Enhanced Visualization of Retinal Pathologies with Ultrahigh Resolution Optical Coherence Tomography

by

Tony Hong-Tyng Ko

B.S., Electrical Engineering and Computer Science
B.S., Bioengineering
University of California at Berkeley, 1997

SUBMITTED TO THE HARVARD-MIT DIVISION OF HEALTH SCIENCES AND TECHNOLOGY

IN PARTIAL FULFILLMENT OF THE REQUIREMENTS FOR THE DEGREE OF

DOCTOR OF PHILOSOPHY IN ELECTRICAL AND MEDICAL ENGINEERING
AT THE
MASSACHUSETTS INSTITUTE OF TECHNOLOGY

JUNE 2005

Signature of Author_____
Harvard-MIT Division of Health Sciences and Technology
May 16, 2005

Certified by_____
James G. Fujimoto, Ph.D.
Professor of Electrical Engineering and Computer Science
Thesis Supervisor

Accepted by_____
Martha L. Gray, Ph.D.
Edward Hood Taplin Professor of Medical and Electrical Engineering
Co-Director, Harvard-MIT Division of Health Sciences and Technology

Enhanced Visualization of Retinal Pathologies with Ultrahigh Resolution Optical Coherence Tomography

by

Tony H. Ko

Submitted to the Harvard-MIT Division of Health Sciences and Technology in May 2005 in Partial Fulfillment of the Requirements for the Degree of Doctor of Philosophy in Electrical and Medical Engineering

Abstract

Current clinical practice calls for the development of techniques to diagnose diseases in its early stages, when treatment is most effective and significant irreversible damage can either be prevented or delayed. Optical coherence tomography (OCT) is an emerging medical diagnostic technology being investigated for applications in a number of medical fields including ophthalmology, cardiology, and gastroenterology. OCT is analogous to ultrasound except that it uses light waves rather than sound waves. OCT can achieve a much higher resolution than ultrasound in measuring the underlying tissue microstructures. Another advantage of OCT is that it can achieve imaging in a non-contact and non-invasive manner. With typical axial resolution of 10 μm, OCT already provides significantly more detailed structural information than any other conventional clinical imaging technique. The development of OCT with even higher resolution would potentially have significant impact in diagnosing diseases in such fields as ophthalmology, cardiology, gastroenterology, and oncology.

Ultrahigh resolution OCT systems have been developed for animal research and clinical ophthalmology. Ultrahigh resolution OCT improves the axial resolution of OCT from the standard 10 μm to 1 μm for animal studies and 3 μm for clinical studies. This improved imaging resolution approaches that of histopathology. Therefore, OCT can potentially function as "optical biopsy" since it permits the imaging of tissue microstructure with resolutions approaching that of histopathology except that imaging can be performed in real time, without the need of tissue removal. Using ultrahigh resolution OCT systems, animal imaging studies have been performed on mouse and rat models of retinal diseases and clinical imaging studies have been performed on more than 800 patients at the ophthalmology clinic. The results from patient imaging studies on a wide variety of retinal diseases suggest that ultrahigh resolution OCT can improve the diagnosis and management of retinal diseases as well as possibly increase the understanding of ocular disease pathogenesis. Therefore, ultrahigh resolution OCT has the potential to become an important tool in ophthalmology research and clinics.

Thesis Supervisor: James G. Fujimoto
Title: Professor of Electrical Engineering and Computer Science

Acknowledgements

This thesis would not be possible without the collaboration of an incredible team of people who have been, in someway, involved with this project. The nature of this interdisciplinary work requires the participation and interaction of people from laser technology development to clinical ophthalmology. During this project, I was fortunate to have worked with many talented and dedicated people on collaborations that have proved to be extremely fruitful and productive, both professionally and personally. Each one of the people I have come in contact with during my graduate career has taught me something about science, career, and life.

I would first like to thank Prof. James Fujimoto, my thesis advisor at MIT. He has provided the incredible infrastructure, resources, and collaborations that he has set up for the completion of this thesis work. With the strenuous trainings that he has provided during my graduate career, I have seen, done, and accomplished so much more than I ever thought it was possible.

Dr. Joel Schuman provided the initial resources, support, and advice for the implementation the ultrahigh resolution OCT system to the clinic at the New England Eye Center (NEEC). He was the first to provide his patients and scientific input for the ultrahigh resolution OCT studies. I will always be grateful for his enthusiasm and support of OCT technology and for this project. Dr. Schuman has since become director and chair of the University of Pittsburgh Medical Center (UPMC) Eye Center and continues to maintain a collaboration with us. Dr. Gadi Wollstein and Dr. Hiroshi Ishikawa have both been very helpful in providing clinical and technical expertise, formerly at NEEC and now at UPMC.

I wish to thank our clinical collaborators at the New England Eye Center for allowing the bulk of this thesis work to be performed in their clinic. Dr. Jay Duker has been incredible in providing the clinical resources and the scientific direction for this project. He is a great mentor who truly embodies the role of a physician-scientist. Medical students Annie Chan and Andre Witkin have been most helpful in performing many ultrahigh resolution OCT measurements as well as spearheading their own projects that resulted from the collected data. Dr. Adelina Paunescu was instrumental in ensuring the initial operation of the system at the clinic. The following ophthalmology attending physicians from NEEC have provided their patients and scientific input for our studies: Dr. Caroline Baumal, Dr. Elias Reichel, Dr. Adam Rogers, Dr. Thomas Hedges III, Dr. Cynthia Mattox, and Dr. Omah Singh. Dr. Janis Lem has been most generous in sharing her animal models of retinal disease with us for our studies in imaging in the animal retina.

We have also performed studies at the Beetham Eye Institute of the Joslin Diabetes Center. Dr. Lloyd P. Aiello was extremely helpful in setting up this clinical collaboration as well as providing scientific analysis of the resulting data. Dr. Sven Bursell was our collaborator in setting up animal studies that have resulting in very interesting results. Joslin colleagues Allen

Clermont and Kim Della-Vecchia have also provided helpful advice on animal handling and imaging of the animal retina.

At MIT, I would like to acknowledge the people who have been involved with the ophthalmology project for their input and support into my work. Wolfgang Drexler had the foresight to start this line of research while he was in our lab; he performed the seminal work on ultrahigh resolution OCT and continues to perform leading studies in the field of ophthalmic OCT imaging. Ingmar Hartl was instrumental in developing the electronics that was necessary for the completion of the clinical ultrahigh resolution OCT system. Andrew Kowalevicz built the compact Titanium:sapphire laser that made the transfer to the clinic possible as well as performed the laser adjustments that made the resolution study possible. Maciej Wojtkowski was responsible for developing the high-speed Spectral OCT systems that seems to be the future of OCT in ophthalmology. Fellow students Desmond Adler and Vivek Srinivasan have been helpful in sharing the load of the ophthalmic OCT projects with me. I am sure Vivek would continue to do great things with Spectral OCT in the field of ophthalmology. Special thanks go out to HST MD student Ravi Ghanta who together with me developed the software for many of the OCT projects in our lab. His great attitude and humorous personality made the tedium of programming actually seem enjoyable!

I have also learned so much from other Postdocs and students that I have met and worked with during my time at MIT. Working with Postdocs or Visiting Scientists such as Wolfgang Drexler, Xingde Li, Ingmar Hartl, Stephane Bourquin, Ping Xue, Yu Chen, Philipp Wagenblast, Maciej Wojtkowski, and Robert Huber have shown me how much I still have to learn about science and research. Many of the other Postdocs and Visiting Scientists that have come through our lab in the past 6 years have also provided many educational opportunities for me. Fellow graduate students Costas Pitris, Rohit Prasankumar, Pei-Lin Hsiung, Andrew Kowalevicz, Aaron Aguirre, Paul Herz, Aurea Tucay, Desmond Adler, Vikas Sharma, and Vivek Srinivasan have shared with me many of the ups and downs of life in science and graduate school together. Great labmates make life in the lab enjoyable and the incredible workload tolerable. I am sure everyone would leave MIT and continue to be a success in science as well as in life.

I am also grateful to Cindy Kopf and Dorothy Fleischer for their help in keeping the group running smoothly and the advices and encouragements they gave to the students.

Finally, I would like to thank my family for their love and support.

Table of Contents

Abstract 3

CHAPTER 1: INTRODUCTION 9
1.1 Overview 9
1.2 Optical Coherence Tomography in Ophthalmology 10
1.3 Scope of Thesis 11
1.4 References 13

CHAPTER 2: ULTRAHIGH RESOLUTION OPTICAL COHERENCE TOMOGRAPHY 16
2.1 Principles of Optical Coherence Tomography 16
Axial and Transverse Resolutions in OCT 19
2.2 Ultrahigh Resolution Optical Coherence Tomography 20
Ultrahigh Resolution OCT System Considerations 21
Laboratory Ultrahigh Resolution OCT System 24
Clinical Ultrahigh Resolution OCT System 26
2.3 References 33

CHAPTER 3: IMAGING SMALL ANIMAL RETINA 35
3.1 Small Animal Models of Retinal Disease 36
3.2 Ultrahigh Resolution OCT Imaging of Mouse Retina 37
Imaging Retinal Degeneration Mouse Model 40
3.3 Ultrahigh Resolution OCT Imaging of Rat Retina 43
3.4 References 46

CHAPTER 4: IMAGING NORMAL RETINA 49
4.1 Interpreting Ultrahigh Resolution OCT Retinal Images 49
4.2 Retinal Mapping of Normal Macula 54
4.3 OCT Axial Resolution vs. OCT Image Quality 57
Source Bandwidth and OCT Axial Resolutions 57
OCT System Considerations 59
OCT Imaging Results 60
4.4 References 65

CHAPTER 5: IMAGING MACULAR PATHOLOGIES 68
5.1 Imaging Protocols 68
5.2 Macular Holes 72
Lamellar Hole 72
Stage 1b Macular Hole 73
Stage 2 Eccentric Macular Hole 75
Stage 3 Macular Hole 77
Stage 4 Macular Hole 78
Understanding Macular Hole Images 81
5.3 Central Serous Chorioretinopathy 82
Follow-up Imaging after One Month 83
Follow-up Imaging after Two Months 83
Understanding Central Serous Chorioretinopathy Images 84

5.4 Macular Edema 86
5.5 Dry Age-related Macular Degeneration 87
5.6 Wet Age-related Macular Degeneration 88
5.7 Retinal Pigment Epithelium Detachment 89
5.8 Epiretinal Membrane 90
5.9 Vitreomacular Traction 91
5.10 Retinitis Pigmentosa 93
5.11 Conclusions 94
5.12 References 96

CHAPTER 6: IMAGING GLAUCOMA 99
6.1 Normal Retinal Anatomy 99
6.2 Early Glaucoma 101
6.3 Moderate Glaucoma 103
6.4 Severe Glaucoma 103
6.5 Localized Glaucomatous Damage 106
6.6 Conclusions from Glaucoma Imaging 107
6.7 References 110

CHAPTER 7: FUTURE WORK AND OUTLOOK 113
7.1 Current Limitations of Ultrahigh Resolution OCT 113
Broadband Laser Light Source 113
Limited Image Acquisition Speed 114
New Ultrahigh Resolution OCT Technologies 115
7.2 Broadband Superluminescent Diode Light Source 115
Multiplexed SLD Light Source 116
Ultrahigh Resolution OCT System Considerations 117
Ultrahigh Resolution OCT of hamster cheek pouch *in vivo* 120
Ultrahigh Resolution OCT of human retina *in vivo* 122
Conclusions from Broadband SLD Imaging 131
7.3 High-Speed, Ultrahigh Resolution OCT Imaging 132
Spectral Domain Ultrahigh Resolution OCT System 134
High-Speed, Ultrahigh Resolution OCT Imaging 137
Conclusions from High-Speed, Ultrahigh Resolution OCT Imaging 143
7.4 Future of Ophthalmic Ultrahigh Resolution OCT Imaging 146
7.5 References 147

CHAPTER 1: INTRODUCTION

1.1 Overview

The main goal of this thesis project is to develop ultrahigh resolution optical coherence tomography for applications in the field of ophthalmology. Optical coherence tomography (OCT) is an emerging medical imaging technology that can perform micron scale, tomographic cross-sectional imaging of internal tissue microstructure *in situ* and in real time.[1-6] OCT imaging is somewhat analogous to ultrasound B mode imaging except that it is performed using light rather than acoustical waves. Tomographic OCT images are generated by scanning an optical beam across the tissue and measuring the echo time delay and intensity of light which is reflected or backscattered from internal tissue microstructures.

Optical coherence tomography (OCT) imaging was reported in 1991 when the first *in vitro* OCT images were demonstrated in the human retina and coronary artery.[1] The first *in vivo* imaging of the normal human retina was reported in 1995.[7] The axial image resolution in that study was 10 μm in tissue and imaging was performed at ~800 nm wavelength. The first demonstration of OCT imaging of the anterior eye was reported in 1994.[8] In addition to ophthalmology, OCT has also demonstrated its potential for imaging a wide range of tissues other than the eye. By performing OCT imaging at longer wavelengths of 1.3 μm, typical image penetration depths of 2-3 mm can be achieved in a wide range of scattering biological tissues.[3, 4] Numerous OCT imaging studies have been performed demonstrating the application of OCT in arterial, GI, pulmonary, reproductive, and neural pathologies.[5, 9-12] OCT imaging has been investigated for surgical guidance applications.[13, 14] OCT has also been applied to developmental biology for the imaging of developmental specimens, neural development, and cardiovascular function.[15-17]

1.2 Optical Coherence Tomography in Ophthalmology

To date, OCT has had its largest clinical impact in ophthalmology. OCT has a number of features which make it attractive as an imaging modality for ophthalmology. OCT can perform imaging with resolutions approaching that of histopathology, with standard resolution OCT technology achieving axial image resolutions of 10 μm. OCT images have significantly higher resolution than other imaging modalities and are the first images that actually permit the delineation of retinal substructure *in vivo*. The sensitivity of OCT is extremely high, usually in excess of 100 dB, corresponding to the detection of reflected optical signals of 1 part in 10^{10}. This high sensitivity is helpful in imaging the relatively transparent retinal tissue; it also means that cross-sectional imaging can be performed in OCT with low and safe illumination levels. In ophthalmology, the cross-sectional information that OCT provides about retinal tissue morphology is impossible to obtain by any other non-invasive technique. In addition, it is possible to perform repeated imaging to monitor disease progression and/or response to therapeutic treatment since OCT can be performed in a non-contact and non-invasively manner. Finally, OCT images are stored in digital format that can facilitate the use of image processing techniques and expert algorithms to yield quantitative information about the OCT data.[18, 19] The ability to image and quantitate retinal structure has a wide range of applications for the diagnosis and monitoring of retinal disease.[20] Because of these features of OCT imaging, it is useful in ophthalmology applications in generating cross-sectional images of retinal morphology that can provide additional diagnostic information that is complementary to conventional fundus photography and fluorescein angiography.[20]

Optical coherence tomography was invented and developed for ophthalmic imaging by Prof. James G. Fujimoto's group at Massachusetts Institute of Technology in collaboration with Carmen A. Puliafito and Joel S. Schuman of the New England Eye Center, Tufts University School of Medicine, and Eric A. Swanson of MIT Lincoln Laboratory.[7, 21, 22] A clinical OCT prototype that can be operated by an ophthalmic technician was developed in 1993, and clinical imaging studies on a variety of ocular diseases were initiated at the New England Eye Center. Many of the first cross-sectional and longitudinal OCT studies on a wide range of ophthalmic diseases resulted from this collaboration. Ophthalmic diseases that were investigated with OCT including macular holes, glaucoma, age-related macular degeneration, macular edema, and

diabetic retinopathy.[7, 19, 22-26] Since OCT can provide direct information on the dimensions of structures, it permits the quantitative measurement of nerve fiber layer (NFL) thickness and can be an important technique for the diagnosis and monitoring of glaucoma. The first studies demonstrating OCT for nerve fiber layer assessment and diagnosis of glaucoma was reported in 1995.[18, 27] The protocol that was developed for NFL assessment in these studies have become clinical standards and are used in the commercial OCT systems today. In addition, OCT can measure retinal thickness and may detect changes that are below the threshold for detection on a standard ophthalmoscopic examination of the fundus.[19, 23] The first studies of macular edema using OCT was reported in 1995.[19] The OCT scanning protocol developed in these initial studies for mapping macular thickness has become the clinical standard in use today.[19]

Since these initial studies in ophthalmology, OCT technology was patented and subsequently transferred to industry (Humphrey Systems, Dublin, CA which subsequently has been acquired by Carl Zeiss Meditec, Inc.). OCT was developed into a clinical instrument and introduced into the clinical ophthalmology market in 1996. The adoption of OCT proceeded slowly at first, with only a few hundred instruments in use during a period of several years. A second generation instrument with additional software features was introduced in 2000, but adoption by the clinical ophthalmology community continues to be slow. In 2002, the second generation instrument was re-engineered to achieve a 4x increase in imaging speed and a third generation instrument, the StratusOCT was introduced by Carl Zeiss Meditec. This current commercial OCT system has a 10 μm axial resolution and can acquire a 512 axial scan (transverse pixel) image in ~1.3 seconds. With the availability of extensive clinical data as well as improved technology, OCT imaging is now rapidly being adopted in ophthalmology. There are now thousands of StratusOCT systems in use internationally and OCT technology is rapidly becoming a standard clinical tool for the diagnosis and management of a wide variety of ocular diseases.[20]

1.3 Scope of Thesis

The hypothesis of this thesis project is that improving the axial resolution of OCT will improve the ability to image retinal structural morphology such as intraretinal layers. Enhancing the visualization of intraretinal structures and improving the assessment of morphologic changes associated with retinal diseases should further advance the application of OCT technology in

ophthalmology. This research is the product of an ongoing collaboration between James G. Fujimoto of the Massachusetts Institute of Technology, Jay S. Duker of the New England Eye Center, Tufts University School of Medicine, and Joel S. Schuman of the University of Pittsburgh School of Medicine.

Chapter 2 is an overview of OCT principles and the development of ultrahigh resolution OCT which can improve OCT resolution from the standard 10 μm resolution to 1-3 μm axial resolution. A laboratory based ultrahigh resolution OCT system capable of performing retinal imaging studies in animal models is described in this chapter. In addition, the development of a clinical ultrahigh resolution OCT system capable of performing imaging studies in the ophthalmology clinic is also discussed. Chapter 3 describes retinal imaging studies performed on small animal models using the laboratory based ultrahigh resolution OCT system. Chapter 4 describes retinal imaging studies performed on normal subjects in order to validate the clinical ultrahigh resolution OCT system. Chapter 5 describes macular imaging studies performed on patients at the ophthalmology clinic using the clinical ultrahigh resolution OCT system. Chapter 6 describer glaucoma imaging studies performed on glaucoma patients using the clinical ultrahigh resolution OCT system. Finally, Chapter 7 discusses the future outlook of this technology by introducing new technology that can overcome the light source and speed limitations of the current ultrahigh resolution OCT systems.

1.4 References

1. Huang D, Swanson EA, Lin CP, et al. Optical coherence tomography. Science 1991;254(5035):1178-81.

2. Swanson EA, Huang D, Hee MR, et al. High-speed optical coherence domain reflectometry. Optics Letters 1992;17:151-3.

3. Fujimoto JG, Brezinski ME, Tearney GJ, et al. Optical biopsy and imaging using optical coherence tomography. Nature Medicine 1995;1(9):970-2.

4. Brezinski ME, Tearney GJ, Bouma BE, et al. Optical coherence tomography for optical biopsy. Properties and demonstration of vascular pathology. Circulation 1996;93(6):1206-13.

5. Tearney GJ, Brezinski ME, Bouma BE, et al. In vivo endoscopic optical biopsy with optical coherence tomography. Science 1997;276(5321):2037-9.

6. Fujimoto JG. Optical coherence tomography for ultrahigh resolution in vivo imaging. Nature Biotechnology 2003;21(11):1361-7.

7. Hee MR, Izatt JA, Swanson EA, et al. Optical coherence tomography of the human retina. Archives of Ophthalmology 1995;113(3):325-32.

8. Izatt JA, Hee MR, Swanson EA, et al. Micrometer-scale resolution imaging of the anterior eye in vivo with optical coherence tomography. Archives of ophthalmology 1994;112(12):1584-9.

9. Brezinski ME, Tearney GJ, Bouma BE, et al. High-Resolution Imaging of Plaque Morphology With Optical Coherence Tomography. Circulation 1995;92(8):103-.

10. Pitris C, Brezinski ME, Bouma BE, et al. High resolution imaging of the upper respiratory tract with optical coherence tomography: a feasibility study. American journal of respiratory and critical care medicine 1998;157(5) Pt 1:1640-4.

11. Pitris C, Goodman A, Boppart SA, et al. High-resolution imaging of gynecologic neoplasms using optical coherence tomography. Obstetrics and gynecology 1999;93(1):135-9.

12. Boppart SA, Brezinski ME, Pitris C, Fujimoto JG. Optical coherence tomography for neurosurgical imaging of human intracortical melanoma. Neurosurgery 1998;43(4):834-41.

13. Boppart SA, Bouma BE, Pitris C, et al. Forward-imaging instruments for optical coherence tomography. Optics Letters 1997;22(21):1618-20.

14. Boppart SA, Bouma BE, Pitris C, et al. Intraoperative assessment of microsurgery with three-dimensional optical coherence tomography. Radiology 1998;208(1):81-6.

15. Boppart SA, Brezinski ME, Bouma B, et al. In-Vivo Imaging of Developing Morphology Using Optical Coherence Tomography. Molecular Biology of the Cell 1995;6:662-.

16. Boppart SA, Bouma BE, Brezinski ME, et al. Imaging developing neural morphology using optical coherence tomography. Journal of Neuroscience Methods 1996;70(1):65-82.

17. Boppart SA, Tearney GJ, Bouma BE, et al. Noninvasive assessment of the developing Xenopus cardiovascular system using optical coherence tomography. Proceedings of the National Academy of Sciences of the United States of America 1997;94(9):4256-61.

18. Schuman JS, Hee MR, Puliafito CA, et al. Quantification of nerve fiber layer thickness in normal and glaucomatous eyes using optical coherence tomography. Archives of Ophthalmology 1995;113(5):586-96.

19. Hee MR, Puliafito CA, Duker JS, et al. Topography of diabetic macular edema with optical coherence tomography. Ophthalmology 1998;105(2):360-70.

20. Schuman JS, Puliafito CA, Fujimoto JG. Optical coherence tomography of ocular diseases, 2nd edition. Thorofare, NJ: Slack Inc., 2004.

21. Swanson EA, Izatt JA, Hee MR, et al. In vivo retinal imaging by optical coherence tomography. Optics Letters 1993;18(21):1864-6.

22. Puliafito CA, Hee MR, Lin CP, et al. Imaging of macular diseases with optical coherence tomography. Ophthalmology 1995;102(2):217-29.

23. Hee MR, Puliafito CA, Wong C, et al. Quantitative assessment of macular edema with optical coherence tomography. Archives of Ophthalmology 1995;113(8):1019-29.

24. Hee MR, Puliafito CA, Wong C, et al. Optical coherence tomography of macular holes. Ophthalmology 1995;102(5):748-56.

25. Hee MR, Puliafito CA, Wong C, et al. Optical coherence tomography of central serous chorioretinopathy. American Journal of Ophthalmology 1995;120(1):65-74.

26. Hee MR, Baumal CR, Puliafito CA, et al. Optical coherence tomography of age-related macular degeneration and choroidal neovascularization. Ophthalmology 1996;103(8):1260-70.

27. Schuman JS, Pedut-Kloizman T, Hertzmark E, et al. Reproducibility of nerve fiber layer thickness measurements using optical coherence tomography. Ophthalmology 1996;103(11):1889-98.

CHAPTER 2: ULTRAHIGH RESOLUTION OPTICAL COHERENCE TOMOGRAPHY

Optical coherence tomography (OCT) at standard 10 μm resolution has already demonstrated its usefulness in clinical ophthalmology. In 2002, the third generation of commercial OCT instrument for ophthalmology was introduced (StratusOCT, Carl Zeiss Meditec, Dublin, CA). This system represents a four-fold increase in imaging speed over previous commercial and prototype devices, and it is rapidly becoming a standard imaging tool at the ophthalmology clinic.[1] The goal of this thesis is to develop ultrahigh resolution OCT for applications in ophthalmology. Improving OCT axial imaging resolution from the standard 10 μm down to 1-3 μm range should enhance the visualization of retinal and intraretinal structural morphology, which could have implications in research and clinical ophthalmology.

2.1 Principles of Optical Coherence Tomography

Optical coherence tomography (OCT) performs imaging by measuring the echo delay time of light reflected from internal tissue structures. Because the velocity of light is extremely high, direct measurement of optical echoes cannot be performed electronically as in ultrasound. OCT is based on a technique known as low coherence interferometry that has been applied in microelectronic devices as well as in biological systems to perform optical ranging with micrometer resolution.[2-4] Figure 2-1 shows schematically how low coherence interferometry works. Measurements are performed using a Michelson interferometer with a low coherence light source. Low coherence light can be generated by a superluminescent semiconductor diode (as in the commercial StratusOCT instrument) or other sources such as a femtosecond solid-state

laser. One arm of the interferometer directs the light onto the sample and collects the reflected signal. A second reference arm contains a retroreflecting mirror which is mechanically translated. If the interferometer uses a coherent light source, then interference between the light from the sample and reference mirror occurs as the relative path lengths between the sample and reference mirror are varied. In contrast, if a low coherence light source is used, constructive interference between the light from the sample and reference mirror occurs only when the optical distance traveled by the light in both the tissue sample and reference paths match to within the coherence length of the light (ΔL_c). Detecting and demodulating the interferometer output permits a precise measurement of the echo time delay and magnitude of reflected light.

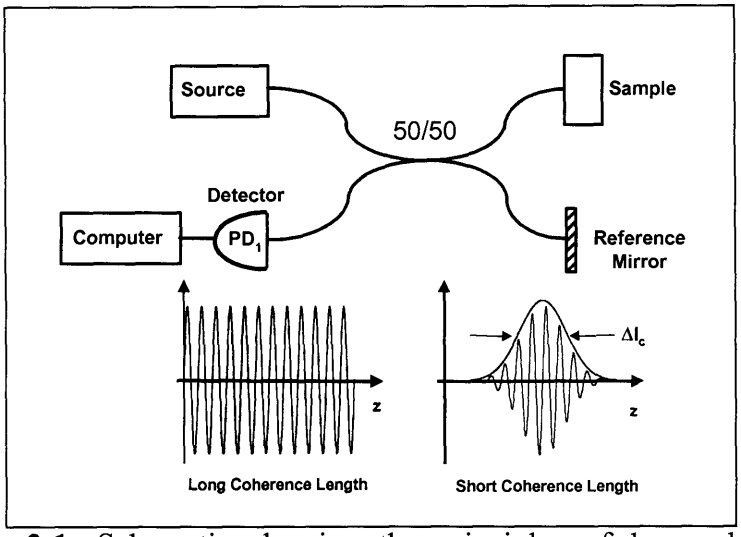

Figure 2-1. Schematic showing the principles of low coherence interferometry for measuring reflected light from the internal microstructure of a sample

Figure 2-2 shows a schematic of how cross-sectional images are generated in OCT. At each transverse position on the tissue sample, an axial measurement (or A-scan) is performed by obtaining the intensity of the backscattered light as a function of axial position (or echo delay time) in depth. Two dimensional cross-sectional imaging of tissue is performed by laterally scanning the optical beam under computer control and acquiring sequential axial measurements (A-scans) at different transverse positions. The resulting data set is a two dimensional array which represents the optical backscattering or reflection within a cross-sectional slice of the

tissue. This two-dimensional data of optical backscattering from the tissue can then be displayed as a gray scale or false color image.

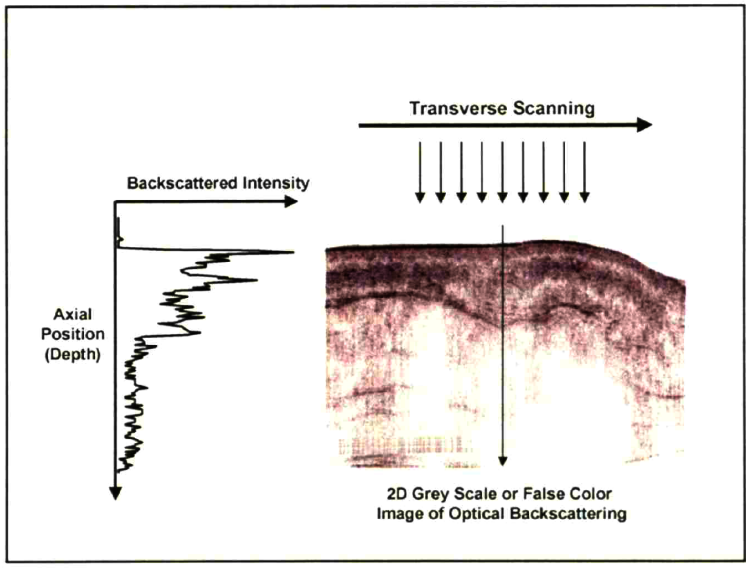

Figure 2-2. Cross-sectional OCT images of internal tissue microstructure are generated by scanning the OCT beam across the tissue to measure the backscattered intensity as a function of axial and transverse position.

The standard implementation of the OCT system as shown in Figure 2-1 uses a fiber optic coupler and a galvanometer scanner to mechanically scan the reference arm mirror in a linear fashion. The motion of the reference arm mirror performs axial depth scanning while transverse scanning is performed by moving the OCT beam to different transverse positions in order to acquire two-dimensional cross-sectional data. As the reference mirror path is scanned, interference fringes are generated which can be detected with a photodetector. Since low-coherence light sources consists of different optical wavelengths, every optical wavelength $\lambda_{optical}$ that is present in the OCT light source will have a corresponding frequency f in the time domain in which it will be mapped into. This mapping relationship is determined by the linear scanning velocity v of the reference mirror.

$$f = \frac{2v}{\lambda_{optical}} \tag{2.1}$$

Where v is the scanning velocity and $\lambda_{optical}$ are the optical wavelengths of the source. The central frequency of this frequency spectrum corresponds to the central wavelength of the OCT light source and is referred to as the Doppler frequency of the system. The subsequent detection electronics and filters must be optimized for the Doppler frequency and the bandwidth of this frequency spectrum.

Axial and Transverse Resolutions in OCT

The axial and transverse resolutions in OCT are determined independently by different physical mechanisms. The transverse resolution is governed by the focal spot size (as in conventional microscopy), while the axial resolution is governed by the coherence length of the light source (rather than the confocal parameter or depth of field as in microscopy).

The coherence length and hence the axial resolution (dz) in OCT is inversely proportional to the optical bandwidth of the light source. For a Gaussian optical spectrum, the coherence length (ΔL_c) is determined by

$$\Delta L_c = \frac{2\ln(2)\lambda_o^{\,2}}{\pi(\Delta\lambda)} = dz \qquad (2.2)$$

where ($\Delta\lambda$) is the optical bandwidth and the λ_o is the center wavelength of the light source.[5] This implies that axial resolution can be enhanced by using broad bandwidth optical sources such as superluminescent semiconductor diodes or femtosecond solid-state lasers. Incandescent sources, although broad bandwidth, do not produce sufficient intensity in a signal spatial mode to perform imaging.

The transverse resolution of OCT is determined by the focused transverse spot size of the optical beam. The transverse spot size is given by:

$$dx = \sqrt{\frac{2b\lambda}{\pi}} \qquad \text{or equivalently} \qquad dx = \frac{4\lambda f}{\pi d} \approx \frac{\lambda}{2NA} \qquad (2.3)$$

where b is the confocal parameter, d is spot size on the objective lens and f is its focal length. Increasing the numerical aperture (NA) reduces the spot size and improves transverse resolution, but also reduces the working distance. In addition, in a manner similar to conventional microscopy, increasing the transverse resolution also produces a decrease in the depth of focus. Figure 2-3 demonstrates the effect that using a low numerical aperture lens versus a high numerical aperture lens has on the transverse resolution of OCT.

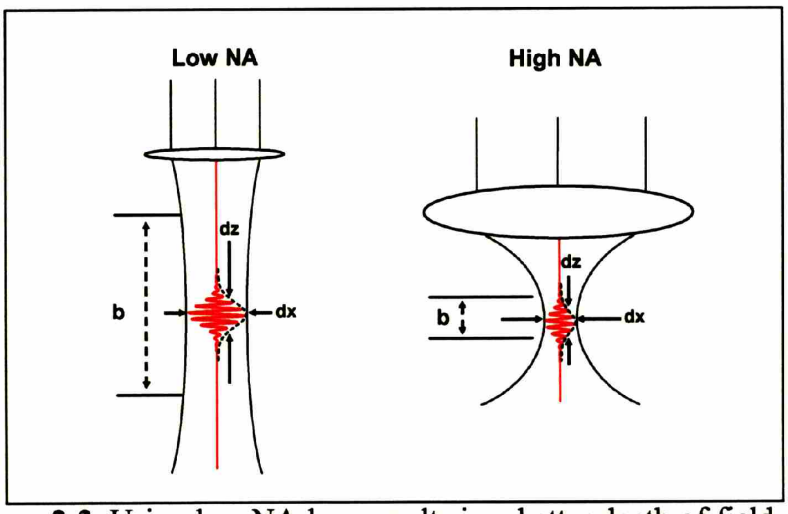

Figure 2-3. Using low NA lens results in a better depth of field at the expense of a degraded transverse resolution while a high NA lens results in better transverse resolution with short depth of field.

The axial resolution in OCT imaging is determined by the coherence length of the light source and is independent of the confocal parameter. This is an important advantage of OCT because this makes it possible to achieve high axial resolution imaging even in systems such as the eye which have limited pupil apertures. This is in contrast to classical microscopy or confocal microscopy, where high axial resolutions necessitate high numerical apertures and short working distances. Unlike confocal microscopy, OCT also images in cross-sectional planes rather than *en face* planes and thus yields images that better matches with the usual cross-sectional view of biopsy and histology.

2.2 Ultrahigh Resolution Optical Coherence Tomography

Standard ophthalmic OCT systems (e.g., StratusOCT) use superluminescent diodes emitting light with 20-30 nm bandwidths centered at 830 nm, resulting in a 10-15 μm axial image resolution. By using femtosecond Titanium-sapphire lasers, bandwidths of up to 260 nm can be achieved around the 830 nm center wavelength.[6] This improvement in the performance of the broadband light source would lead to ultrahigh OCT axial resolution of ~1 μm.[7] Figure 2-

4 demonstrate the difference between standard and ultrahigh OCT resolution near the 830 nm center wavelength.

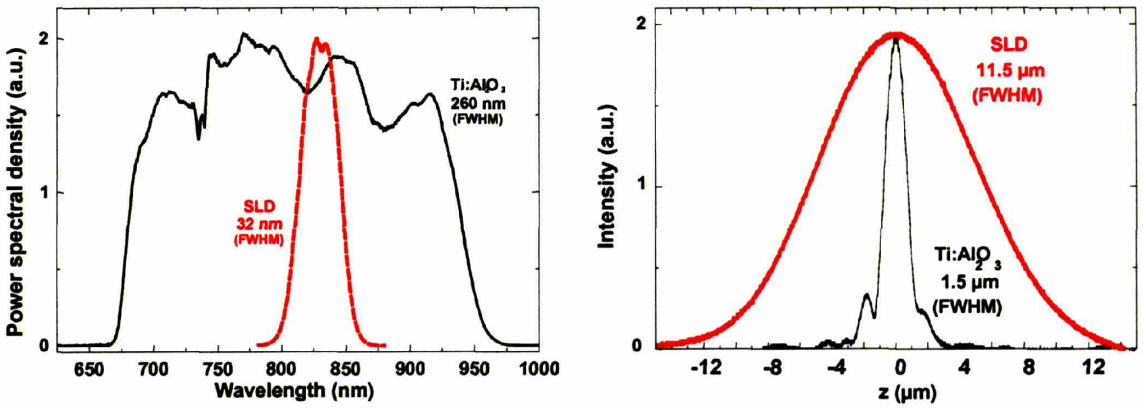

Figure 2-4. Optical output spectrum (left) and the envelopes of the coherence function (right) of the Titanium:sapphire laser (black) versus a superluminescent diode (SLD) light source (red). An optical bandwidth of 260 nm enables a free space resolution of ~1 μm compared to 32 nm and 11.5 μm using a SLD.

Ultrahigh Resolution OCT System Considerations

The standard optical and electrical components of an OCT system needs to be modified before the system can take advantage of the broadband performance of the femtosecond laser to achieve ultrahigh resolution OCT. Figure 2-5 depicts the basic optical and electrical components of an OCT system. The basic OCT system consists of a low-coherence light source, a fiber optic coupler to separate the incoming source light into the sample and reference arm, an optical pathlength scanning mechanism (e.g., a scanning mirror) in the reference arm, a beam delivery instrument to deliver the beam to the tissue specimen as well as control the transverse position of the beam, and a photodetector to detect the interference signal between the reference and sample fields. After the photodetector detects the optical signal, an electronic fringe signal is first bandbpass filtered to remove the noise outside of the expected frequency spectrum (see equation 2.1), then the envelope of the interference fringes are extracted typically by a logarithmic demodulator before the signal is digitized by an analog-to-digital acquisition card (A-D) and sent to the computer for processing, display, and storage. In order to achieve ultrahigh resolution

OCT performance, broadband fiber optic couplers needs to be selected so that the system can support the broad bandwidth of the ultrahigh resolution light source. In addition, achromatic lenses should also be implemented in the reference and sample arm in order to reduce chromatic aberration and backcoupling losses.

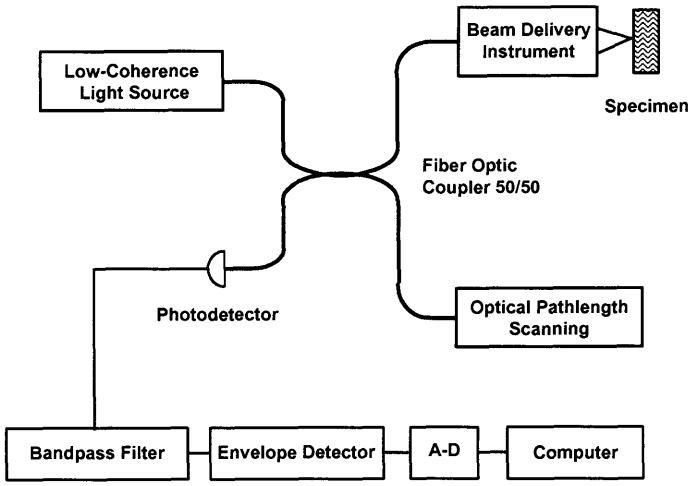

Figure 2-5. The basic OCT system layout includes a low-coherence light source, a fiber optic coupler, sample arm and reference arm optics. The detected signal is first bandpass filtered before envelope demodulation and computer digitization.

The detection signal-to-noise (SNR) performance in OCT can be calculated from optical communications theory and is given by SNR = $10\text{Log}(\eta P)/(E \cdot NEB)$ where P is the power that is reflected or backscattered, NEB (noise equivalent bandwidth) is proportional to the bandwidth of the electronic detection, η is the photo-detector efficiency, and E is the energy of the photon. This formula essentially means that the signal-to-noise performance in OCT is proportional to the power detected divided by the electronic bandwidth or the data rate. Therefore, higher image acquisition speeds as well as higher resolutions will both decrease the signal-to-noise performance of the system. For example, the broad optical bandwidths of the ultrahigh resolution OCT light source would necessitate using broad passband bandwidths in the bandpass filter which would increase the NEB and decrease the SNR of the system. Decreasing the linear scanning speed of the reference arm can increase the SNR performance of the ultrahigh resolution OCT system; however, decreasing the reference arm scanning speed also increases the

total image acquisition time. In ophthalmic imaging, the increased acquisition time could make imaging in patients prohibitively long as well as increasing the axial motion artifacts in the resulting OCT image. In ultrahigh resolution OCT, the excess intensity noise from the femtosecond laser light sources will also be included in the detected OCT signal and further degrade signal-to-noise (SNR) performance. Dual-balanced detection schemes are usually implemented to remove the excess intensity noise of the laser light source and improve the SNR performance of ultrahigh resolution OCT systems.

As shown in Figure 2-5, a single-detector interferometer design with a 50/50 coupler means that half of the interference signal will be lost in the fiber coupler on the way to the photodetector. Neglecting losses in the optical components, the power available for both the sample and the reference arms is 0.5 P_o, where P_o is the output power of the broadband source. The signal S generated by the interference between the reference and sample arm fields will also be evenly split by the 50/50 fiber coupler. Therefore, the signal detected at the photodetector is 0.5 S while the other 0.5 S is passed back into the broadband source.

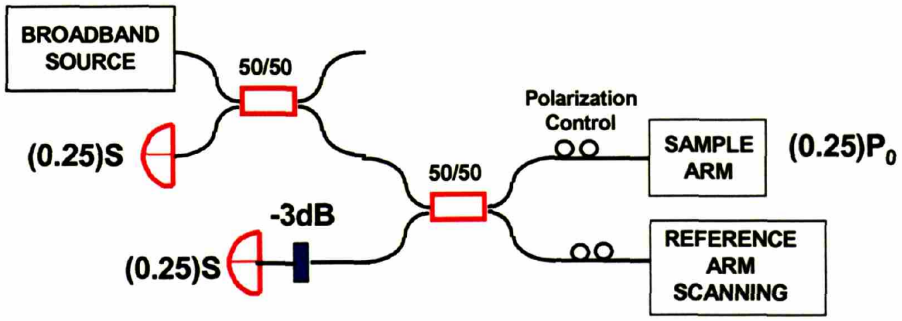

Figure 2-6. Dual-balanced detection using symmetric 50/50 interferometers. The excess intensity noise of the broadband laser light source can be removed, but less of the source power is available on the sample for imaging.

Figure 2-6 shows a typical dual-balance detection scheme using symmetric 50/50 interferometers. In dual-balanced detection, the excess intensity noise of the broadband laser light source is removed by performing differential measurements of the interference signal with two photodiodes. The power available for both the sample and the reference arms is only 0.25 P_o since two 50/50 fiber couples are implemented sequentially. On the return path to the

photodetectors, 0.5 S of the interference signal S is available at the first photodiode while 0.25 S is available at the second photodiode. Light traveling in the "bar" path through the fiber coupler (i.e., from a lower port to an upper port or vice versa) obtains a $-\pi/2$ phase shift relative to the light that travels in the "cross" path (i.e., from a lower port to a lower port, or an upper port to an upper port). Therefore, the interference signal at the two photodiodes will be out of phase while the intensity noise at the two detectors will still be in phase. Electronic subtraction of the signals at the two detectors will have the effect of doubling the detected signal power (a 3 dB increase in SNR) while cancel much of the intensity noise of the broadband laser light source (usually another ~3 dB improvement in SNR).[8] However, since good noise cancellation is only obtained when the signal at the two photodiodes are equivalent, a -3 dB attenuation is usually applied to the first photodiode and the signal detected at the photodetector is only 0.25 S. Comparing to the single-detector interferometer design, 0.25 S is 3 dB less than the 0.5 S detected by the signal detector of that detection setup. Therefore, dual-balanced detection using symmetric 50/50 interferometers was able to improve the SNR performance of the ultrahigh resolution OCT system by about 3 dB.

Laboratory Ultrahigh Resolution OCT System

The first ultrahigh resolution OCT system was demonstrated in our laboratory using a femtosecond Kerr-lens modelocked Titanium:sapphire laser as the low coherence light source.[7] This laser emits pulses as short as <5.5 fs, corresponding to bandwidths of up to 350 nm centered at 800 nm with an average power of 150 mW.[6] This high performance was achieved by using specially designed double chirped mirrors which have a high reflectivity bandwidth and controlled dispersion response, in combination with low-dispersion prisms for intracavity dispersion compensation.[6] For ultrahigh resolution OCT imaging, a bandwidth of up to 260 nm could be coupled into the fiber optic OCT system. An ultrahigh resolution OCT system that can accommodate the broad bandwidth of the laser light source was developed for OCT imaging. Figure 2-7 is a schematic of the ultrahigh resolution OCT system. The optical components of the this ultrahigh resolution OCT system can typically support ~200 nm bandwidth and ultrahigh axial resolution of ~1-2 μm can be achieved. The dual-balanced detection design utilized two broadband 50/50 fiber couplers (FC) in order to remove the excess intensity noise of the Titanium:sapphire laser and improve SNR performance of the system by ~3 dB. Axial

resolution will be degraded by both chromatic aberration and group-velocity dispersion mismatch between the reference and the sample arm. Achromatic lenses (CL's, OL) optimized for a bandwidth from 600 to 1000 nm were used in both the sample arm and the reference arm. Dispersion mismatch between the sample arm and reference arm is further compensated by inserting variable-thickness fused-silica (FS) and BK7 prism pairs into the reference arm until uniform group-delay dispersion is achieved. Polarization mismatch can further degrade the shape and peak height of the interference fringes, so polarization controllers (PC's) were used to adjust for polarization mismatch.[7] The sample arm optics is attached to a stage that is computer controlled and can be scanned in both transverse directions (X and Y). High NA superachromat objective lens (OL) was used to achieve a transverse resolution of ~5 μm at a working distance of 10 mm.

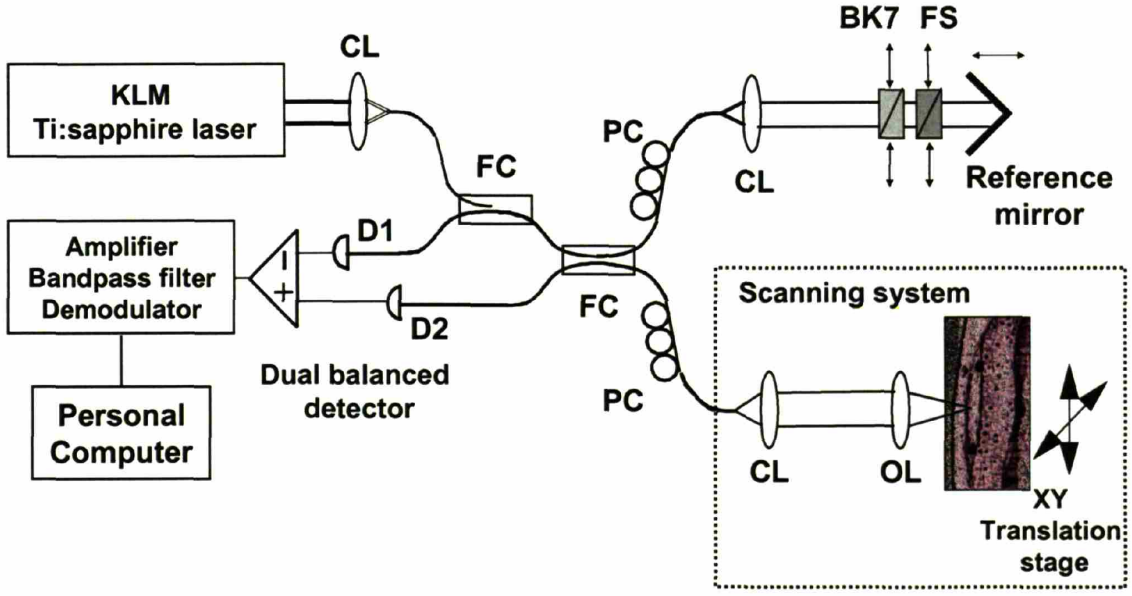

Figure 2-7. Schematic layout of the laboratory ultrahigh resolution OCT system. An imaging microscope in the sample arm is translated by a stage in order to scan the OCT beam on the sample. A dual balanced detection is utilized in order to cancel the excess noise of the femtosecond laser source in the range of the OCT detection band.

With the two 50/50 couplers in the dual-balanced configuration, the power output of the Titanium:sapphire laser typically can deliver over 3 mW power onto the sample for OCT

imaging. The linear scanning speed of the reference arm mirror in this system is 82 mm/s. For an axial scan of about 1 mm, the typical imaging time is about 20 seconds for a 1000 A-scan image. The bandpass filter has a center frequency of 205 kHz and passband bandwidth of 54 kHz. For these imaging parameters, the typical SNR performance of this laboratory ultrahigh resolution OCT is ~110 dB which means that reflected signals as small as 10^{-11} of the incident signal may be detected. Typically, SNR sensitivity of about 90 dB is sufficient for acquiring high contrast retinal OCT images.

The laboratory ultrahigh resolution OCT system has the axial resolution of ~1-2 μm and SNR sensitivity of ~110 dB and is suitable for performing imaging studies on *in vitro* tissue preparations and small animal models of retinal diseases. However, the imaging speed of the system (typically >10 seconds) is too slow to perform *in vivo* retinal imaging studies in humans. A clinical ultrahigh resolution OCT system needs to achieve imaging in a sufficiently short time that the patient subject can maintain eye fixation without blinking during individual OCT scans. In addition, the femtosecond Titanium:sapphire laser used to achieve the high imaging performance is too bulky and unsuitable for implementation in the ophthalmology clinic. In order to study a large number of ophthalmic patients using ultrahigh resolution OCT, a more portable and robust laser would have to be developed.

Clinical Ultrahigh Resolution OCT System

In order to perform ultrahigh resolution OCT studies outside of the research laboratory and in the ophthalmology clinic, a new broadband light source needed to be developed. Typical femtosecond lasers are expensive and are not easily transported for operations in the clinic. A laser light source suitable for use in the clinic must be made more portable, more robust, and lower cost. For performing *in vivo* ophthalmic imaging studies, the ANSI safety standard limits the retinal exposure that is permissible for imaging. Therefore, a laser that is developed for clinical use does not require very high power output and a lower power pump laser can be utilized to reduce the size and cost of the clinical laser, making it more portable and more robust. However, a Titanium:sapphire laser that can achieve modelocking at a lower threshold would have to be developed before a lower power pump laser can be implements. In collaboration with Andrew Kowalevicz from our group, we have developed an ultra-low-threshold femtosecond Titanium:sapphire laser as the light source for the clinical ultrahigh resolution OCT system. This

laser is able to achieved a record low pump power operation of <200 mW, a factor of 10x lower than standard Titanium:sapphire laser designs.[9] Since the cost of femtosecond lasers depends on the pump power requirement, this laser can achieve cost savings of a factor of 2 to 4 times compared to standard Titanium:sapphire femtosecond lasers. Figure 2-8 shows the schematic and a photograph of this compact and portable Titanium:sapphire femtosecond laser.

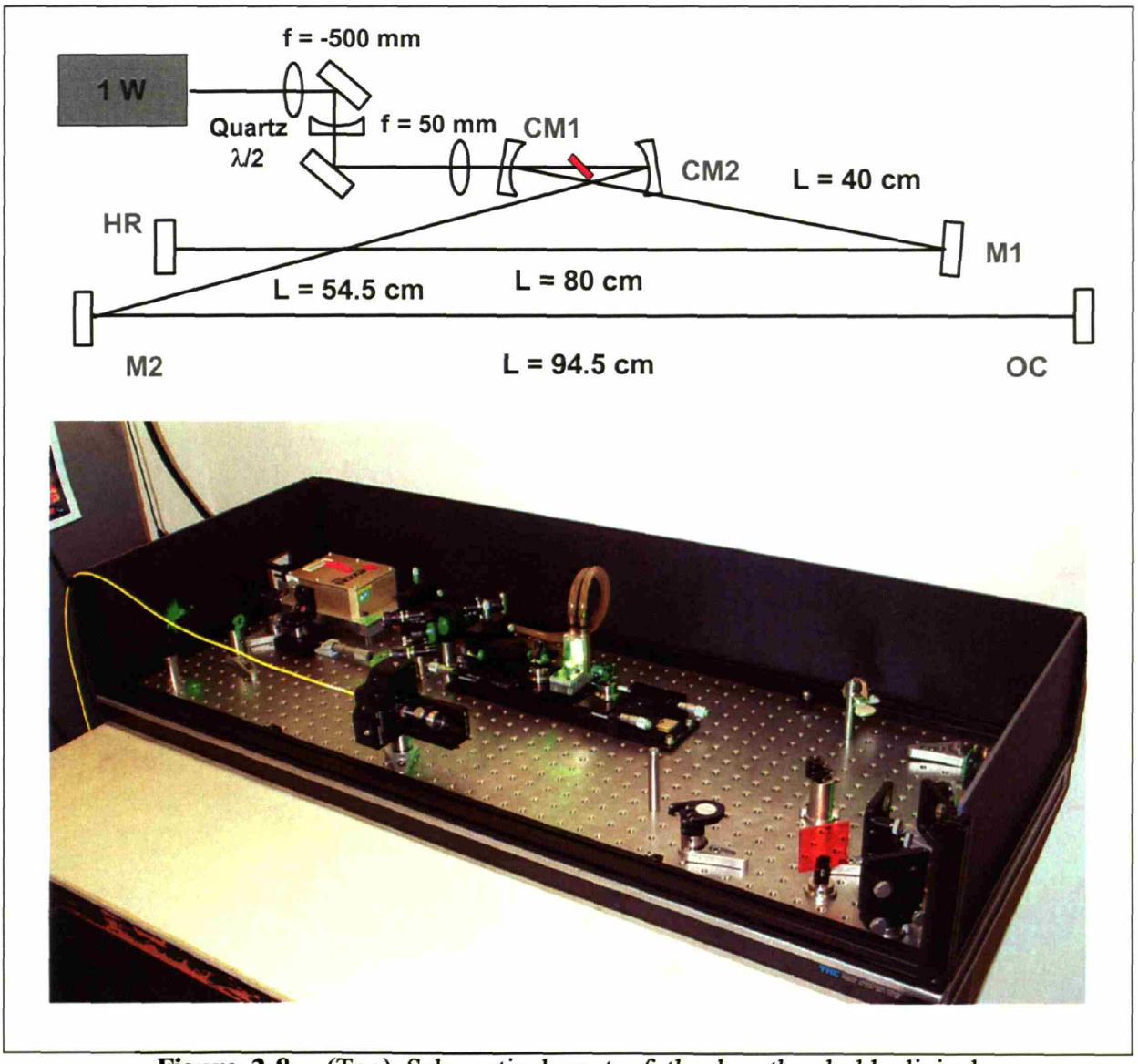

Figure 2-8. (Top) Schematic layout of the low-threshold clinical femtosecond Titanium:sapphire laser using a 1 watt pump laser instead of the typical 5 watt pump source. (Bottom) A picture of the low-threshold clinical laser; the laser has a small footprint and is contained in a laser box that can be transported to the ophthalmology clinic.

This laser is portable, has a small footprint, and is suitable for implementation into the ophthalmology clinic to perform ultrahigh resolution OCT imaging studies. Figure 2-9 depicts the output bandwidth of this laser. Under optimum setting, this laser can generate very broad ~160 nm bandwidths with 15 mW of output power. For clinical imaging, it is generally believed that the chromatic aberrations of the human eye does not support OCT axial resolutions that are significantly less the 3 μm.[10] Therefore, for clinical imaging, the laser was adjusted to operate at ~120 nm bandwidth in order to achieve higher output power of 50 mW as well as a more Gaussian spectrum to reduce sidelobe artifacts in the ophthalmic image. With ~120 nm output bandwidth, the low-threshold clinical laser can achieve ultrahigh resolution OCT imaging of ~3 μm in the eye.

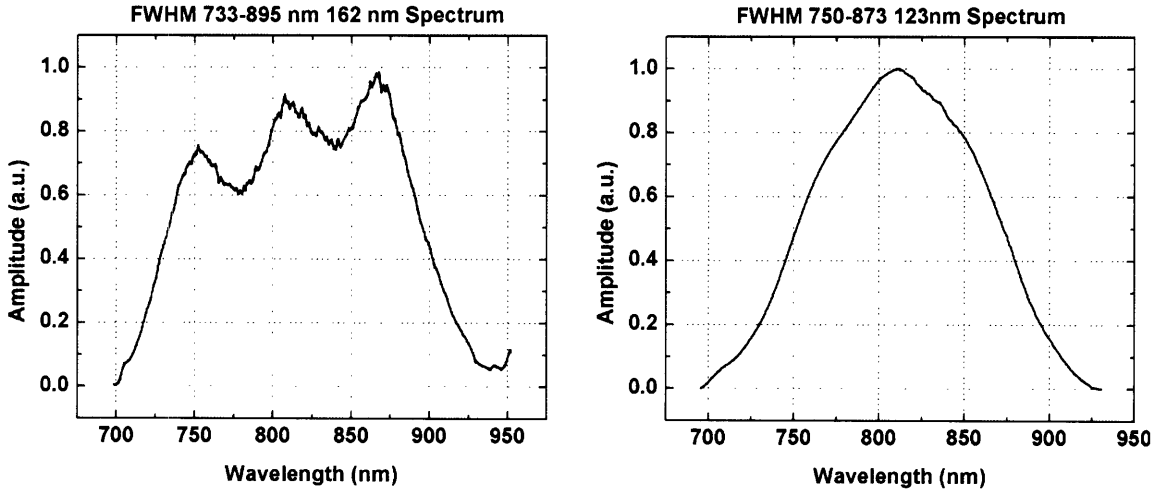

Figure 2-9. (Left) The optimum output spectrum of the low-threshold laser produces ~160 nm bandwidth with 15 mW of output power. (Right) The clinical output spectrum of the low-threshold laser produces ~120 nm Gaussian bandwidth with 50 mW of output power.

A clinical ultrahigh resolution OCT system that can perform imaging studies in the ophthalmology clinic was developed. Figure 2-10 is a schematic of the clinical ultrahigh resolution OCT system. The clinical system is similar in setup to the laboratory ultrahigh resolution OCT system. A dual-balanced detection configuration utilizing two fiber couplers

(FC) was used to remove the excess intensity noise of the portable Titanium:sapphire laser. Variable-thickness fused-silica (FS) and BK7 prism pairs were used in the reference arm to compensate for the dispersion mismatch between the sample arm and reference arm optics, and polarization controllers (PC's) were used to adjust for polarization mismatch. In addition, the clinical ophthalmic ultrahigh resolution OCT system also includes a 24 mm water cell in the reference arm to compensate for the dispersion mismatch in the sample arm caused by the vitreous of the eye. The sample arm optics is integrated into a slit-lamp biomiscroscope to provide a simultaneous viewing of the OCT beam on the retina in order to facilitate aiming the OCT beam onto different retinal structures. Two galvanometer scanners in the sample arm can generate any arbitrary scan patter on the retina in both X and Y directions. A fixation target (i.e., a black crosshair) is presented in the optical path of the slitlamp that will allow the subject to fixate the eye motion onto the internal slitlamp target.

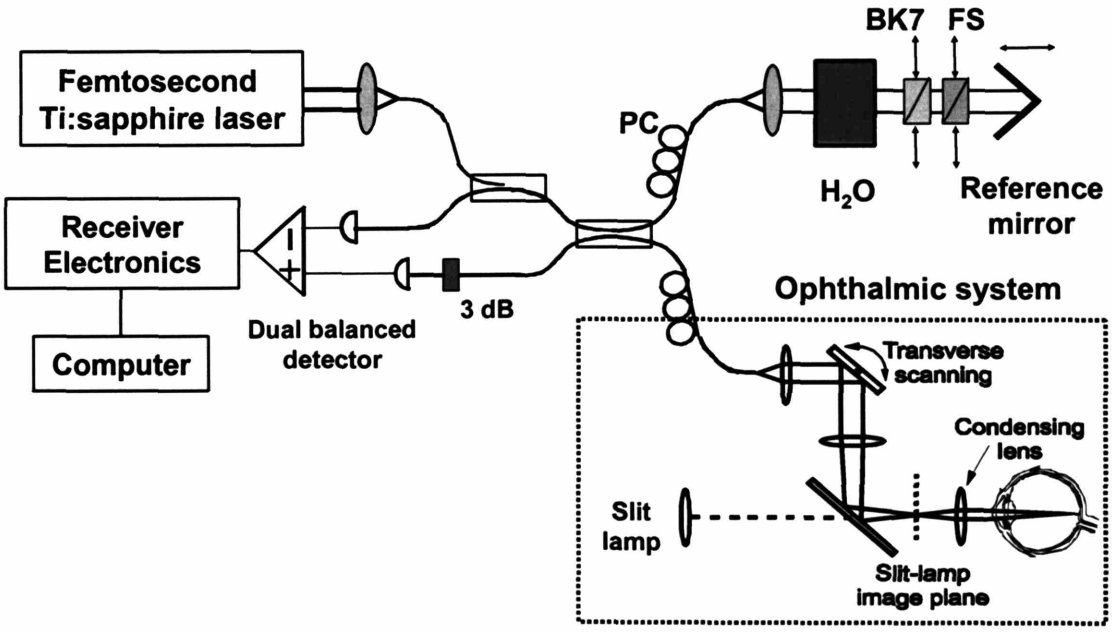

Figure 2-10. Schematic layout of the clinical ultrahigh resolution ophthalmic OCT system. Dispersion matching elements (H_2O, BK7, FS) are placed in the reference arm to balance the dispersion introduced by additional optical elements and the vitreous of the eye in the sample arm.

Ultrahigh resolution OCT imaging with this system is performed within well-established safe retinal exposure limits established by the ANSI standard.[11] For safety during retinal imaging, the femtosecond pulses are dispersively broadened by a 100-meter long optical fiber before entering the OCT system in order to increase the pulse duration and reduce the peak intensities by several order of magnitudes. Since the laser operates at 50 MHz repetition rate, the output can be considered as a continuous wave rather than pulsed from the laser safety standpoint. The ANSI standard for safe retinal exposure accounts for wavelength, duration, and multiple exposures of the same spot on the retina. Since the laser source used in this system generates broad bandwidth light, the shortest wavelength will have the most stringent exposure limits according to the ANSI standard. For the wavelengths and scanning conditions used in this study, the ANSI standard for maximum permissible ocular exposure is 1 mW (for 700 nm center wavelengths) and 1.54 mW (for 800 nm center wavelengths), assuming 30 consecutive scans in the same spot. For the clinical system, ultrahigh resolution OCT imaging was performed using up to 750 μW of incident optical power in the OCT scanning beam; this is the same incident optical power as used by the commercial StratusOCT system.

In order to increase the imaging speed of the clinical ultrahigh resolution OCT system, the linear scanning speed of the reference arm mirror was increased to 410 mm/s. An axial scan of about 2 mm in reference arm was typically used for OCT imaging in the retina. The 2 mm scanning in the reference arm achieves about 1.5 mm longitudinal scanning in the retina due to the index of refraction difference between air and tissue ($n \approx 1.33$ in tissue). For a typical ultrahigh resolution OCT image of about 600 total A-scans, the high reference arm scanning rate of 410 mm/s can achieve an imaging time of ~4 seconds accounting for the return of the reference arm galvanometer to the start of each A-scan. This imaging time is sufficiently short for most patients to maintain fixation without blinking during each 600 A-scan OCT image. According to equation 2.1, the increase in the scanning speed increases the Doppler frequency of the system to about 1 MHz. The bandpass filter has a center frequency of 1 MHz and a passband bandwidth of 170 kHz. The increase in imaging speed and the NEB (noise equivalent bandwidth) will decrease the SNR performance of the clinical OCT system. To partially compensate for this drop in SNR sensitivity, a different dual-balanced configuration was implements. Figure 2-11 shows the asymmetric dual-balanced interferometer configuration that was used in the clinical ultrahigh resolution OCT system. In the ophthalmic application, the total

amount of power that can be delivered to the sample arm is limited by the ANSI standard for safe retinal exposure, which in our case was 750 μW of incident optical power. Since the femtosecond laser can generate much higher output power than necessary for delivery of 750 μW onto the sample arm, the asymmetric dual-balanced interferometer was implemented. In this configuration, an 80/20 coupler was used as the first interferometer. Therefore, 80% of the output power from the laser was immediately dumped to the unused port and only 20% of the output was sent to the second 50/50 coupler of the OCT system. The power available for the sample arm is only (0.2 x 0.5) P_o, but it is sufficient to provide 750 μW of incident optical output power. On the return path to the photodetectors, 0.5 S of the interference signal S is available at the first photodiode while (0.8 x 0.5) S is available at the second photodiode. Comparing to the single detector interferometer design, 0.4 S is about 1 dB less than the 0.5 S detected by the signal detector. Therefore, this dual-balanced design using 80/20 and 50/50 interferometers was able to improve the SNR performance of the ultrahigh resolution OCT system by about 5 dB over the single interferometer design. This is about 2 dB more improvement than the conventional dual-balanced detection configuration, with two 50/50 couplers, used in the laboratory ultrahigh resolution OCT system.

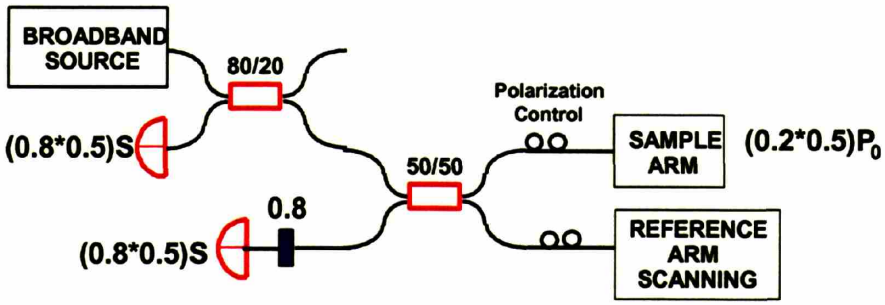

Figure 2-11. Dual-balanced detection using asymmetric 80/20 and 50/50 interferometers. Increased signal recovery means higher SNR improvement at a cost of less power available for imaging the sample.

Ideally, one would want to implement a broadband optical circulation in place of the 80/20 coupler so that all the input power from the laser can be delivered to the 50/50 coupler of the OCT system and 0.5 S of the interference signal S is available at the second photodiode. This configuration would lead to a 6 dB improvement in SNR sensitivity over the single

interferometer design. However, a broadband circulator suitable for the wavelengths used in this ultrahigh resolution OCT system does not currently exist and high split ratio couplers (e.g. 80/20 or 90/10 couplers) can be used to simulate the effect of the circulator as long as sufficient power is supplied to the sample arm for retinal imaging.

Using the asymmetric dual-balanced detection configuration along with the operating parameters of the clinical ultrahigh resolution OCT system (i.e., 750 μW incident optical power, 410 mm/s reference scanning, 170 kHz bandpass filter bandwidth), the typical SNR performance achieved was ~94-95 dB. This SNR sensitivity is sufficient for acquiring high contrast retinal OCT images, sometimes even from patients with slight or moderate cataracts.

2.3 References

1. Schuman JS, Puliafito CA, Fujimoto JG. Optical coherence tomography of ocular diseases, 2nd edition. Thorofare, NJ: Slack Inc., 2004.

2. Youngquist R, Carr S, Davies D. Optical coherence-domain reflectometry: a new optical evaluation technique. Optics Letters 1987;12(3):158-60.

3. Takada K, Yokohama I, Chida K, Noda J. New measurement system for fault location in optical waveguide devices based on an interferometric technique. Applied Optics 1987;26:1603-8.

4. Gilgen HH, Novak RP, Salathe RP, et al. Submillimeter optical reflectometry. IEEE Journal of Lightwave Technology 1989;7:1225-33.

5. Swanson EA, Huang D, Hee MR, et al. High-speed optical coherence domain reflectometry. Optics Letters 1992;17:151-3.

6. Morgner U, Kartner FX, Cho SH, et al. Sub-two-cycle pulses from a Kerr-lens mode-locked Ti:sapphire laser. Optics Letters 1999;24(6):411-3.

7. Drexler W, Morgner U, Kartner FX, et al. In vivo ultrahigh-resolution optical coherence tomography. Optics Letters 1999;24(17):1221-3.

8. Takada K. Noise in optical low-coherence reflectometry. Ieee Journal of Quantum Electronics 1998;34(7):1098-108.

9. Kowalevicz AM, Schibli TR, Kartner FX, Fujimoto JG. Ultralow-threshold Kerr-lens mode-locked Ti:Al2O3 laser. Optics Letters 2002;27(22):2037-9.

10. Drexler W, Morgner U, Ghanta RK, et al. Ultrahigh-resolution ophthalmic optical coherence tomography. Nature Medicine 2001;7(4):502-7.

11. American National Standards Institut (1993) Safe Use of Lasers, ANSI Z 136.1. New York: American National Standards Institute, 1993.

CHAPTER 3: IMAGING SMALL ANIMAL RETINA

In order to demonstrate ultrahigh resolution optical coherence tomography (UHR-OCT) imaging, seminal studies on developmental biology specimens were conducted using the laboratory based system with the microscope delivery. Because a larger numerical aperture focusing is possible, much better transverse resolution may be achieved compared to that in the human eye. Figure 3-1 shows an example of an ultrahigh resolution image of cellular structures in the Xenopus laevis tadpole *in vivo*. These imaging studies demonstrate that with ~1 μm axial and ~5 μm transverse resolutions, the laboratory ultrahigh resolution OCT system has the ability to tremendously enhance the visualization of fine tissue microstructures.[1]

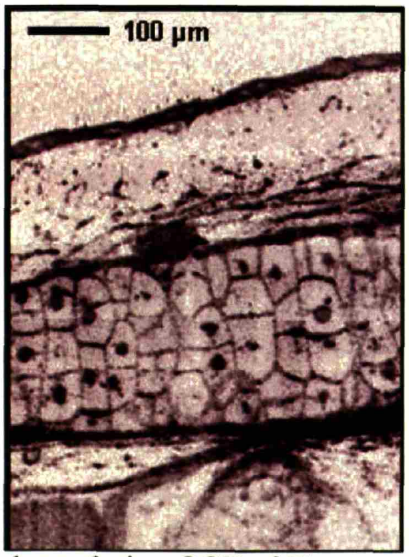

Figure 3-1. Ultrahigh resolution OCT of Xenopus laevis *in vivo* with ~1 μm axial and ~5 μm transverse resolution.[1]

3.1 Small Animal Models of Retinal Disease

Mouse models of retinal disease have been shown to be useful in understanding the cellular and molecular processes associated with retinal degenerative diseases.[2, 3] Mouse models of retinal degeneration have been investigated for many years in the hope of understanding the cause of photoreceptor cell death.[4] Conventionally, it has been difficult to monitor the retinal structural changes of the rodent eye without killing the animal for retinal histology. With histology, however, the retinal morphology through the course of retinal degeneration can not be studied non-invasively in a single animal. Therefore, each animal contributes only to a single time point for the overall understanding of the full disease progression. Consequently, large numbers of animals must be sacrificed in order to obtain convincing experimental results as population variations among individual animals also need to be accounted for. The ability to observe the progression of a disease process through its entire course and its response to a therapeutic regimen in individual rodent models would greatly enhance the speed and reliability of testing for new pharmaceutics and would reduce the number of experimental animals required. Therefore, there is a need for rapid and non-invasive analysis of retinal morphology and/or degeneration in the small eyes of rodent models.

Rat models have also been used to study retinal degeneration[5] and diabetic retinopathy.[6] The streptozotocin-induced diabetic rat shows many of the early change associated with human diabetic retinopathy.[7] Animal studies with rat models of diabetic retinopathy can improve the understanding of the pathogenesis of the disease as well as provide the development of possible treatments for preventing diabetic retinopathy. Therefore, there is a need for a method to non-invasively track retinal morphology throughout the disease course and to analyze its response to possible treatment. The application of OCT to animal models of diabetic retinopathy can provide a noninvasive, quantitative assessment of early markers of retinal disease in diabetes and thus help elucidate the mechanisms of diabetic retinopathy.

The improved axial and transverse resolution of ultrahigh resolution optical coherence tomography over standard resolution optical coherence tomography (OCT) allows cross-sectional *in vivo* imaging of the small eyes of rodent models to be performed. OCT has been used to image the retina of animals with relatively large eye such as chicken and swine,[8, 9] but has not been widely applied for *in vivo* imaging of small animal models of retinal diseases.[10]

Ultrahigh resolution OCT has been utilized to study the retinal tissue preparations of pig eyes[11] and monkey eyes,[12] but no *in vivo* small animal imaging studies has been reported to date. Therefore, the demonstration of ultrahigh resolution OCT imaging in mouse and rat retina will have important implications for ophthalmology research with these animal disease models.

3.2 Ultrahigh Resolution OCT Imaging of Mouse Retina

The laboratory ultrahigh resolution OCT system was adapted to perform OCT imaging in the mouse eye. Because of the small size of the mouse eye (~2-3 mm in diameter), the laboratory ultrahigh resolution OCT system is desired for perform imaging studies with ~1 μm axial resolution and ~5 μm transverse resolution. The microscope delivery system was turned in the horizontal direction in order to accommodate imaging the eye of the mouse. Figure 3-1 depicts the sample arm setup for performing ultrahigh resolution OCT imaging of the mouse eye.

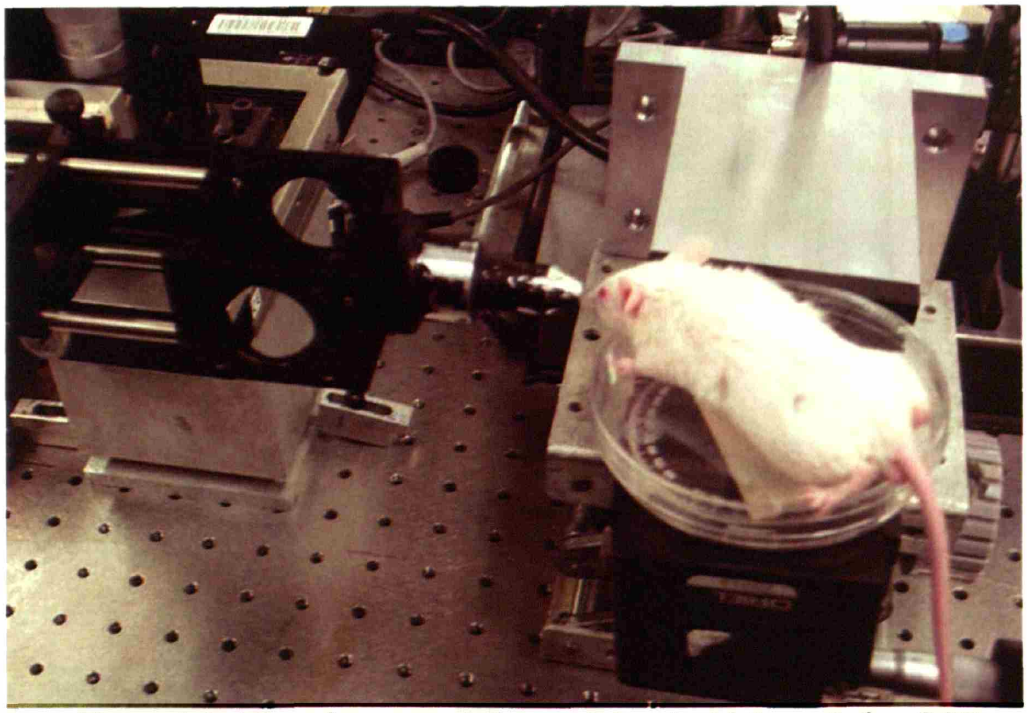

Figure 3-1. The microscope delivery of the ultrahigh resolution OCT system is turned horizontal to accommodate imaging the eye of the mouse. The animal is situated on a platform that allows 6-axis of adjustment.

The animal is placed on a platform that allows adjustments along 6 axes in order to position the eye of the animal in the most optimum position for OCT imaging. The animal is anesthized with Tribromoethanol (Avertin, 125-250 mg/kg) for the duration of the imaging period. A coverslip glass is placed, with the aid of goniosol solution, onto the cornea of the eye in order to remove the high corneal curvature of the animal's eye. By removing the corneal refraction of the animal, the OCT beam will be able to focuse directly onto the retina of the animal. In addition, this method also allows direct viewing of the fudus for positioning the animal onto retinal landmarks of interest before performing OCT imaging. Figure 3-2 demonstrates the ability to position the animal's fundus for direct viewing and OCT imaging around the optic disc.

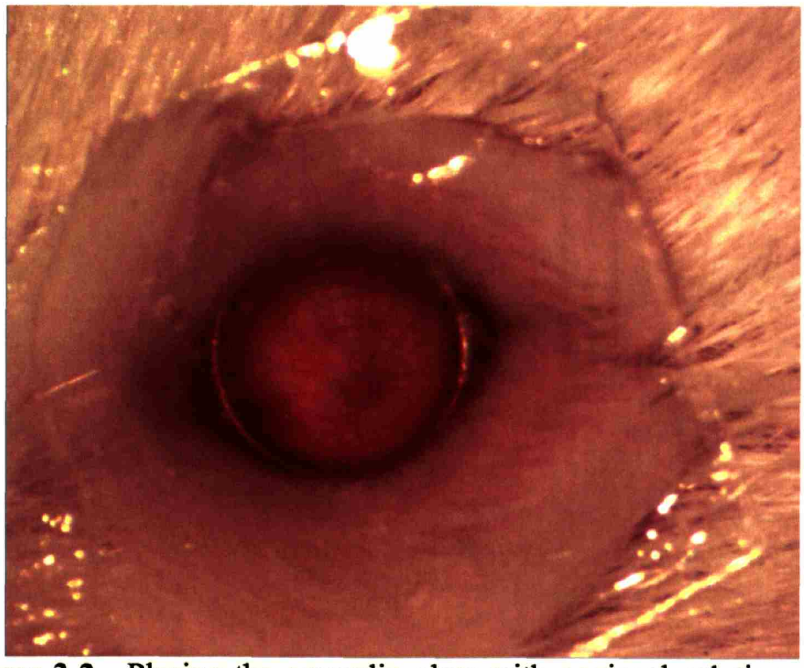

Figure 3-2. Placing the coverslip glass with goniosol solution onto the cornea allows direct viewing and positioning of the animal's fundus in preparation for OCT imaging.

The sample arm microscope is connected to translation stages in the X- and Y-direction which allows computer-controlled scanning of the retina for OCT imaging in the nasal-temporal as well as the superior-inferior directions. Figure 3-3 shows a textbook histology of the mouse retina with the major intraretinal layers identified and labeled. For comparison, Figure 3-4 shows an example of ultrahigh resolution OCT image of the mouse retina; the image was acquired from a normal mouse.

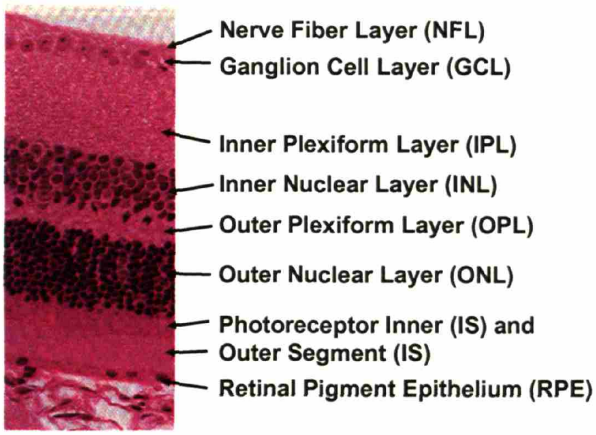

Figure 3-3. A textbook histology of the mouse retina (hematoxylin and eosin staining) showing all the major intraretinal layers.[13]

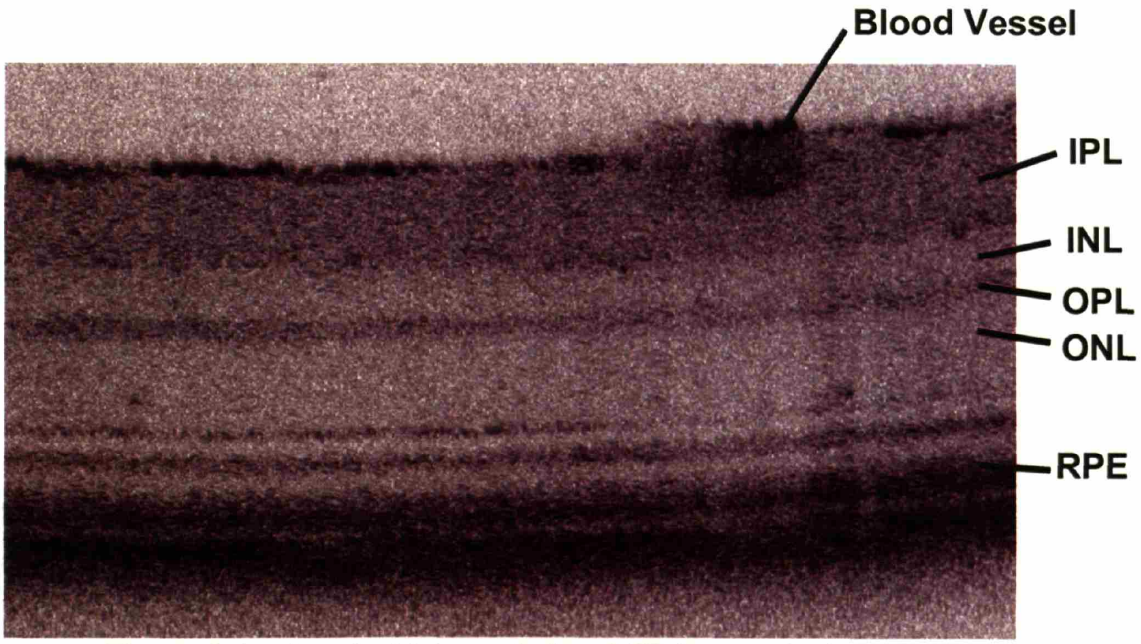

Figure 3-4. An ultrahigh resolution OCT image obtained from the mouse retina. The ultrahigh resolution OCT has the ability to visualize the major intraretinal layers.

Ultrahigh resolution OCT allows viewing of the major intraretinal layers that are identified in hematoxylin and eosin histology of the mouse retina. High organized layers such as the inner plexiform layer (IPL) and outer plexiform layer (OPL) appear to be highly backscattering in the OCT image (darker in appearance in Figure 3-4). The cellular nuclear layers such as the inner

nuclear layer (INL) and the outer nuclear layer (ONL) appear to be low back scattering (whiter in appearance in Figure 3-4). The OCT beam is highly scattered in blood so blood vessels have a darker, more highly backscattering appearance in the OCT image (Figure 3-4, blood vessel). The scattering and absorption in the blood vessels also attenuate the OCT beam which causes shadowing of the underlying retinal structures in the OCT image. In the outer retina, the retinal pigment epithelium appears to be the outermost highly scattering layer (Figure 3-4, RPE). The two highly backscattering lines above the RPE in the outer retina appear to be the external limiting membrane and the junction between the inner and outer segments of the photoreceptors. Therefore, the inner and outer segments are the low backscattering layers in between these high scattering junctions.

Imaging Retinal Degeneration Mouse Model

OCT imaging has not been widely applied to *in vivo* imaging of animal models of retinal degeneration. There is currently one study using standard resolution (~10 μm) OCT to study the retinal morphology in a retinal degeneration model.[10] In that study, OCT imaging of the mouse retina was correlated with conventional ERG and histology. However, Figure 3-5 shows that standard resolution OCT was not able to convincingly visualize the intraretinal layers and can only be used to detect total retinal thickness changes reliably.

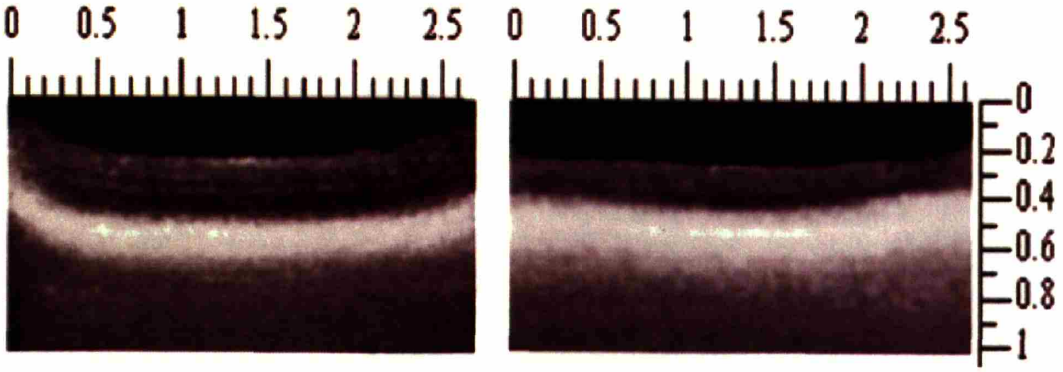

Figure 3-5. Standard resolution OCT image of the retinas of normal (left) and retinal degeneration (right) mice.[10] Intraretinal structures are hard to discern in standard resolution OCT image.

Ultrahigh resolution OCT would potentially have the ability to visualize all the intraretinal layers in order to identify the layer of retinal degeneration and track the morphologic changes occurring throughout the disease course. In order to demonstrate ultrahigh resolution OCT imaging in a retinal degeneration mouse model, imaging studies were performed in collaboration with Janice Lem, Ph.D. of Tufts University School of Medicine who has developed a rhodopsin knockout mouse model of retinal degeneration.

The rhodopsin knockout mouse model developed by Dr. Lem lacks both copies of the opsin gene.[14] These mice exhibit retinas that initially developed normally, except that rod outer segments failed to form. Within months of birth, photoreceptor cells degenerated completely.[14] Figure 3-6 demonstrates the difference in retinal development between normal wildtype mice and their rhodopsin knockout littermates.

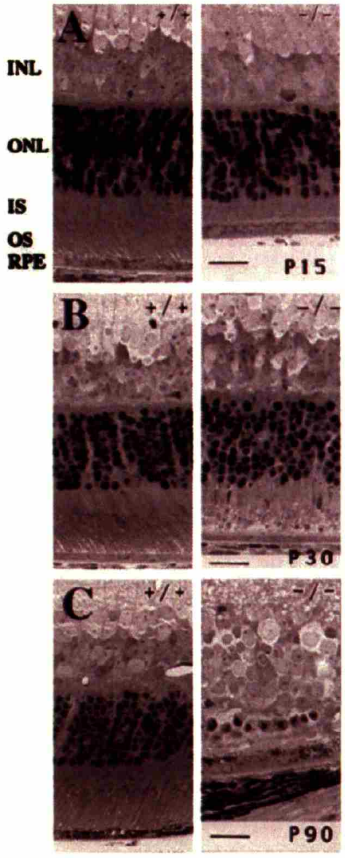

Figure 3-6. Retinal histology of (A) 15-day old, (B) 30-day old, and (C) 90-day old mice (Left, +/+ wildtype; Right, -/- rhodopsin knockout littermate).[14]

At 15 days, the outer nuclear layer (ONL) thicknesses for both wildtype and knockout mice were comparable at 10-12 rows of nuclei (Figure 3-6). However, photoreceptor outer segment was absent in the knockout mice retina. By 30 days, the ONL has developed to maximum thickness in the wildtype mice, but the ONL thickness was decreased by one or two rows in the knockout mice retina.[14] By 90 days, the retinal degeneration is nearly complete in the knockout mouse with little ONL thickness remaining compared to the normal wildtype mouse (Figure 3-6).

Ultrahigh resolution OCT imaging studies were performed in normal and rhodopsin knockout mice in order to demonstrate the ability of ultrahigh resolution OCT to track the development of retinal degeneration. Figure 3-7 shows the ultrahigh resolution OCT imaging results obtained from normal and knockout mice.

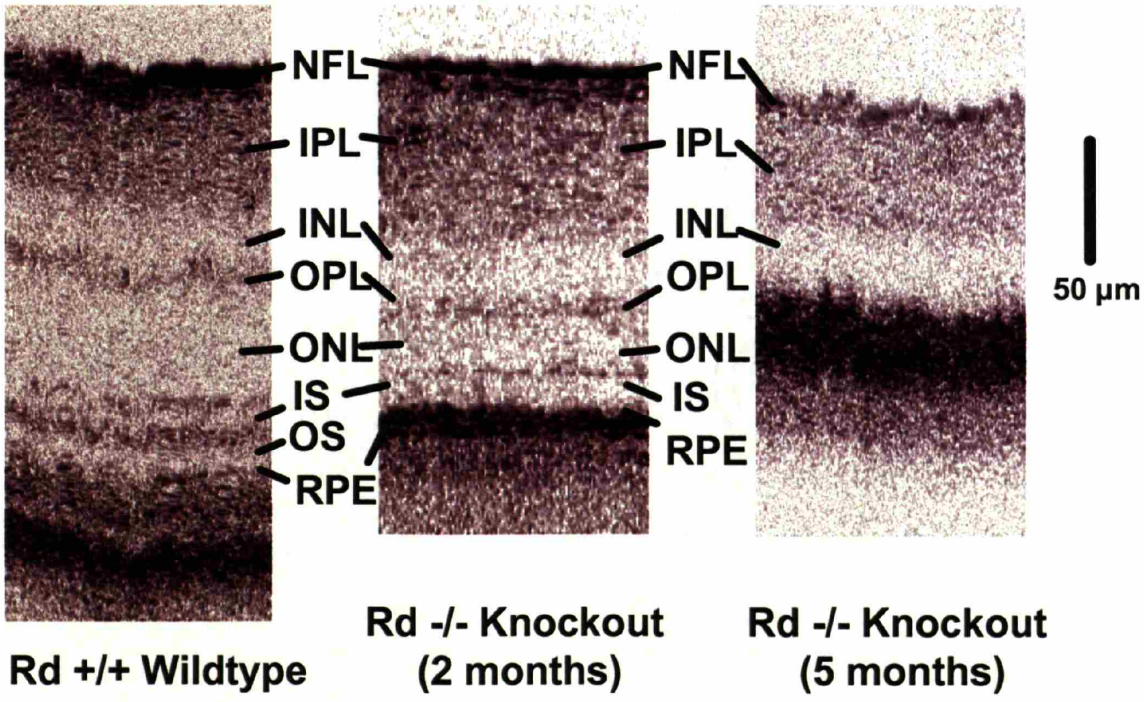

Figure 3-7. Ultrahigh resolution OCT retinal images of widetype mice (left), rhodopsin knockout mice at 2 months (center), and rhodopsin knockout mice at 5 months (right). The wildtype mouse retina exhibits normal intraretinal layer morphology while the outer retina of the knockout mice undergoes degeneration.

In the wildtype mouse retina, all major intraretinal layers were identified in ultrahigh resolution OCT. The photoreceptor inner and outer segments were also present in the wildtype retina above the retinal pigment epithelium (RPE) layer. In the rhodopsin knockout mouse retina at 2 months of age, all the intraretinal layers are present except for the photoreceptor outer segment which is missing. The outer nuclear layer (ONL) thickness at 2 months is already markedly thinner than the wildtype ONL thickness. In the rhodopsin knockout mouse retina at 5 months of age, all the outer retinal layers have completely degenerated in the ultrahigh resolution OCT image. The only intraretinal layers that appear to be present in this animal are the nerve fiber layer (NFL), inner plexiform layer (IPL), and the inner nuclear layer (INL). These results (Figure 3-7) demonstrate that ultrahigh resolution OCT can be used to visualize the major intraretinal layers of the retina and to detect morphological changes associated with retinal degeneration. The intraretinal changes correlates very well with the retinal degeneration changes observed in histology (Figure 3-6). By comparison, intraretinal features are hard to discern in standard resolution OCT imaging of the mouse retina (Figure 3-5). The ability to detect subtle changes in retinal structure associated with early disease is important because it provides a method to assess early detection, diagnosis and treatment possibilities. Furthermore, ultrahigh resolution OCT imaging is non-invasive and can be performed at multiple time points to investigate the progression of changes in retinal degenerative diseases in a single animal.

3.3 Ultrahigh Resolution OCT Imaging of Rat Retina

In addition to imaging mouse models of retinal degeneration, ultrahigh resolution OCT imaging was also demonstrated for imaging the rat retina. This study is performed in conjunction with collaborators at the Joslin Diabetes Center who are actively developing an injection model of diabetic retinopathy in rats. In this model of diabetic retinopathy, one eye of the rat serves as the study eye which would be injected with factors that would induce retinal leakage; the other eye serves as the control eye which would be injected with saline that would not induce any retinal changes. OCT imaging can then be performed on a single animal in both the study eye and the control eye in order to track the morphologic changes occurring in the retina at different time points following injection. Figure 3-8 shows an ultrahigh resolution OCT image of the retina obtained from the normal control eye of a rat.

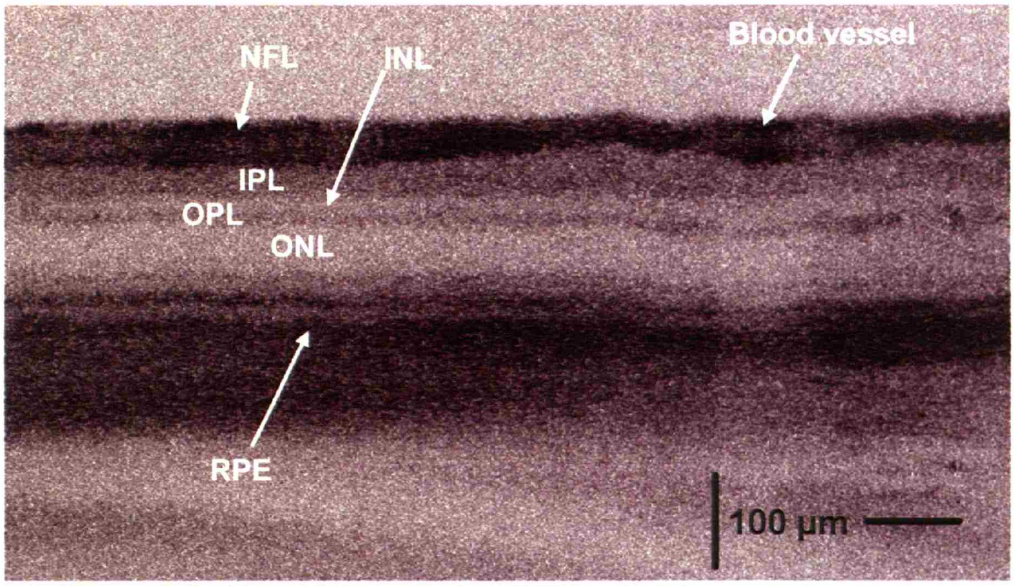

Figure 3-8. Ultrahigh resolution OCT retinal images of normal rat retina. Major intraretinal layers morphology of the NFL, IPL, INL, OPL, ONL, and RPE can be observed in this UHR-OCT image.

As expected, the normal retina of a rat exhibit all the major intraretinal layer that can be visualized in the ultrahigh resolution OCT of the normal mouse retina (Figure 3-4). Figure 3-9 shows an ultrahigh resolution OCT image of the retina obtained from the injected study eye of a rat 2 days following injection.

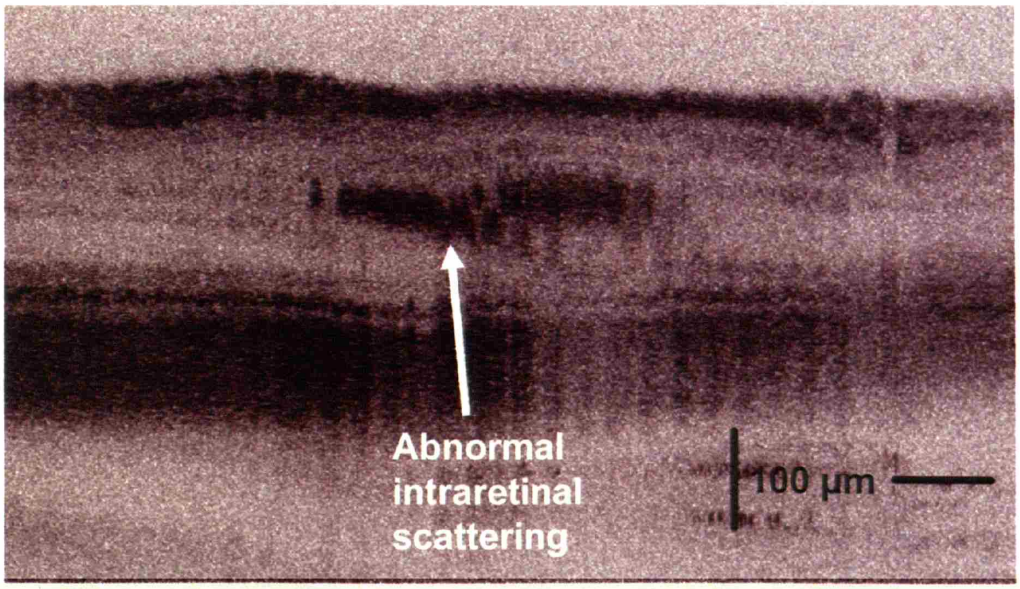

Figure 3-9. Ultrahigh resolution OCT retinal images of rat retina with induced diabetic retinopathy showing abnormal intraretinal changes.

The ultrahigh resolution OCT images acquired from the retina of the rat model indicate the ability of OCT to non-invasively detect and visualize intraretinal morphologic changes. Future studies would have to be conducted to validate the result seen in these preliminary studies and to ascertain the cause of these morphologic changes. The application of ultrahigh resolution OCT with animal models of diabetes can provide a noninvasive, quantitative assessment of early markers of retinal disease in diabetes and thus help elucidate the mechanisms of diabetic retinopathy and possible therapies. Performing ultrahigh resolution OCT imaging studies on animal models is also important in validating the technology before proceeding onto human and patient studies.

3.4 References

1. Drexler W, Morgner U, Kartner FX, et al. In vivo ultrahigh-resolution optical coherence tomography. Optics Letters 1999;24(17):1221-3.

2. Farber DB, Flannery JG, Bowesrickman C. The Rd Mouse Story - 70 Years of Research on an Animal-Model of Inherited Retinal Degeneration. Progress in Retinal and Eye Research 1994;13(1):31-64.

3. Hauswirth WW, Timmers AM. The eyes have it. Mol Med Today 2000;6(2):51.

4. Chang B, Hawes NL, Hurd RE, et al. Retinal degeneration mutants in the mouse. Vision Res 2002;42(4):517-25.

5. Lai YL, Jonas AM. Rat model for hereditary retinal degeneration. Adv Exp Med Biol 1977;77:115-36.

6. Yu DY, Cringle SJ, Su EN, et al. Pathogenesis and intervention strategies in diabetic retinopathy. Clin Experiment Ophthalmol 2001;29(3):164-6.

7. Su EN, Yu DY, Alder VA, et al. Altered vasoactivity in the early diabetic eye: measured in the isolated perfused rat eye. Exp Eye Res 1995;61(6):699-711.

8. Huang Y, Cideciyan AV, Aleman TS, et al. Optical coherence tomography (OCT) abnormalities in rhodopsin mutant transgenic swine with retinal degeneration. Exp Eye Res 2000;70(2):247-51.

9. Huang Y, Cideciyan AV, Papastergiou GI, et al. Relation of optical coherence tomography to microanatomy in normal and rd chickens. Invest Ophthalmol Vis Sci 1998;39(12):2405-16.

10. Li Q, Timmers AM, Hunter K, et al. Noninvasive imaging by optical coherence tomography to monitor retinal degeneration in the mouse. Investigative ophthalmology & visual science 2001;42(12):2981-9.

11. Gloesmann M, Hermann B, Schubert C, et al. Histologic correlation of pig retina radial stratification with ultrahigh-resolution optical coherence tomography. Investigative ophthalmology & visual science 2003;44(4):1696-703.

12. Anger EM, Unterhuber A, Hermann B, et al. Ultrahigh resolution optical coherence tomography of the monkey fovea. Identification of retinal sublayers by correlation with semithin histology sections. Exp Eye Res 2004;78(6):1117-25.

13. Hawes NL, Chang B, Hageman GS, et al. Retinal degeneration 6 (rd6): a new mouse model for human retinitis punctata albescens. Invest Ophthalmol Vis Sci 2000;41(10):3149-57.

14. Lem J, Krasnoperova NV, Calvert PD, et al. Morphological, physiological, and biochemical changes in rhodopsin knockout mice. Proc Natl Acad Sci U S A 1999;96(2):736-41.

CHAPTER 4: IMAGING NORMAL RETINA

Before performing patient imaging studies in the ophthalmology clinic with ultrahigh resolution OCT, imaging studies on normal subjects were conducted in order to evaluate the imaging performance and to understand the operational issues involved with the clinical ultrahigh resolution OCT system. In addition, a comparison between the StratusOCT images and the ultrahigh resolution OCT images of normal retina was made in order to understand the interpretation of the intraretinal layers seen in the ultrahigh resolution OCT images.

4.1 Interpreting Ultrahigh Resolution OCT Retinal Images

OCT imaging was performed on normal volunteers using both the standard resolution, commercially available StratusOCT and the clinical ultrahigh resolution OCT system. The StratusOCT image was generated using scans of 2 mm axial depth and 6 mm in the transverse direction. The StratusOCT image had ~10 μm axial and 20 μm transverse resolution in tissue and consisted of 1024 axial pixels and 512 transverse pixels. The pixel spacing was 2 μm/pixel in the axial direction and 12 μm/pixel in the transverse direction. The ultrahigh resolution OCT image was generated using scans with a 1.5 mm axial depth and 6 mm in the transverse direction. The ultrahigh resolution OCT image had ~3 μm axial and 15-20 μm transverse resolution in tissue and consisted of 3000 axial and 600 transverse pixels. The pixel spacing was 0.5 μm/pixel in the axial direction and 10 μm/pixel in the transverse direction. The standard StratusOCT imaging protocol was followed on both systems in order to facilitate a direct comparison of the resulting images. Six scans of 6-mm length were acquired at the macula and oriented at different angles separated by 30-degree intervals. A false-color image display,

similar to that used in the standard resolution StratusOCT instrument was chosen for the ultrahigh resolution OCT images in order to better facilitate comparison of images from the different systems. False-color images have the advantage that they can display a larger dynamic range than gray scale images because the observer can differentiate a wider range of colors than gray levels. However, it is important to note that color scales represent variations in backscattered or backreflected light and are not analogous to staining in histology.

It is helpful to first consider an ultrahigh resolution OCT image of a normal retina to understand the interpretation of the backscattering signals seen in the OCT images. Figure 4-1 shows a horizontal ultrahigh resolution OCT image of the fovea as well as a 2x enlargement of a portion of the image. This ultrahigh resolution OCT image was generated using 1.5 mm axial depth scan and was 3 mm long in the transverse direction. This short transverse scan length yields a higher pixel density image in the transverse direction than the standard 6 mm scan length of the clinical protocol.

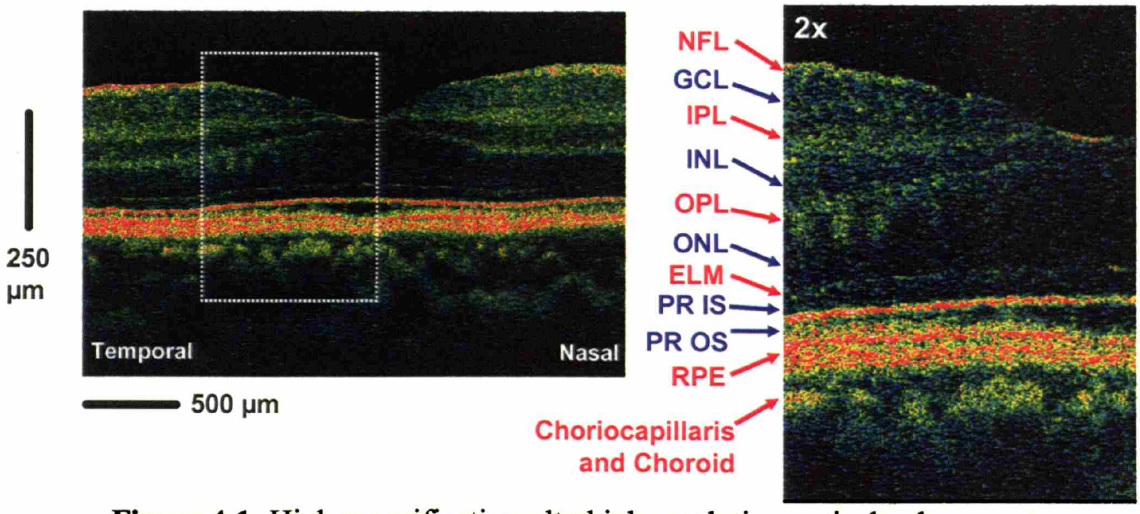

Figure 4-1. High magnification ultrahigh resolution optical coherence tomography image of the normal human macula. A 2x enlargement of image demonstrates the ability to visualize intraretinal layers that can be correlated with intraretinal anatomy - NFL: nerve fiber layer, GCL: ganglion cell layer, IPL: inner plexiform layer, INL: inner nuclear layer, OPL: outer plexiform layer, ONL: outer nuclear layer, ELM: external limiting membrane, PR IS, PR OS: photoreceptor inner and outer segments, RPE: retinal pigment epithelium. Red label: high backscattering layers, blue label: low backscattering layers.[1]

The architectural morphology of the intraretinal layers is well differentiated in the ultrahigh resolution OCT image and correlates with the well-known morphology of the retina in the foveal and parafoveal region.[2] These results from the normal human retina are much like the results obtained from the *in vivo* imaging studies of mouse and rat retina (Chapter 3). In addition, studies have been performed by others comparing ultrahigh resolution OCT images of pig and monkey retinal preparations to retinal histology, and the intraretinal features visualized in ultrahigh resolution OCT have good correspondence to the intraretinal features of retinal histology.[3, 4] The nerve fiber layer and the plexiform layers appear to be more optically backscattering than the nuclear layers and are seen as red or white false color in the OCT images.[5] Therefore, the first highly backscattering layer is the nerve fiber layer (NFL). The three, low backscattering intraretinal layers are the ganglion cell layer (GCL), inner nuclear layer (INL), and outer nuclear layer (ONL) and are seen as blue or black false color in the OCT images. These nuclear layers are adjacent to the optically backscattering layers of inner plexiform layer (IPL) and outer plexiform layer (OPL). The external limiting membrane (ELM) corresponds to the thin backscattering junction immediately below the outer nuclear layer (ONL). The junction between the photoreceptor inner segment (PR IS) and outer segment (PR OS) corresponds to the thin highly backscattering layer beneath the external limiting membrane.

The reflection arising from this junction of the inner and outer segment (IS/OS) may be the result of the abrupt boundary between the structures of the inner segments and the highly organized outer segments which contains stacks of membranous disc that are rich in the visual pigment rhodopsin.[6] This interpretation is supported in the OCT image by the increase in photoreceptor outer segment thickness in the foveal region that corresponds to the well-known increase in the length of the cone outer segments in this region. Outer segment thickness measurements (from ~20 μm in the parafovea to ~40 μm in the foveola) obtained from the ultrahigh resolution OCT image also agree well with recently published outer segment thickness measurements obtained from monkey and human retinal histology.[6] This new interpretation of the OCT signals observed in the outer retina corrects an error in earlier publications using standard and ultrahigh resolution OCT where the inner and outer segment boundary was incorrectly identified as the RPE.[7-9] The presence of a large reflection from the boundary between the photoreceptor inner and outer segments is surprising and this lead to an incorrect interpretation of this feature as the RPE. This misinterpretation was introduced when the first *in*

vivo OCT retinal imaging was performed in 1993.[7, 8] The origin of the high reflection from the interface between the photoreceptor inner and outer segments is not well understood. One possible explanation comes from the photoreceptor outer segment which contains stacks of membranous disc that are rich in the visual pigment rhodopsin and has waveguiding behavior.[10-12] The densely stacked disc membranes of the outer segments have high refractive indices than the inner segment,[6] which is probably the physical basis that the interface between inner and outer photoreceptor segments can cause a highly backreflecting OCT signal.

The melanin-containing retinal pigment epithelium (RPE) is very strongly backscattering and is visualized in the OCT image as the bright layer below the low scattering photoreceptor outer segment. The vascular choriocapillaris and chroidal structures are visualized as the optically backscattering structure underneath the RPE. These vascular structures are highly scattering and limit the penetration of light and the imaging depth of OCT for deeper structures underneath the choroid.

Figure 4-2 shows representative StratusOCT and ultrahigh resolution OCT cross-sectional images of the macula of a normal subject. Due to the long 6 mm transverse scan of the OCT images, different vertical and horizontal scaling has been utilized to display the OCT images in order to enhance viewing of retinal structures in the longitudinal direction. In addition, edge regions in both OCT images were cropped due to the large axial scan range. A single refractive index was assumed for all retinal layers because the exact difference in refractive index between the retinal layers in not currently known. Comparison of the standard resolution OCT image (top) to the ultrahigh resolution OCT image (bottom) of the normal human macula shows that most major intraretinal layers such as the NFL, IPL, INL, OPL, ONL, and RPE can be well visualized in the standard resolution OCT image. The ganglion cell layer (GCL) is poorly backscattering and may not be as clearly visualized in the standard resolution OCT image. The thin layer corresponding to the ELM is also not as easily visualized in the standard resolution OCT image. However, in the foveal region where the distance between ELM and RPE is larger, the external limiting membrane can sometimes be differentiated in the standard resolution OCT image. The junction between the photoreceptor inner and outer segments (IS/OS) is highly backscattering and can be visualized in both OCT images. The RPE is also highly backscattering and are visualized in both OCT images. The identification of structures such as the GCL, ELM, RPE, and IS/OS junction in the standard resolution OCT

image can be facilitated by using the ultrahigh resolution OCT image as a baseline for determining the relative locations of these layers.

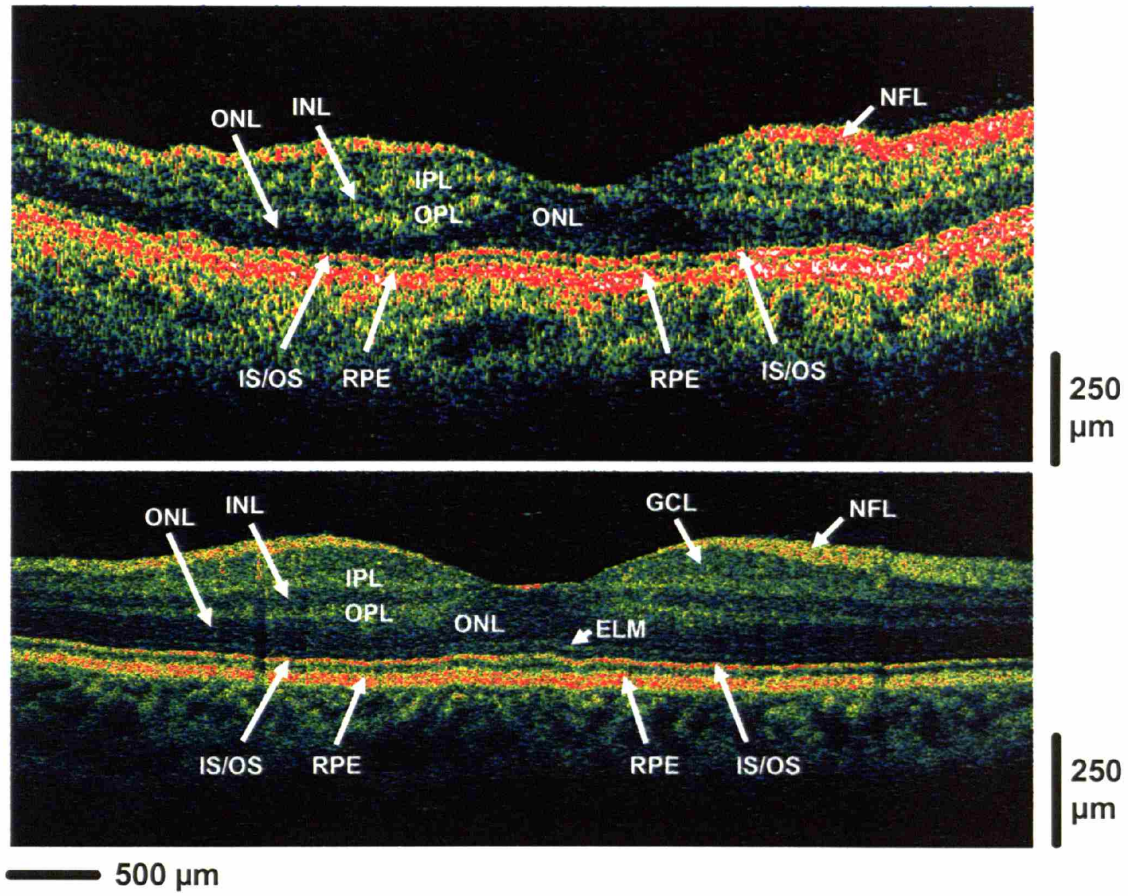

Figure 4-2. Standard resolution StratusOCT (top) and ultrahigh resolution OCT (bottom) images of normal human macula. Most of the major intraretinal layers can be visualized in the StratusOCT image, but fine structures such as the ganglion cell layer and external limiting membrane are much better visualized in the ultrahigh resolution OCT image.[1]

The StratusOCT performs imaging at 400 A-scans per second and can acquire a 512 A-scan OCT image in 1.3 seconds. The clinical ultrahigh resolution OCT system performs imaging at 150 A-scans per second and requires 4 seconds to acquire a 600 A-scan ultrahigh resolution OCT image. Since the imaging time is slower in ultrahigh resolution OCT, more axial motion is present during the acquisition of the high resolution images. Therefore, all ultrahigh resolution OCT images have been processed to correct for axial motion. Assuming that adjacent axial

scans will have similar backscattering profile, the relative axial motion between successive A-scans can be determined by finding the cross-correlation between the two. Shifting the second axial scan by the amount of the cross-correlation term will correct out the subject's motion in the axial direction. These algorithms have been used in all of the previous prototype and commercial OCT systems.[7] The StratusOCT images are usually not corrected for axial motion because axial motion is usually not significant so the commercial software only exports uncorrected raw images. Nevertheless, we have also developed software to correct the raw StratusOCT images in cases where axial motion is substantial.

4.2 Retinal Mapping of Normal Macula

Ultrahigh resolution OCT imaging enhances the visualization of different intraretinal layers over standard resolution StratusOCT. The improved axial resolution also leads to better segmentation of the intraretinal layers. In StratusOCT imaging, the only intraretinal layer that the commercial software performs segmentation on is the highly backscattering nerve fiber layer (NFL) that is segmented when circumpapillary OCT scans are performed. Figure 4-3 demonstrates segmentation of the different intraretinal layers in the normal human macula with ultrahigh resolution OCT imaging. Image processing and segmentation algorithm can be performed on the retinal boundaries and intraretinal layers of the ultrahigh resolution OCT image. An automated algorithm can then be used to detect different intraretinal boundaries that depict the different layers. In the macula, the layers that can be segmented from the image easily are the nerve fiber layer (NFL), the inner nuclear layer (INL), and outer plexiform layer (OPL), the outer nuclear layer (ONL), and the inner and outer segment junction and the RPE. The ganglion cell layer (GCL) does not have enough contrast against adjacent structures to be reliably segmented in these OCT images; therefore, the entire ganglion cell layer and inner plexiform layer (GCL+IPL) is usually segmented together. Figure 4-4 demonstrates segmentation of the different intraretinal layers along the maculopapillary axis (from the fovea to the optic disk). Along the maculopapillary axis, the nerve fiber layer increases in thickness until it reaches the optic disk. In contrast, the ganglion cell layer and inner plexiform layer (GCL+IPL) decreases in thickness as it moves away from the fovea towards the optic disk. These anatomical variations are clearly visualized in the retinal thickness plots (Figure 4-4).

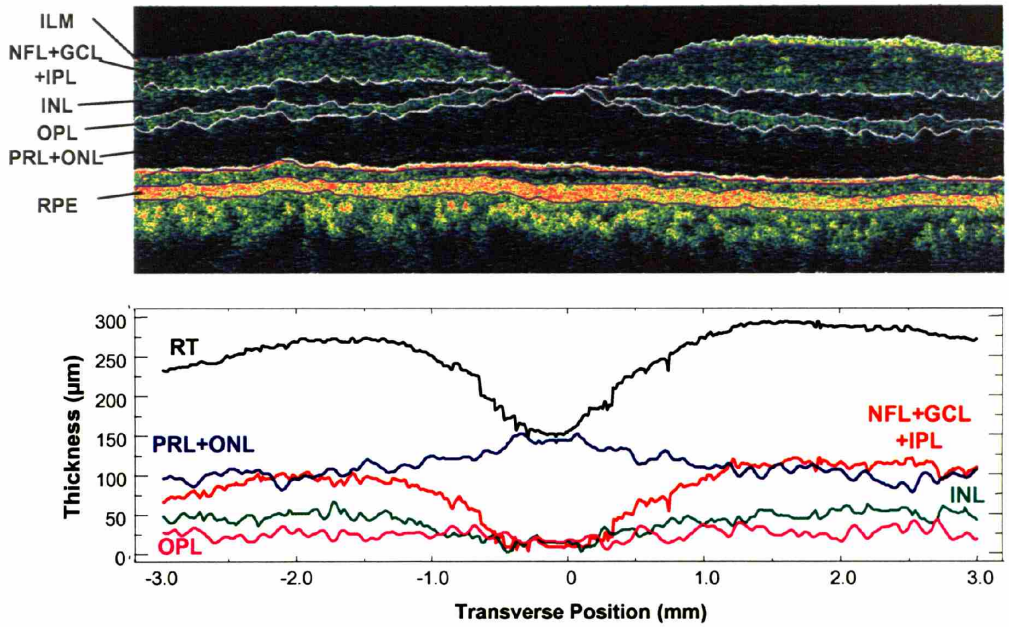

Figure 4-3. (Top) Ultrahigh resolution OCT enhances the segmentation of intraretinal layers in the macula. **(Bottom)** The thickness measurements of the segmented layer plotted as a function of transverse position from the fovea. RT = Total retinal thickness.

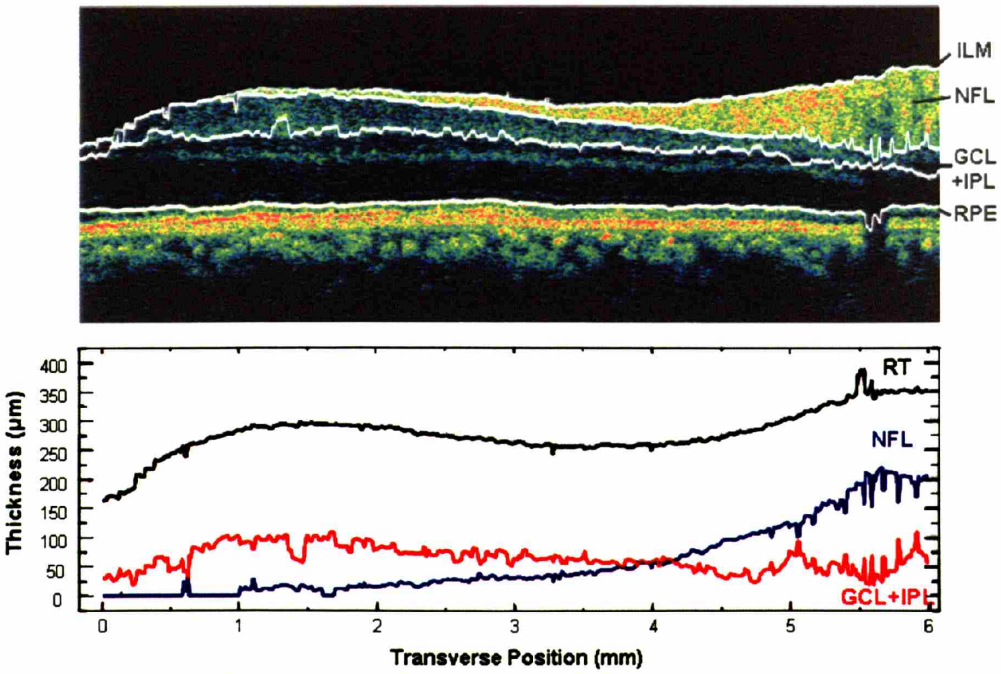

Figure 4-4. (Top) Ultrahigh resolution OCT and layer segmentation along the maculopapillary axis. **(Bottom)** The thickness measurements of the segmented layer plotted as a function of transverse position away from the fovea. RT = Total retinal thickness.

Since ultrahigh resolution OCT imaging enables the segmentation of intraretinal layers, thickness mapping of different intraretinal layers is also a possibility. Figure 4-5 depict thickness mapping of the macular region with ultrahigh resolution OCT. Seven ultrahigh resolution OCT scans were acquired in the macular region of the eye. Total retinal thickness as well as intraretinal layer thickness can be segmented and plotted in different thickness maps of the macula. Thickness maps of the ganglion cell layer, in particular, has clinical implications in the early detection of glaucoma since ganglion cells in the macula of the retina are lost in glaucoma.[13, 14] The ability to track thickness changes in the ganglion cell layer using such a macular thickness map may enhance the detection of glaucomatous changes as well as monitor the patient's response to treatment.

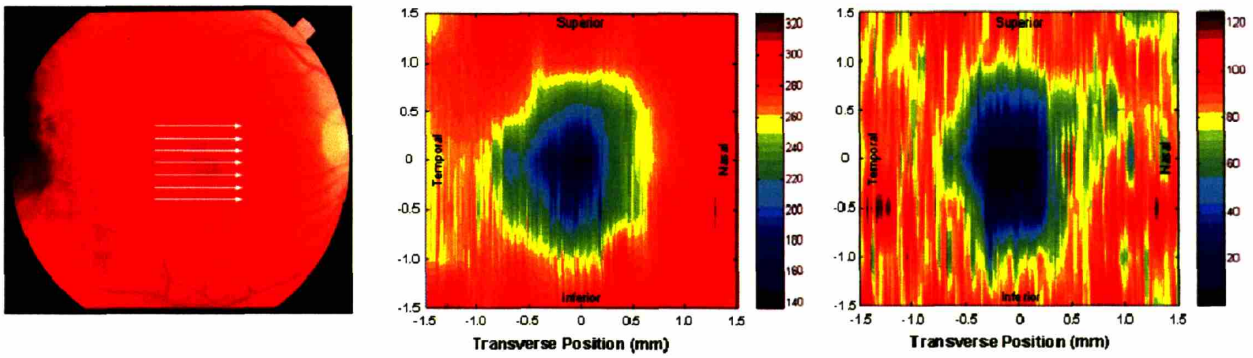

Figure 4-5. (Left) Seven ultrahigh resolution OCT scans were acquired in the macula in order to perform macula thickness mapping. **(Center)** Thickness map (in μm) of the total retinal thickness in the macula. **(Right)** Thickness map (in μm) of the ganglion cell layer and the inner plexiform layer. This map is a good representation of ganglion cell layer thickness as inner plexiform layer thickness in the macula is generally uniform.

Figure 4-6 depicts the thickness mapping along the maculopapillary axis with ultrahigh resolution OCT. Ten ultrahigh resolution OCT scans were acquired with equidistant spacing from the fovea to the optic disk. Intraretinal layer thickness maps such as the variation of the nerve fiber layer thickness from the fovea to the optic disk can be plotted and monitored for thickness changes that may be associated with diseases such as glaucoma.

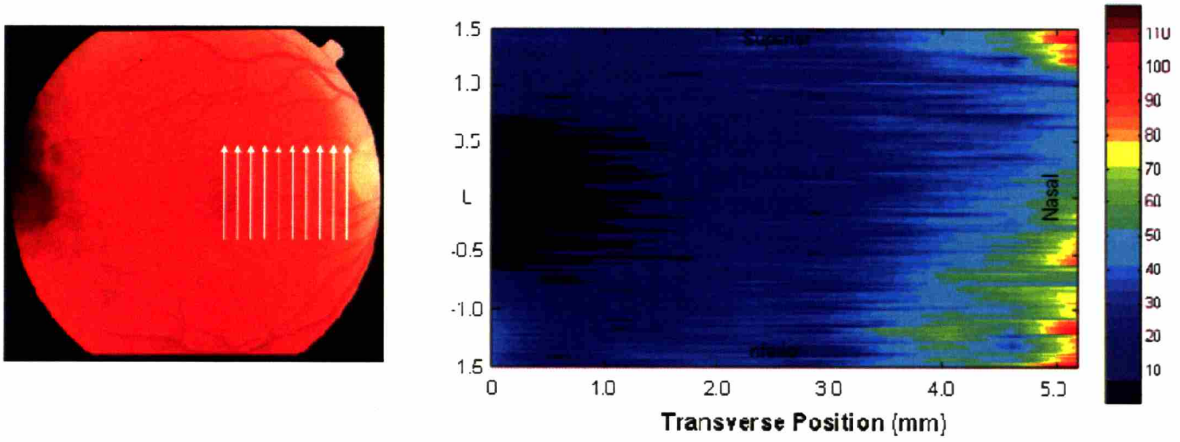

Figure 4-6. (Left) Ten ultrahigh resolution OCT scans were acquired in the maculopapillary axis in order to perform thickness mapping. **(Right)** Thickness map (in μm) of the nerve fiber layer as it varies from the fovea towards the optic disk.

4.3 OCT Axial Resolution vs. OCT Image Quality

For clinical application, it is interesting to understand the relationship between OCT axial resolution and the quality of the acquired OCT images from the retina. This information will be useful in determining the minimum OCT resolution that would continue to achieve enhancement of retinal feature visualization to yield additional diagnostic information. Consequently, this OCT resolution would determine the minimum source bandwidth requirements of future commercial ultrahigh resolution OCT system. In general, broadband light sources such as femtosecond lasers are prohibitively expensive for implementation into a commercial OCT imaging instrument. By determining the OCT resolution that can still achieve the diagnostic promise of ultrahigh resolution OCT imaging, the source bandwidth requirements and therefore the cost of a future commercial devices can therefore be reduced while still achieving the desired clinical performance. Another objective of this study is to determine to what extent the chromatic and other possible aberrative effects of the eye limit the maximum achievable axial resolution of *in vivo* ophthalmic OCT retinal images. It has been previously reported that the chromatic aberration of the eye would likely limit the maximum achievable OCT resolution to ~3 μm in the human eye.[9]

Source Bandwidth and OCT Axial Resolutions

In this study, we compared ophthalmic OCT imaging over a wide range of axial image resolutions. According to equation 2.2, different OCT axial resolutions can be achieved by using broadband sources with different bandwidths (assuming similar center wavelengths). Figure 4-7 indicates the relationship between source bandwidth and the OCT axial resolution in the eye. Assuming a center wavelength of 800 nm, the StratusOCT source of 25 nm would yield an OCT resolution of ~10 μm. In collaboration with Andrew Kowalevicz from our group, the laboratory based Titanium:sapphire laser was adjusted to yield different output bandwidths in order to achieve ophthalmic OCT imaging at different axial resolutions. The laser bandwidths used for this investigation was 33 nm, 60 nm, 122 nm, and 215 nm bandwidth and figure 4-7 indicates the predicted OCT resolution assuming Gaussian shaped spectra.

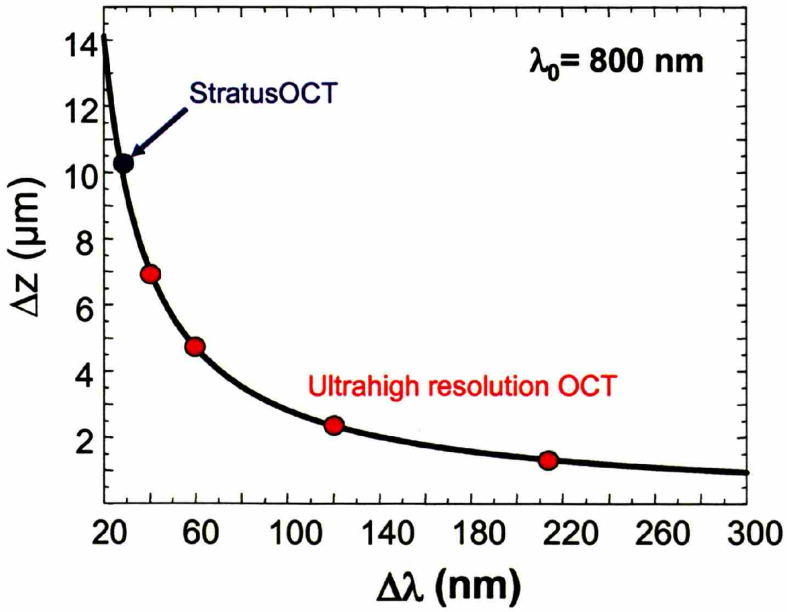

Figure 4-7. The relationship between OCT axial resolution and source bandwidth for a central wavelength of 800 nm. The StratusOCT light source yields an OCT resolution of 10 μm while the femtosecond laser can be adjusted to yield different output bandwidths and different OCT axial resolutions.

The curve in Figure 4-7 indicate the absolute limit of axial resolution for ideal optics in the OCT imaging system and sample arm. However, real systems exhibit a decrease in achievable resolution due to non-ideal spectral shape of the light source, wavelength dependence of the

optical components in the OCT system, imperfect dispersion matching in the two interferometer arms, as well as other aberrative effects from the sample arm such as the chromatic aberration of the human eye.

OCT System Considerations

In most conventional OCT systems, the detected interferometric fringes are bandpass filtered and demodulated before being acquired by the computer's data acquisition card. The demodulation step minimizes the data rate as only the envelopes of the interferometric fringes are required for conventional OCT. However, the logarithmic demodulation can introduce artifacts that tend to broaden the axial resolution of the backreflected OCT signal, which will undermine the determination of the absolute best axial resolution in an OCT image. In this study, the filtered OCT interferometric fringes are also acquired by a high speed data acquisition card. The acquisition of the linear interferometric fringes will allow the determination of OCT axial resolution in a retinal image to be performed directed from the full-width half-maximum (FWHM) measurement of an isolated backreflection from the retina.

In addition, the signal-to-noise (SNR) performance of the OCT system is given by SNR = $10\text{Log}(\eta P)/(E \cdot NEB)$ where P is the power that is reflected or backscattered and NEB (noise equivalent bandwidth) is proportional to the bandwidth of the electronic detection. In order to achieve maximum SNR performance and to eliminate excess noise outside of the signal bandwidth, 3 different electronic bandpass filters were used. As the bandwidth of the optical spectra is increased, an electronic bandpass filter with larger bandwidth is required (equation 2-1), leading to an increase in the NEB. Therefore, there would be a drop in SNR performance at the highest OCT axial resolution in response to the increase in bandpass filter bandwidth. Table 4-1 summarizes the different operating parameters for the four different source bandwidths used in this study. The observed OCT axial resolution was obtained by placing a mirror in the sample arm and measuring the full-width half-maximum (FWHM) of the resulting OCT interferometric fringe. As the optical bandwidth is increased from 33 nm to 215 nm, the bandwidth of the bandpass filter also increased from 130 kHz to 250 kHz. This increase in the bandpass filter bandwidth leads a drop in SNR performance of the OCT system from 95 dB to 90 dB. The expected OT resolution in the eye was calculated from the measured OCT resolution in air (from

the mirror) by dividing the measured resolution by 1.33, the assumed index of refraction of the tissue, in order to account for the difference in index of refraction between air and tissue.

Source optical bandwidth (FWHM)	Observed OCT resolution in air (from mirror)	Bandwidth of the bandpass filter (3 dB)	SNR of OCT system (measured)	Expected OCT resolution in eye (calculated)
33 nm	9.5 μm	130 kHz	95 dB	7 μm
60 nm	6 μm	130 kHz	95 dB	4.5 μm
122 nm	3.2 μm	170 kHz	93 dB	2.4 μm
230 nm	2.4 μm	250 kHz	90 dB	1.8 μm

Table 4-1. The four different source optical bandwidths used in the investigation between axial resolution and OCT image quality. Broader source bandwidth leads to broader filter bandwidth which leads to a decrease in the SNR performance of the OCT system.

The observed OCT resolutions in air as measured from a mirror in the sample arm were 9.5 μm, 6 μm, 3.2 μm, and 2.4 μm respectively for source optical bandwidths of 33 nm, 60 nm, 122 nm, and 230 nm. The optical throughput limitation of the OCT system is apparent in that the observed OCT resolution in air is always broader than those expected from theoretical calculations. For example, for the widest source optical bandwidth of 230 nm, only a bandwidth of 215 nm was observed to have passed through the OCT system with the coincident drop in the axial resolution performance of the OCT system. The calculated OCT resolutions in the eye were 7 μm, 4.5 μm, 2.4 μm, and 1.8 μm respectively for source optical bandwidths of 33 nm, 60 nm, 122 nm, and 230 nm. At the broader source optical bandwidths of over 120 nm, Table 4-1 indicate that the expected OCT resolution in the eye is less than 3 μm. Should the chromatic aberration of the eye limit maximum achievable OCT resolution to ~3 μm in the human eye, we should observe no backreflected interference fringe from the retina with less than 3 μm axial resolution.

OCT Imaging Results

Figure 4-8 through Figure 4-11 show the OCT imaging results obtained from the four different source optical bandwidths of 33 nm, 60 nm, 122 nm, and 230 nm.

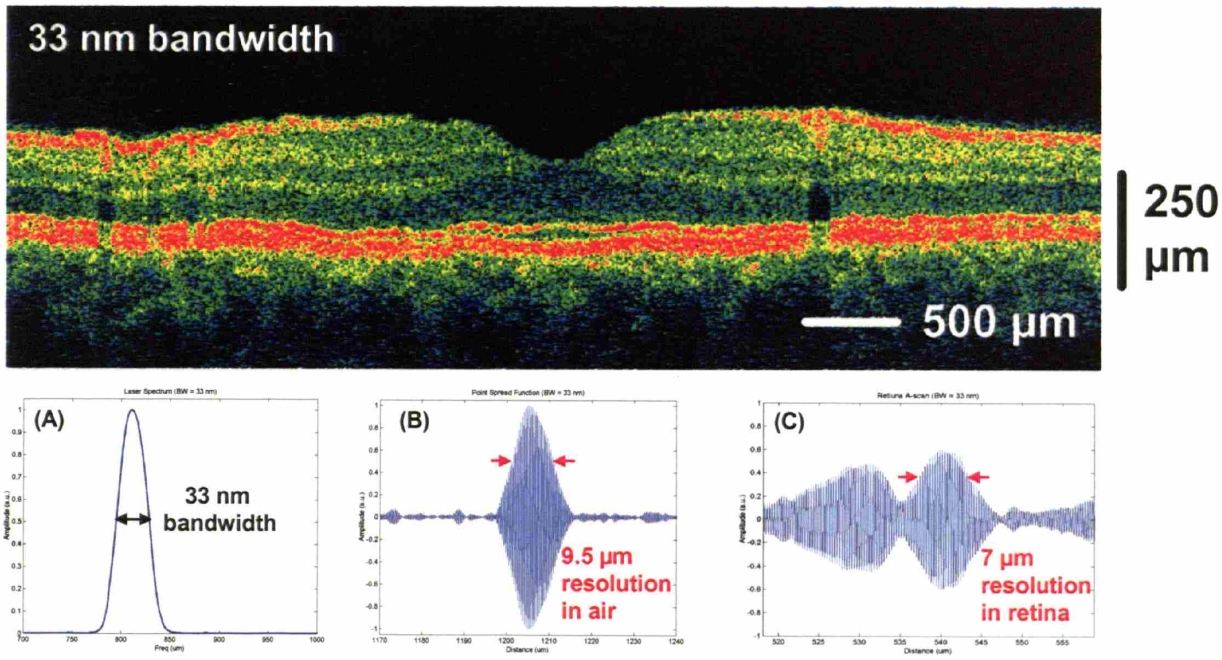

Figure 4-8. (Top) OCT image of the normal macula *in vivo* taken with (A) a 33 nm bandwidth laser which gives (B) 9.5 µm axial resolution in air and (C) 7 µm axial resolution in the retina.

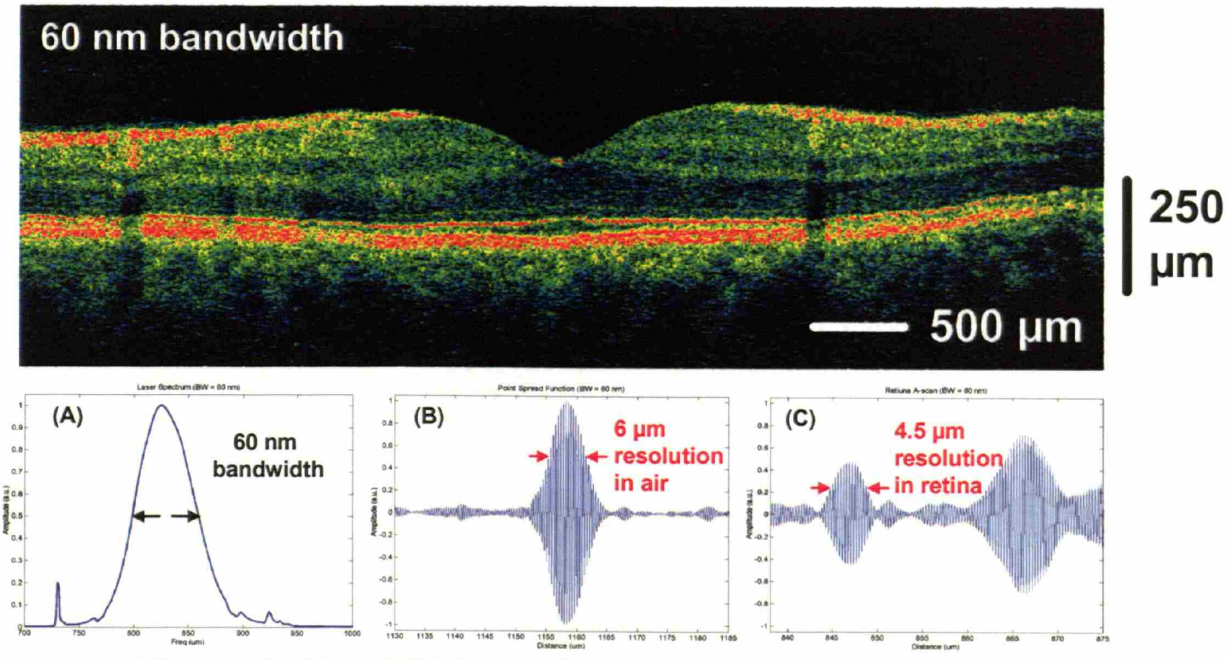

Figure 4-9. (Top) OCT image of the normal macula *in vivo* taken with (A) a 60 nm bandwidth laser which gives (B) 6 µm axial resolution in air and (C) 4.5 µm axial resolution in the retina.

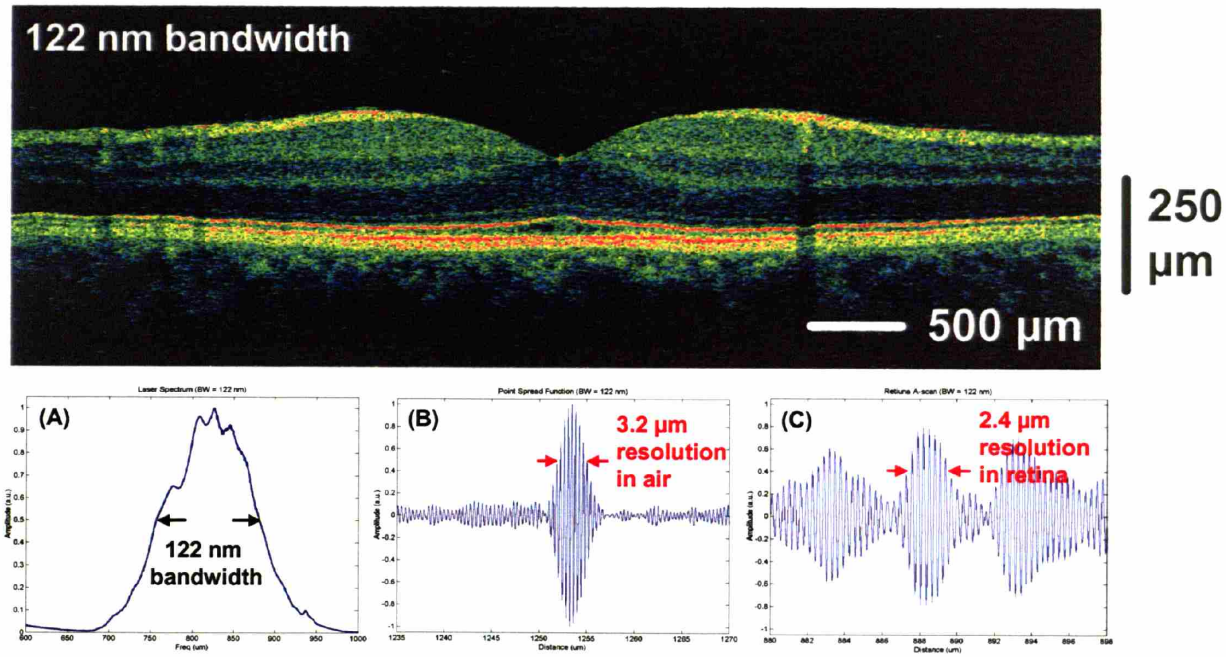

Figure 4-10. (Top) OCT image of the normal macula *in vivo* taken with (A) a 122 nm bandwidth laser which gives (B) 3.2 µm axial resolution in air and (C) 2.4 µm axial resolution in the retina.

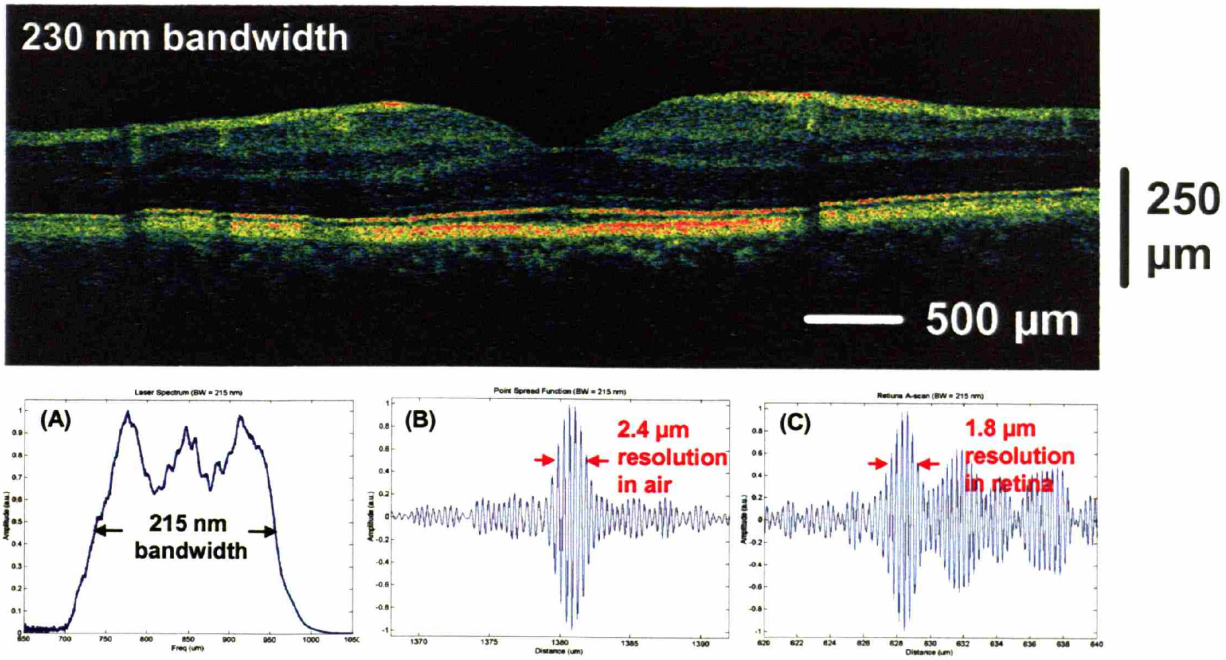

Figure 4-11. (Top) OCT image of the normal macula *in vivo* taken with 230 nm bandwidth laser resulting in (A) 215 nm bandwidth passing through the OCT system and (B) 2.4 µm axial resolution in air and (C) 1.8 µm axial resolution in the retina.

The OCT image acquired with 33 nm source bandwidth (Figure 4-8, top) is similar to the StratusOCT image in image quality and resolution. As in the StratusOCT images, fine intraretinal features (GCL, ELM) are more difficult to visualize than OCT images taken at ultrahigh resolutions. The expected 7 μm OCT axial resolution in the eye was observed in a Gaussian interference fringe obtained from an isolated retinal reflection in the axial scan (Figure 4-8 C).

This OCT image acquired with 60 nm source bandwidth (Figure 4-9, top) already has image quality that is very close to those obtained by the clinical ultrahigh resolution OCT system (Figure 4-2, bottom). Fine intraretinal features (GCL, ELM, photoreceptor segments) visualized in ultrahigh resolution OCT can already be recognized with this OCT resolution. The expected 4.5 μm OCT axial resolution in the eye was observed in a Gaussian interference fringe obtained from an isolated retinal reflection in the axial scan (Figure 4-9 C).

This OCT image acquired with 122 nm source bandwidth (Figure 4-10, top) has image quality that is similar to the OCT images taken with the clinical ultrahigh resolution OCT system (Figure 4-2, bottom). Fine intraretinal features (GCL, ELM, photoreceptor segments) are well visualized at this resolution. The expected 2.4 μm OCT axial resolution in the eye was observed in a Gaussian interference fringe obtained from an isolated retinal reflection in the axial scan (Figure 4-10 C).

OCT imaging using a 230 nm source bandwidth only resulted in 215 nm of the source passing through the OCT system. The OCT imaged acquired with this source (Figure 4-11, top) has the highest resolution in this study and the sharpest retinal features. However, it also has the lowest SNR performance due to the increased bandwidth of the bandpass filter. The expected 1.8 μm OCT axial resolution in the eye was observed in a Gaussian interference fringe obtained from an isolated retinal reflection in the axial scan (Figure 4-11 C).

This study investigating the relationship between OCT axial resolution and the retinal image quality has yielded two interesting findings. Though OCT image quality (in terms of sharpness of features) continue to improve at higher axial resolutions, it appears that the minimum OCT resolution that would continue to yield additional diagnostic information is ~6 μm in air or 4.5 μm in tissue. The fine intraretinal features (GCL, ELM, photoreceptor

segments) that can be visualized at the finest OCT axial resolution can also be recognized at lower axial resolutions of 2.4 μm or 4.5 μm axial resolutions. Therefore, future ultrahigh resolution OCT systems that can achieve 6 μm axial resolution in air would presumably provide similar performance than the current clinical ultrahigh resolution OCT system.

In addition, this study also indicates that chromatic aberrations of the eye do not limit the OCT axial resolution to 3 μm and retinal OCT imaging down to 1.8 μm is still possible. At the broadest source bandwidths of 122 nm and 230 nm, the observed OCT axial resolution in air was 3.2 μm and 2.4 μm, respectively. The observed OCT axial resolution in the retina were 2.4 μm for 122 nm source bandwidth and 1.8 μm for 230 nm source bandwidth. Since these measured axial resolutions in tissue were exactly the same as those calculated from OCT axial resolutions in air, the imperfect optics of the eye does not appear to have adversely affected the axial resolution. It is possible that as source bandwidth continues to increase, there will be a point where the chromatic aberration of the eye limits the absolute axial resolution that can be achieved in the retina. However, this study shows that the optics of the eye still permits retinal OCT imaging down to 1.8 μm axial resolution.

4.4 References

1. Ko TH, Fujimoto JG, Schuman JS, et al. Comparison of Ultrahigh and Standard Resolution Optical Coherence Tomography for Imaging Macular Pathology. Ophthalmology in review.

2. Gass JDM. Stereoscopic Atlas of Macular Diseases: Diagnosis and Treatment. In, 3rd ed. St. Louis, Missouri: CV Mosby, 1987; v. 1.

3. Gloesmann M, Hermann B, Schubert C, et al. Histologic correlation of pig retina radial stratification with ultrahigh-resolution optical coherence tomography. Investigative ophthalmology & visual science 2003;44(4):1696-703.

4. Anger EM, Unterhuber A, Hermann B, et al. Ultrahigh resolution optical coherence tomography of the monkey fovea. Identification of retinal sublayers by correlation with semithin histology sections. Exp Eye Res 2004;78(6):1117-25.

5. Toth CA, Narayan DG, Boppart SA, et al. A comparison of retinal morphology viewed by optical coherence tomography and by light microscopy. Archives of ophthalmology 1997;115(11):1425-8.

6. Hoang QV, Linsenmeier RA, Chung CK, Curcio CA. Photoreceptor inner segments in monkey and human retina: mitochondrial density, optics, and regional variation. Vis Neurosci 2002;19(4):395-407.

7. Swanson EA, Izatt JA, Hee MR, et al. In vivo retinal imaging by optical coherence tomography. Optics Letters 1993;18(21):1864-6.

8. Hee MR, Izatt JA, Swanson EA, et al. Optical coherence tomography of the human retina. Archives of Ophthalmology 1995;113(3):325-32.

9. Drexler W, Morgner U, Ghanta RK, et al. Ultrahigh-resolution ophthalmic optical coherence tomography. Nature Medicine 2001;7(4):502-7.

10. Enoch JM. Visualization of wave-guide modes in retinal receptors. Am J Ophthalmol 1961;51:1107-18.

11. Fankhauser F, Enoch J, Cibis P. Receptor orientation in retinal pathology. A first study. Am J Ophthalmol 1961;52:767-83.

12. Winston R, Enoch JM. Retinal cone receptor as an ideal light collector. J Opt Soc Am 1971;61(8):1120-2.

13. Zeimer R, Asrani S, Zou S, et al. Quantitative detection of glaucomatous damage at the posterior pole by retinal thickness mapping. A pilot study. Ophthalmology 1998;105(2):224-31.

14. Greenfield DS, Bagga H, Knighton RW. Macular thickness changes in glaucomatous optic neuropathy detected using optical coherence tomography. Arch Ophthalmol 2003;121(1):41-6.

CHAPTER 5: IMAGING MACULAR PATHOLOGIES

Standard ophthalmic OCT systems using superluminescent diodes can perform retinal imaging with 10 μm axial resolution. The first ultrahigh resolution OCT of the human eye was reported in 2001.[1] That study was performed with a custom-built Titanium:sapphire femtosecond laser and it demonstrated the ability to perform retinal imaging with 3 μm axial resolution.[1] However, these initial studies were performed on the laboratory-based ultrahigh resolution OCT system that is not suitable for transfer into the ophthalmology clinic.

A clinical ultrahigh resolution OCT system was developed (Chapter 2) and successfully transferred and implemented into the ophthalmology clinic of the New England Eye Center, Tufts University School of Medicine. Ultrahigh resolution OCT imaging studies were performed in coordination with clinical collaborators, Dr. Jay S. Duker of the New England Eye Center and Dr. Joel S. Schuman of the University of Pittsburgh Medical Center (formerly of the New England Eye Center). To date, over 700 patients representing a wide variety of retinal pathologies have been imaged on the clinical ultrahigh resolution OCT system.

5.1 Imaging Protocols

Figure 5-1 shows the clinical ultrahigh resolution OCT system as it was implemented in ophthalmology clinic of the New England Eye Center. The clinical Titanium:sapphire low-threshold laser was covered in a laser box for eye safety and placed in the clinical examination room. The ultrahigh resolution OCT system was placed on a movable cart that can be moved easily into the clinic. To perform ultrahigh resolution OCT imaging, the patient looks into the integrated slit-lamp biomicroscope as in a standard ophthalmic eye exam. The patient fixates his

or her gaze onto an internal fixation target in the slit-lamp while the ultrahigh resolution OCT imaging is performed.

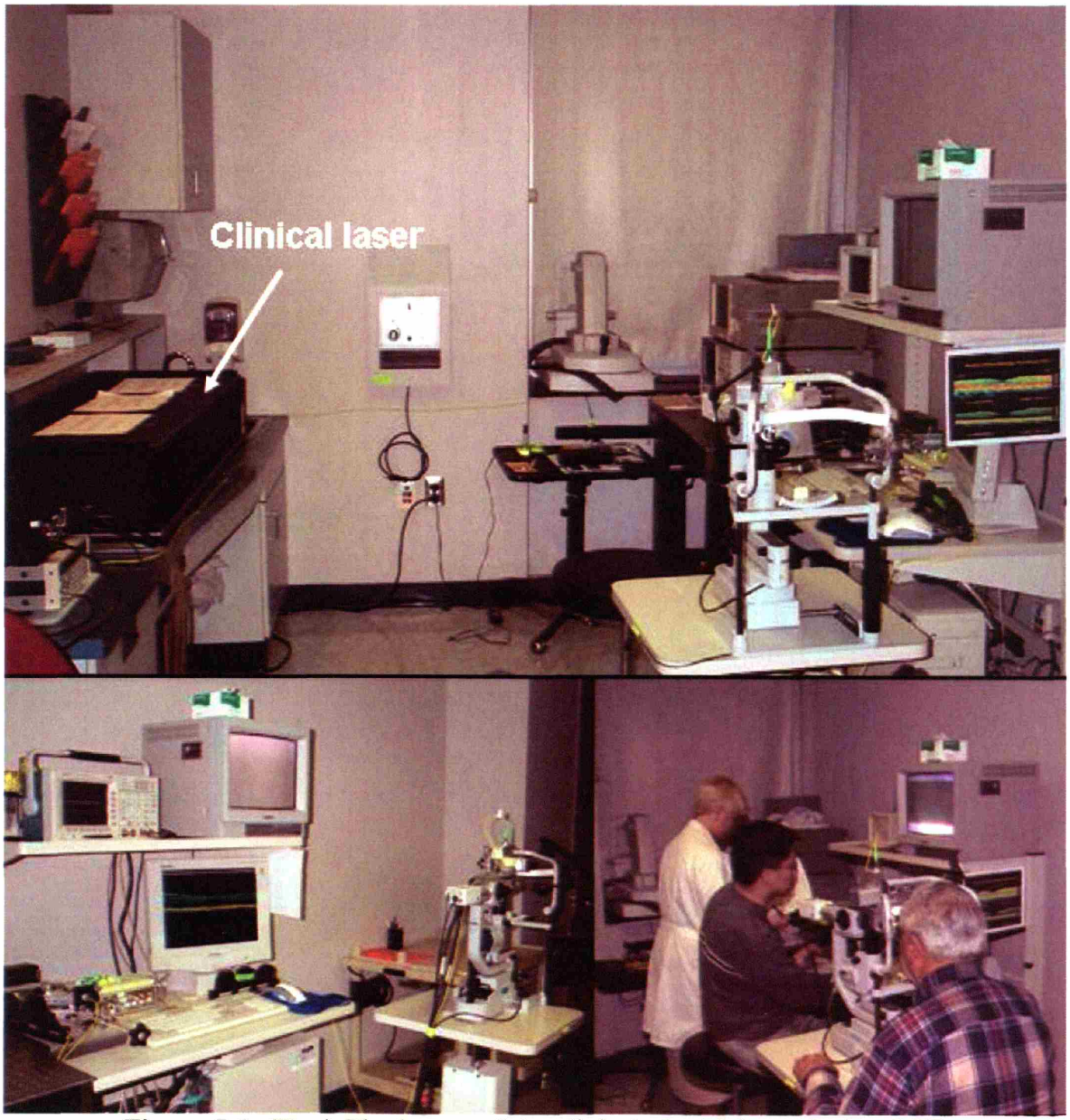

Figure 5-1. (Top) The layout of the clinical ultrahigh resolution OCT system in a clinical examination room of the New England Eye Center. **(Bottom, Left)** The ultrahigh resolution OCT system fits onto a movable cart and is connected to the slit-lamp biomicroscope. **(Bottom, Right)** The patient looks into the slit-lamp as in a standard eye exam and ultrahigh resolution OCT imaging is performed.

During a patient's scheduled visit to the ophthalmology clinic, patients with identified retinal pathologies of interest were recruited by the attending ophthalmologists to participate in the ultrahigh resolution OCT imaging study. The study was approved by the IRB committees of both Tufts-New England Medical Center and MIT and is HIPPA-compliant. Written informed consents were obtained from all subjects who agree to participate in the imaging studies. The consented subjects continues with their normal clinical visit including examinations by the ophthalmologists as well as standard imaging studies and tests associated with their scheduled visit. Standard resolution StratusOCT imaging was performed on all test subjects in order to compare with ultrahigh resolution OCT imaging. If indicated, additional clinical tests and imaging studies such as fundus photography, fluorescein angiography, and electroretinogram were also included. The ultrahigh resolution OCT imaging is performed at the end of the study subject's clinical visit and does not add significantly to the patient's total time in the ophthalmology clinic.

The clinical ultrahigh resolution OCT system is based on a slit-lamp biomicroscope which has an integrated CCD to provide a video image of the fundus. This provides a real time view of the fundus during OCT imaging. The patient's eye position was maintained using an internal fixation target, as in the commercial StratusOCT instrument. The patient looks into the slit-lamp biomicroscope and fixes his or her gaze on the internal fixation target while the ultrahigh resolution OCT scan is being performed. A computer was used to control the scanning pattern of the OCT beam on the retina, acquire data, and generate an OCT image on the display in real time. Ultrahigh resolution OCT imaging was performed using up to 750 μW of incident optical power in the OCT scanning beam, the same incident power as used in the commercial StratusOCT instrument.

The imaging protocol of the ultrahigh resolution OCT follows the standard StratusOCT imaging protocol in order to permit a direct comparison of the imaging performance of the two instruments. For OCT scans in the macula, the standard StratusOCT imaging protocol consists of six linear OCT scans of 6 mm length centered on the fovea. Each scan was acquired oriented at angles separated by 30-degree intervals, resulting in 3 mm rays at each clock hour emanating from the fovea. For OCT scans in the optic nerve head, the standard StratusOCT imaging protocol consists of six linear OCT scans of 4 mm length, each separated by 30-degree angles, centered on the optic disc. For circumpapillary OCT scans, the standard StratusOCT imaging

protocol consist of three circular OCT scans of 3.4 mm diameter. The circular OCT scans are centered on the optic disc by the operator. In the ultrahigh resolution OCT system, the macular scans are performed with an internal fixation target (a black crosshair) that is presented to the subjects in the slit-lamp viewing path. In this manner, the position of the subject's fovea is fixated on the crosshair and the linear OCT scans can be centered onto this position. For optic nerve head and circumpapillary OCT scans, the ultrahigh resolution OCT system presents a blinking fixation dot for the subject to fixate. Using the video image of the fundus for guidance, the blinking fixation point and/or the OCT scan beams can be moved until the optic disc is centered onto the OCT scans. The StratusOCT images consisted of 1024 axial pixels and 512 transverse pixels (total = 524,288 pixels). The ultrahigh resolution OCT images consisted of 3000 axial and 600 transverse pixels (total= 1,800,000 pixels).

After OCT scanning was completed, the ultrahigh resolution OCT images were corrected for axial motion using standard re-registration algorithms. These algorithms have been used in all of the previous prototype and commercial OCT systems.[2] The StratusOCT images are usually not corrected for axial motion because the commercial software exports only uncorrected raw images. Since the StratusOCT can acquire an image in 1.3 seconds as compared to ~4 seconds in the clinical ultrahigh resolution OCT system, the axial motions in the StratusOCT images are usually not significant; however, additional software have also been developed to correct the raw StratusOCT images in cases where axial motion is substantial. Ultrahigh resolution OCT images were compared to standard resolution StratusOCT images as well as clinical photos and patient history to assess the ability for ultrahigh resolution OCT to improve the visualization of intraretinal features associated with retinal disease pathology.

The diagnosis of macular pathology was performed using standard clinical methods including fundus examination, fundus photography and/or fluorescein angiography. Fundus photography and fluorescein angiography allow comparison of fundus features to cross-sectional features visualized in the OCT images. A wide variety of macular pathologies were investigated using ultrahigh resolution OCT. The macular pathologies imaged include macular holes, central serous chorioretinopathy, macular edema, age-related macular degeneration (dry and wet), retinal pigment epithelium detachment, epiretinal membrane, vitreomacular traction, and retinitis pigmentosa.

5.2 Macular Holes

The initial classification, staging, and pathogenesis of idiopathic macular holes was based largely on clinical examination and fluorescein angiography.[3, 4] More recently, optical coherence tomography (OCT) has been employed.[5] Standard resolution OCT imaging has been used to improve the understanding macular hole pathogenesis and has already yielded an improved staging of macular holes.[5-9]

Lamellar Hole

Figure 5-2 shows the OCT images acquired from a 58 year old woman with 20/30 vision in her right eye that was diagnosed with a lamellar hole upon clinical examination.

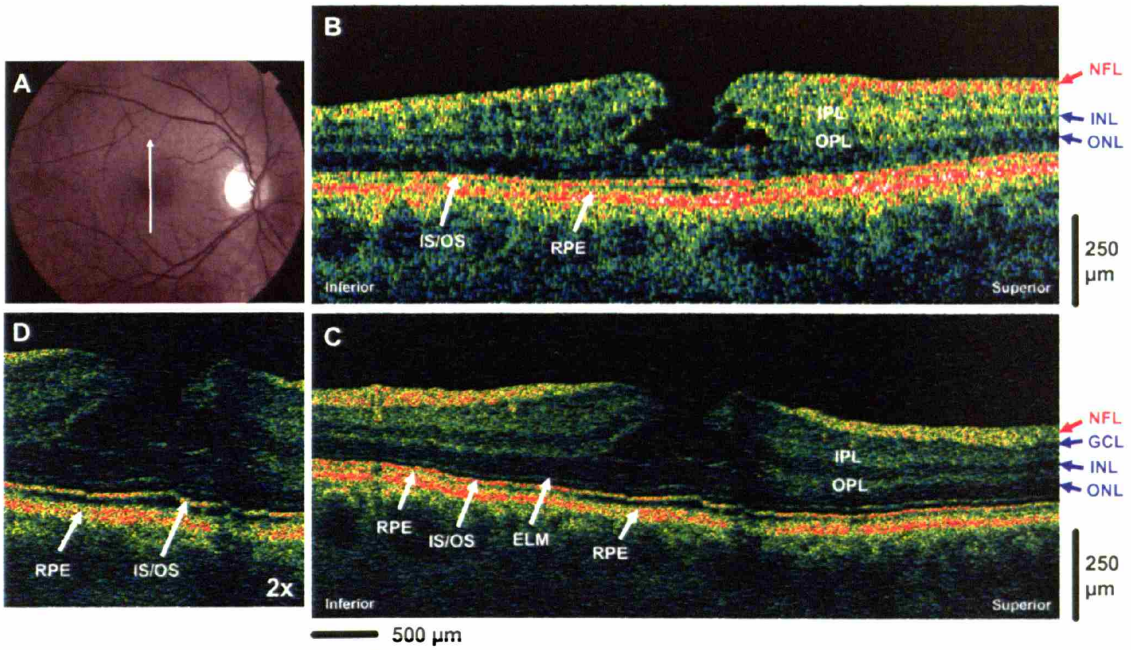

Figure 5-2. (A) Fundus photo depicting lamellar hole and the direction of OCT scans. **(B)** StratusOCT and **(C)** ultrahigh resolution OCT image of lamellar hole. **(D)** Two times magnification of the ultrahigh resolution OCT image in the region of the lamellar hole.[10]

Comparing standard resolution StratusOCT image to the ultrahigh resolution OCT image of the lamellar hole, it is evident that the lamellar hole in both images does not involve the structures of the outer retina (ONL, ELM, photoreceptor IS/OS) which remain intact and juxtaposed with the

RPE. This finding helps explain the relatively intact visual acuity of lamellar hole cases. Both StratusOCT and ultrahigh resolution OCT images also show a separation between the outer nuclear layer (ONL) and the outer plexiform layer (OPL) in the region of the lamellar hole. In the StratusOCT image, most of the major intraretinal layers such as the NFL, IPL, INL, OPL, ONL, IS/OS, and RPE can be visualized, but the low-backscattering ganglion cell layer (GCL) and the thin backreflecting feature corresponding to the ELM are not well visualized in the standard resolution image. The ultrahigh resolution OCT image more clearly visualizes small features such as the ELM that are associated with photoreceptor segments in the outer retina. The junction (IS/OS) that separates the inner and outer segments of the photoreceptor layer appears to be highly backreflecting and is visualized in both OCT images. This highly visible IS/OS junction may be used to detect the integrity of the photoreceptor outer segments even in standard resolution OCT images.

Stage 1b Macular Hole

Figure 5-3 shows the OCT images acquired from a 64 year old woman with 20/50 vision in her right eye that was diagnosed with a stage 1b macular hole upon clinical examination. Both OCT images show the posterior hyaloid attachment to the fovea. Both images also show a small portion of the sensory retina that has detached from the RPE in the foveola region. Small cystic changes are also visible in the ganglion cell layer (GCL) and inner nuclear layer (INL). The ultrahigh resolution OCT image provides enhanced visualization of fine intraretinal features of the ELM and the Henle's fibers of the outer plexiform layer (Figure 5-3D, yellow asterisk). The ultrahigh resolution OCT image provides an enhanced visualization of the very fine structures which may be still intact Müller cells that span the separation between the outer nuclear layer and the outer plexiform layer. The angled orientation of these structures suggests traction on the photoreceptors. In the region of central foveal elevation, both standard and ultrahigh resolution OCT images show a reduced backreflection from the boundary between the photoreceptor inner and outer segments (IS/OS) in the region of the photoreceptor detachment. However, the increased resolution of the ultrahigh resolution OCT image indicates that the photoreceptor inner and outer segments are still intact and attached to the ONL portion of the sensory retina even in the region of the photoreceptor detachment (Figure 5-3D). Following the highly reflecting

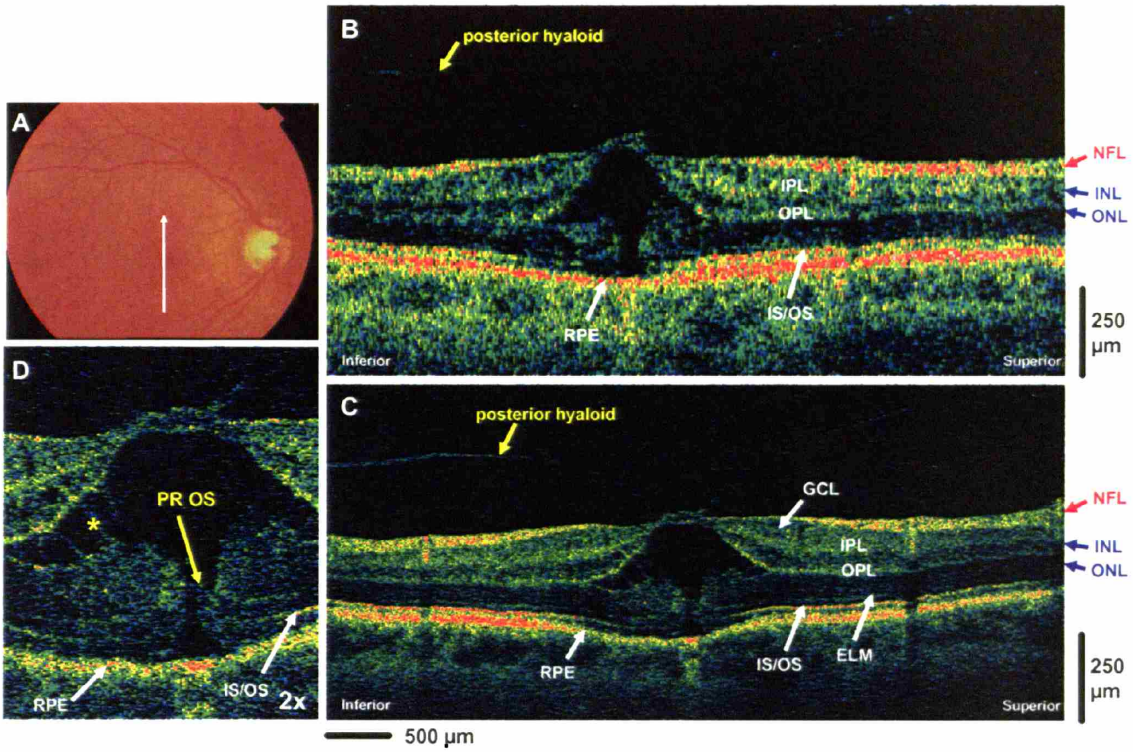

Figure 5-3. (A) Fundus photo depicting stage 1b macular hole and the direction of OCT scans. **(B)** StratusOCT and **(C)** ultrahigh resolution OCT image of stage 1b macular hole. **(D)** Two times magnification of the ultrahigh resolution OCT image in the region of the stage 1b macular hole.[10]

feature of the IS/OS junction from the parafoveal region into the region of the photoreceptor detachment, it is seen that the photoreceptor outer segment (Figure 5-3D, PR OS) is still attached to the IS/OS junction. In response to the presence of the macular hole, the photoreceptor segments in this region appear to be detached from the RPE and lifted away from its anatomical position. There is a diminishment of the highly reflecting IS/OS junction in this region of detachment and this may be attributed to the altered orientation of photoreceptors and the IS/OS junction caused by the lifting away of photoreceptors from the RPE. These finer features involving the photoreceptor outer segment and the IS/OS junction are difficult to differentiate in the standard resolution StratusOCT image. The preservation of the photoreceptor outer segment demonstrated by the ultrahigh resolution OCT image can possibly explain the reason why macular hole surgery often has a successful outcome. Surgery can re-appose the intact photoreceptors back to their normal anatomical position against the RPE and facilitate the

recovery of visual function. Due to its lower resolution and difficulty in identifying the ELM and photoreceptor segments, the StratusOCT image may incorrectly suggest that there is a complete loss of outer retinal tissue in the region of the macular hole, when in fact the outer retinal morphology (EML and photoreceptor segments) is preserved, but only lifted away from the RPE in the foveola.

Stage 2 Eccentric Macular Hole

Figure 5-4 shows the OCT images acquired from a 71 year old woman with 20/200 vision in her right eye that was diagnosed with a stage 2 macular hole upon clinical examination.

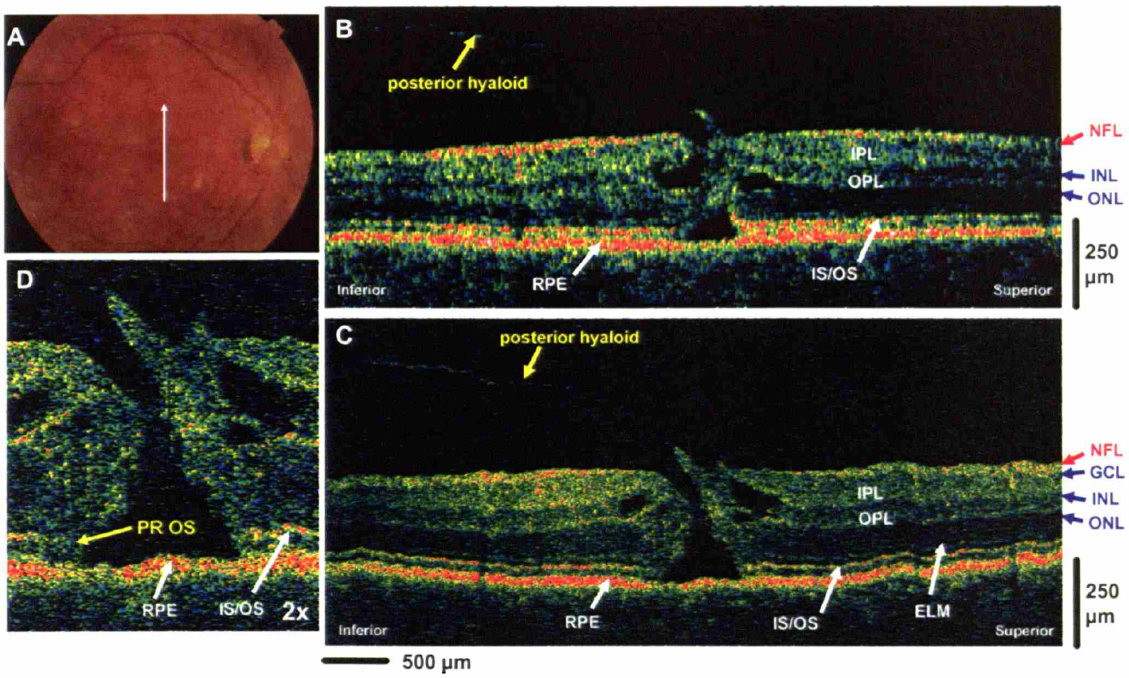

Figure 5-4. (A) Fundus photo depicting eccentric stage 2 macular hole and the direction of OCT scans. **(B)** StratusOCT and **(C)** ultrahigh resolution OCT image of eccentric stage 2 macular hole. **(D)** Two times magnification of the ultrahigh resolution OCT image in the region of the eccentric stage 2 macular hole.[10]

Both standard resolution StratusOCT and ultrahigh resolution OCT images show the thin reflective posterior hyaloid that is connected to the "lid" of the stage 2 macular hole. The OCT images correspond to an "eccentric" macular hole where the opening of the hole is not centered

on the fovea. Cystic spaces are present in the inner nuclear layers of both OCT images. In the region of the macular hole, the ultrahigh resolution OCT image shows the preservation of the photoreceptor outer segment (Figure 5-4D, PR OS) that is lifted away from the RPE. The posterior hyaloid seen in both OCT images suggest that the pathogenesis of this macular hole may be due to oblique, as opposed to tangential, traction of the hyaloid. The lower resolution of the standard resolution image does not clearly indicate the preservation of the PR OS in the foveola region.

Figure 5-5 shows the OCT images acquired from the same patient at the same location following macular hole surgery.

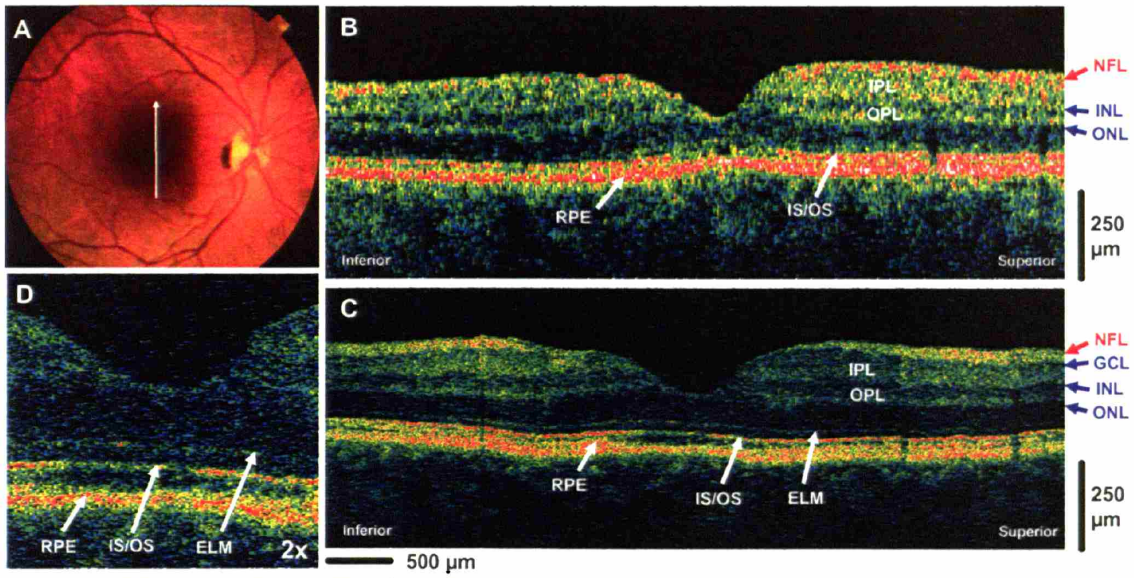

Figure 5-5. (A) Fundus photo depicting repair of the eccentric stage 2 macular hole after surgery. **(B)** StratusOCT and **(C)** ultrahigh resolution OCT image of the repair of eccentric stage 2 macular hole after macular hole surgery. **(D)** Two times magnification of the ultrahigh resolution OCT image in the region of the eccentric stage 2 macular hole repair.[10]

After macular hole surgery, the patient's vision improved to 20/40 and the macular hole appeared closed on funduscopic examination. Both StratusOCT and ultrahigh resolution OCT scans show the restoration of the normal foveal depression and the resolution of the cystic intraretinal spaces. The photoreceptor inner and outer segments appear to be intact and connected to the RPE in the region where the stage 2 macular hole was prior to surgery. The ultrahigh

resolution OCT image shows a re-appearance of the thin backreflecting ELM layer and the highly backreflecting boundary between the photoreceptor IS/OS in the foveola region. Even though the StratusOCT image cannot distinguish the thin ELM layer in the outer retina, the StratusOCT image can be used to demonstrate the return of the highly backreflecting boundary between the photoreceptor IS/OS after the macular hole surgery. The presence of this feature suggests that the integrity of the photoreceptor outer segments has been largely preserved and there is minimal photoreceptor impairment. However, both standard resolution and ultrahigh resolution OCT images also show that this usually highly backreflecting IS/OS junction appears to be less backreflecting after the macular hole surgery than in the normal adult eye (Chapter 4). There also appears to be small discontinuities of the junction between the photoreceptor IS/OS in the region of the repaired hole (Figure 5-5D), suggesting that small residual photoreceptor impairments may still be present. This may account for the lack of full visual acuity recovery post operatively.

Stage 3 Macular Hole

Figure 5-6 shows the OCT images acquired from a 64 year old woman with 20/50 vision in her left eye which had a chronic stage 3 macular hole. Both StratusOCT and ultrahigh resolution OCT images clearly visualized a full-thickness macular hole. Cystic areas at the border of the macular hole appear to be localized in the outer nuclear and inner nuclear layers of the parafoveal region. The ultrahigh resolution OCT enhances visualization of the smaller cystic structures in the ONL. External to the macular hole, the neurosensory retinal layers appear to be normal in both the StratusOCT and ultrahigh resolution OCT images. The improved resolution in the ultrahigh resolution OCT image enables visualization and identification of the ELM that is not clearly seen in the StratusOCT image. In the region of the macular hole, the ultrahigh resolution OCT image again shows that the integrity of the photoreceptors is preserved, but only detached from the RPE (Figure 5-6D). By following the highly visible backreflecting feature of the IS/OS junction from the parafoveal area to the region of the macular hole, the ultrahigh resolution OCT image shows the photoreceptor outer segments (PR OS) to be lifted away from the RPE but are still intact and connected to the rest of the sensory retina. The reduced backreflection from the junction between the photoreceptor inner and outer segments may be the

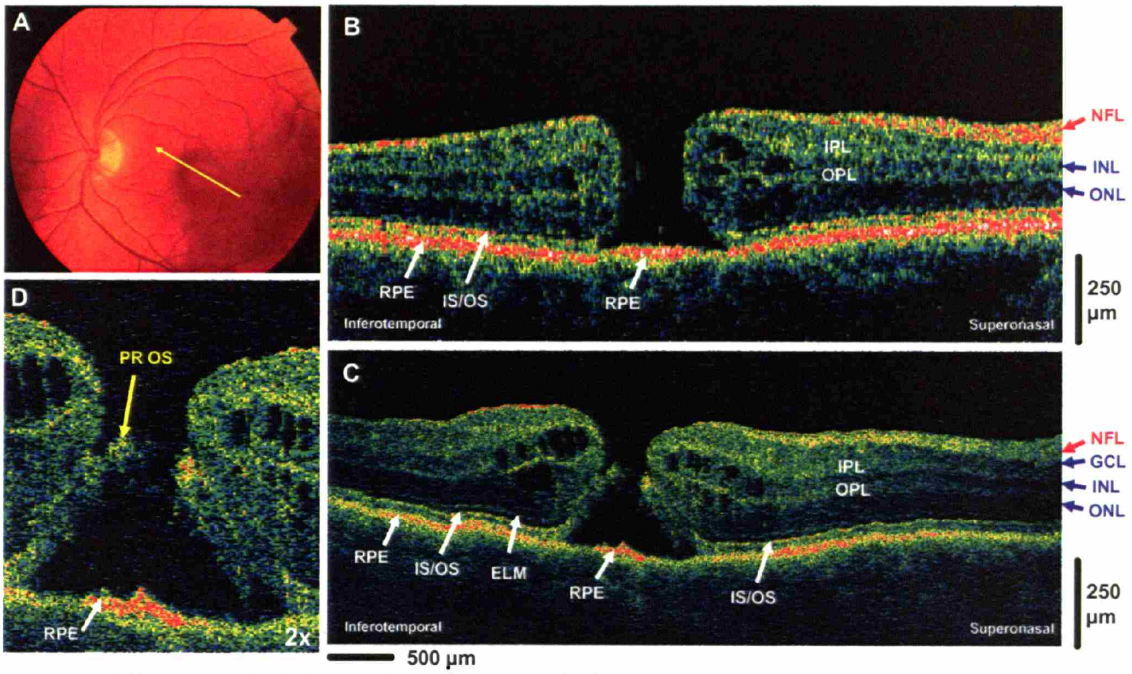

Figure 5-6. (A) Fundus photo depicting stage 3 macular hole and the direction of OCT scans. **(B)** StratusOCT and **(C)** ultrahigh resolution OCT image of stage 3 macular hole. **(D)** Two times magnification of the ultrahigh resolution OCT image in the region of the stage 3 macular hole.[10]

results of misalignment of the photoreceptors from their normal anatomical position.[11-13] The StratusOCT image does not have the resolution to resolve the fine features of the photoreceptor outer segments and may incorrectly suggest that there is a complete loss of photoreceptor outer segments in the region of the macular hole.

Stage 4 Macular Hole

Figure 5-7 shows the OCT images acquired from a 64 year old woman with 20/80 vision in her right eye that was diagnosed with a stage 4 macular hole upon clinical examination. Both StratusOCT and ultrahigh resolution OCT images demonstrate a full-thickness macular hole as well as cystic spaces in the outer nuclear and outer plexiform layers. A pseudo-operculum can clearly be seen above the region of the macular hole. At the boundary with the outer plexiform layer (OPL), there are cystic changes in the outer nuclear layer (ONL) as well as in the inner

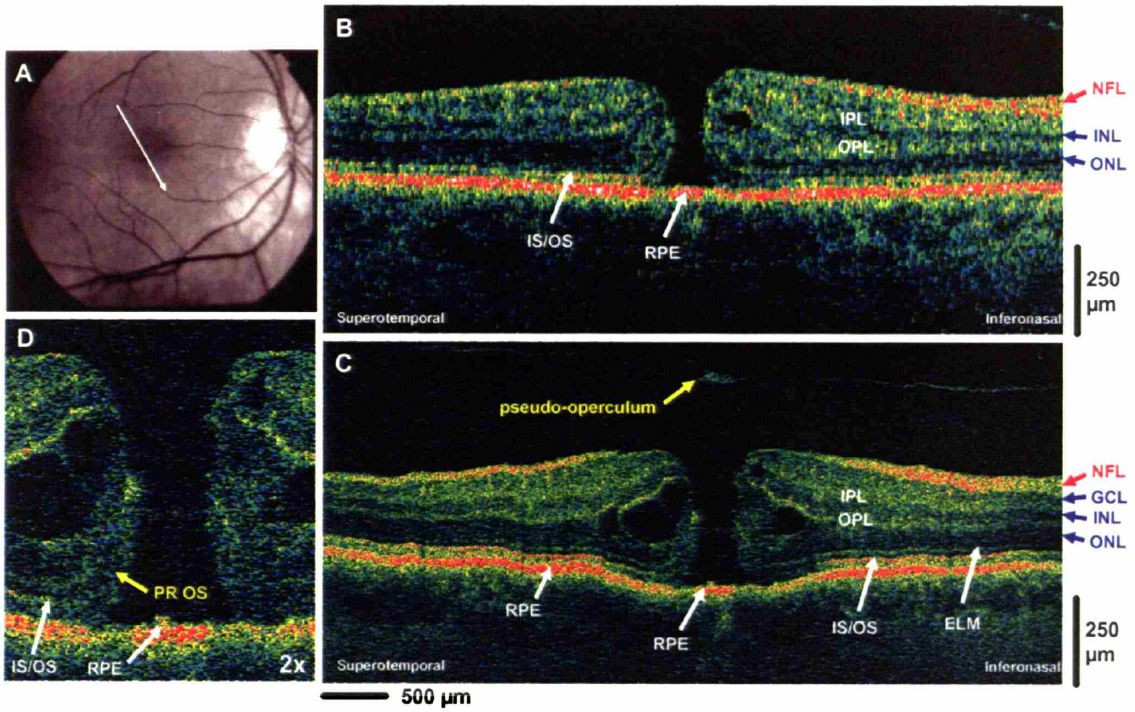

Figure 5-7. (A) Red-free fundus photo depicting stage 4 macular hole and the direction of OCT scans. **(B)** StratusOCT and **(C)** ultrahigh resolution OCT image of stage 4 macular hole. **(D)** Two times magnification of the ultrahigh resolution OCT image in the region of the stage 4 macular hole.[10]

nuclear layer (INL). In the foveal region, the sensory retina has detached from the RPE and the RPE is clearly visualized in the foveola. There is a slight shadowing of the RPE signal in the parafoveal region where there is edema of the sensory retina. The ultrahigh resolution OCT image indicates the architectural morphology of the ELM and photoreceptor IS/OS junction are preserved in the region of the macular hole (Figure 5-7D). The photoreceptor inner and outer segments are lifted away from their anatomical position against the RPE, but remain intact. By visualizing that the photoreceptor layer morphology is intact in the region of the macular hole, ultrahigh resolution OCT confirms that the structure observed above the macular hole is a pseudo-operculum and not a true operculum. Due to its lower resolution, it is difficult for StratusOCT images to differentiate the photoreceptor segment morphology in this detail.

Figure 5-8 shows the OCT images acquired from the same patient after macular hole surgery. After macular hole surgery, the patient's vision improved to 20/40 and the macular hole

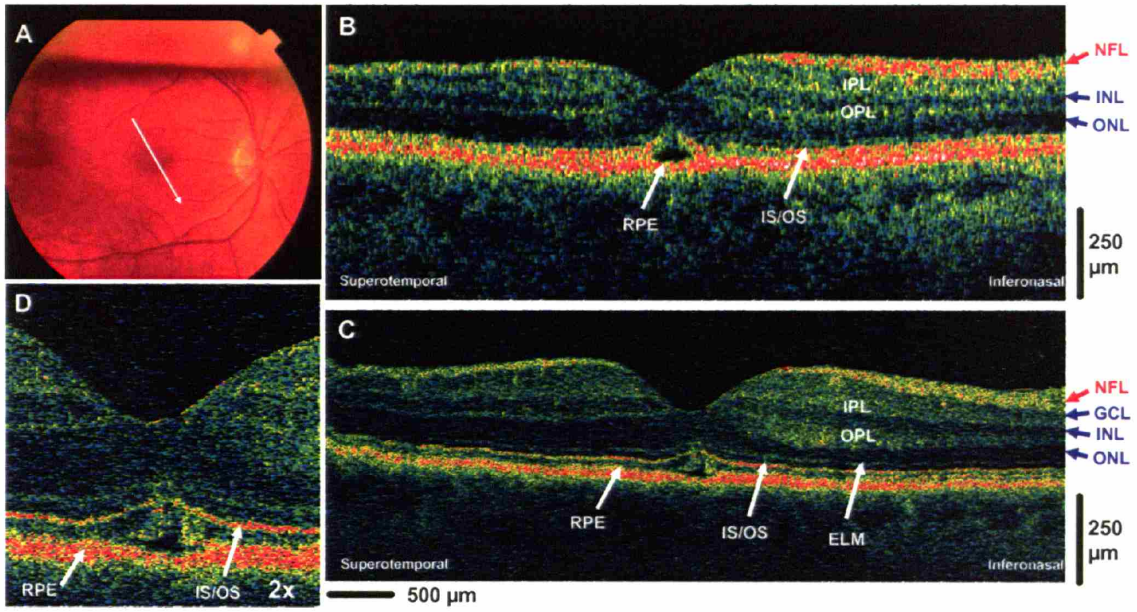

Figure 5-8. (A) Fundus photo depicting repair of the stage 4 macular hole after surgery. **(B)** StratusOCT and **(C)** ultrahigh resolution OCT image of the repair of stage 4 macular hole after macular hole surgery. **(D)** Two times magnification of the ultrahigh resolution OCT image in the region of the stage 4 macular hole repair.[10]

appears closed. Both StratusOCT and ultrahigh resolution OCT images demonstrate the return of normal foveal depression and the disappearance of cystic intraretinal spaces. Both images also show a small elevation of the outer retina away from the RPE in the central fovea which may account for some of the residual post-operative visual impairment. Both StratusOCT and ultrahigh resolution OCT images demonstrate the return of the highly backreflecting IS/OS photoreceptor segment junction in the parafoveal region, but the ultrahigh resolution OCT image more clearly shows the re-appearance of the thin backreflecting ELM layer. The ELM layer appears to be continuous after the surgery, but there is a residual elevation in the photoreceptor outer segments in the foveola. The abnormal elevation of the central photoreceptors is seen in both StratusOCT and ultrahigh resolution OCT images, but only the ultrahigh resolution OCT image has the resolution to distinguish the photoreceptor outer segments that are still present in this region (Figure 5-8D). This suggests that the foveolar elevation is caused by the continual shedding of the outer segment debris that can not be completely reabsorbed by the RPE due to the lack of correct apposition of the outer segments with the RPE. The lower resolution of

StratusOCT does not indicate the presence of outer segment tissue in the foveola elevation, which can incorrectly suggest subretinal fluid under the foveola elevation.

Understanding Macular Hole Images

The results from ultrahigh resolution OCT imaging of various stages of macular hole lends support the new interpretation of the OCT signals of the outer retina. The junction between the photoreceptor inner and outer segments (IS/OS) was previously incorrectly interpreted as the melanin-containing retinal pigment epithelium.[1, 14] With ultrahigh resolution OCT and the understanding of macular hole pathologic morphology, the first thin high backscattering feature of the outer retina is identified as the inner/outer segment junction anterior to the RPE signal which is represented by the second high backscattering feature in the outer retina. As expected in full-thickness macular holes, there is no involvement of the backscattering features representing the RPE layer in the OCT images, while the features representing the photoreceptor layers were affected.

The ability of ultrahigh resolution OCT to visualize fine features such as the ELM and the details of photoreceptor outer segment morphology indicates that the morphology of the photoreceptors is often preserved in the region of the macular hole where the sensory retina is detached from the RPE. This contrasts with standard resolution OCT images which can be incorrectly interpreted to suggest that sensory retinal tissue and photoreceptors are lost in the focal area of the macular hole. This finding was also not reported in previous studies of macular hole with ophthalmoscopic examination or standard resolution OCT.[4-6, 8, 9] From the viewpoint of imaging with standard resolution OCT, special attention should be paid to visualization of the highly backreflecting junction between the photoreceptor inner and outer segments (IS/OS) since this can be used as an indicator of photoreceptor integrity or impairment. Integrity of the photoreceptor outer segment would be a necessary, though not sufficient condition, for restoration of visual function. The ability to visualize and track photoreceptor morphology associated with macular hole formation may play a role in further understanding the process of macular hole formation. Ultrahigh resolution OCT may also be useful in predicting and assessing the potential outcome of macular hole surgery based on the morphologic appearance of the photoreceptor layers in the region of the macular hole.

5.3 Central Serous Chorioretinopathy

Figure 5-9 shows the OCT images acquired from a 50 year old man with the diagnosis of acute central serous chorioretinopathy (CSCR) in his left eye.

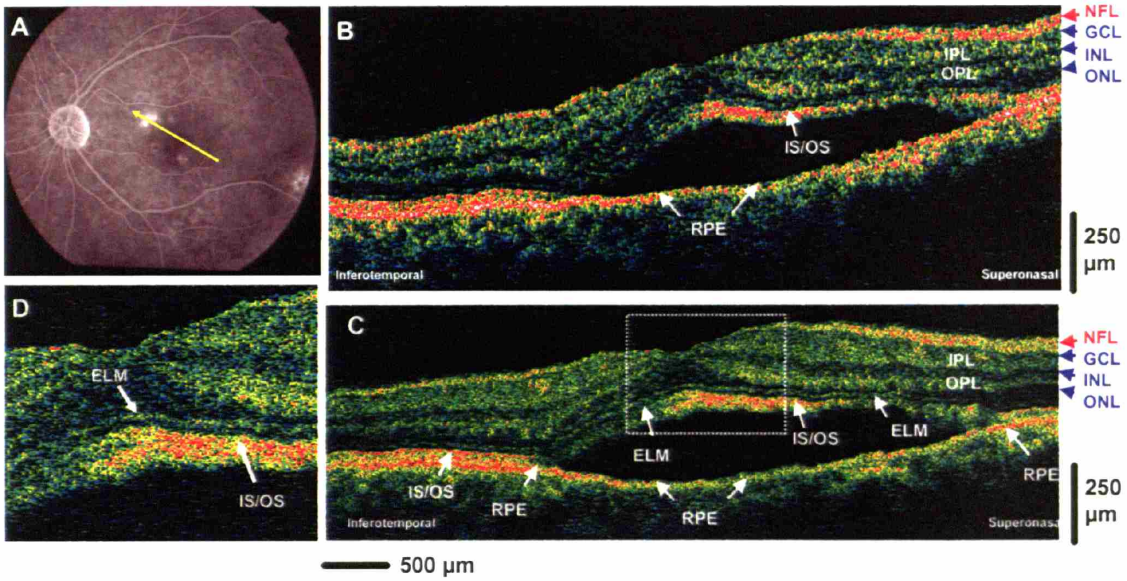

Figure 5-9. (A) Late-phase fluorescein angiogram depicting the lesion of central serous chorioretinopathy and the direction of OCT scans. **(B)** StratusOCT and **(C)** ultrahigh resolution OCT image of central serous chorioretinopathy. **(D)** A 2x enlargement of the ultrahigh resolution OCT image demonstrates the preservation of the photoreceptor inner and outer segment in the sensory retina that has separated away from the RPE.[15]

The late-phase fluorescein angiography (FA) fundus photo depicts several hyperfluorescent spots which suggests compromise of Bruch's membrane and leakage into the subretinal space. Both StratusOCT and ultrahigh resolution OCT images taken across the predominant hyperfluorescent area clearly show the serous detachment of the sensory retina. However, all the intraretinal layers in the sensory retina appear to be intact on ultrahigh resolution OCT. In addition, the ultrahigh resolution OCT image indicates the intact appearance of the ELM and IS/OS photoreceptor layers. The highly backreflecting line in the outer boundary of the detached retina appears to be the IS/OS junction. In the elevated retina, there appears to be also be a high backscattering region immediately underneath the normally sharp boundary of the IS/OS junction signal. This region of high backscattering may reflect the ends of the outer segment that

continues to shed into the subretinal space following the retinal detachment. In this central serous chorioretinopathy case, the RPE does not appear to be detached in both the StratusOCT and ultrahigh resolution OCT images.

Follow-up Imaging after One Month

Figure 5-10 shows the OCT images acquired from the same fundus locatoin one month following initial presentation.

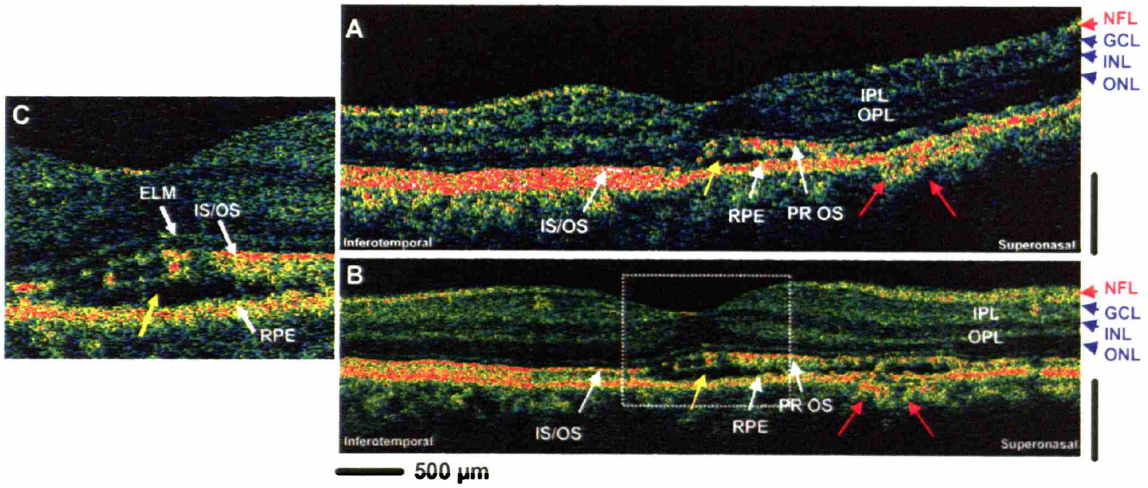

Figure 5-10. (A) StratusOCT and **(B)** ultrahigh resolution OCT image of the central serous chorioretinopathy after 1 month. **(C)** A 2x enlargement of the ultrahigh resolution OCT image.[15]

Both StratusOCT and ultrahigh resolution OCT images of the same fundus location show partial resolution of the central serous chorioretinopathy after 1 month. Both images demonstrate the decreased serous fluid accumulation under the sensory retina (yellow arrows). A disruption of the RPE layer in the superior-nasal region of the macula (red arrows) is seen much more clearly in the ultrahigh resolution OCT image. The disruption of the RPE is in an area that corresponds to the region of dominant hyperfluorescence in the fluorescence angiogram (Figure 5-9A).

Follow-up Imaging after Two Months

Figure 5-11 shows the OCT images acquired from the same fundus locatoin two months following initial presentation.

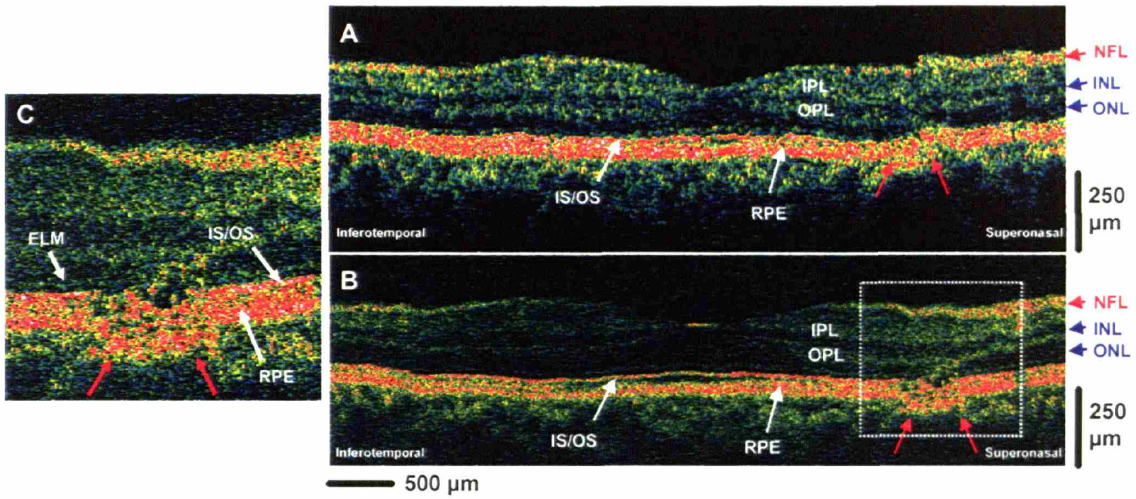

Figure 5-11. (A) StratusOCT and **(B)** ultrahigh resolution OCT image of the central serous chorioretinopathy after 2 months. **(C)** A 2x enlargement of the ultrahigh resolution OCT image.[15]

Both StratusOCT and ultrahigh resolution OCT images taken at the same fundus location after 2 months reveal complete disappearance of the subretinal serous fluid as well as recovery of the normal retinal appearance in the intraretinal layers. This is consistent with the recovery associated with the resolution of central serous chorioretinopathy. The ultrahigh resolution OCT image indicates more clearly a residual lesion in the RPE layers near the superior-nasal region of the macula (red arrows). An associated disruption of the outer nuclear layer and photoreceptor inner and outer segments can also be visualized in this area in the ultrahigh resolution OCT image; these layers appear to be drawn towards the RPE abnormality since the outer nuclear layer appears to be thinner in the region of the RPE disruption. The defect in the RPE, which corresponds to the region of dominant hyperfluorescence in the fluorescence angiogram, is the probable cause for serous leakage of fluid into the intraretinal space, and the ultrahigh resolution OCT image indicates that a lesion is still present even after resolution of the acute central serous chorioretinopathy.

Understanding Central Serous Chorioretinopathy Images

In this central serous chorioretinopathy case, the RPE layer is not involved in the serous elevation of the sensory retina. The RPE can be seen in the OCT images as the highly

backscattering layer at the bottom of the serous fluid accumulation. In contrast, the highly backscattering interface between the photoreceptor inner and outer segments (IS/OS) can be visualized inside the elevated sensory retina in the affected region as well as in its normal anatomical position in the unaffected adjacent macular region in which there is no sensory retina detachment. This finding lends further support to the interpretation that the first highly backscattering layer in the outer retina is the interface of the photoreceptor inner and outer segments and the second highly backscattering layer is the RPE.

The intensity of the normally highly backreflecting junction between the photoreceptor inner and outer segments (IS/OS) also appears to be dependent on the orientation of the membranous discs in the outer segment.[10] This finding is consistent with previous studies which demonstrated that photoreceptors exhibit directional sensitive waveguiding properties.[11, 16, 17] In their normal anatomical position apposed to the RPE, the membranous stacks lie in an orientation perpendicular to the direction of the incoming OCT beam and a highly backscattering signal is present at this junction. With the serous elevation of the sensory retina (Figure 5-9), the membranous discs in the inferotemporal region of the parafovea no longer lie perpendicular to the direction of the incoming OCT beam and the IS/OS junction appears low backscattering. In the fovea and the superonasal parafovea region of the retina, the outer segment of the elevated sensory retina appears to lie perpendicular to the direction of the incoming OCT beam and the highly backreflecting signal from the IS/OS junction is seen near the fovea and the presence of the photoreceptor outer segment (PR OS) in the elevated retina can be detected. However, in the superonasal parafovea, the signal from the IS/OS junction appears to be weakly backscattering even though the orientation of the outer segments is perpendicular to the incoming OCT beam. The lack of the IS/OS junction signal in this region of the elevated sensory retina may be caused by the disruption of the photoreceptor segments in this area that corresponds to the predominant hyperfluorescence in the fluorescein angiogram (Figure 5-9A).

The pathological disruption of the RPE and photoreceptor cells in this region is clearly indicated by ultrahigh resolution OCT as the central serous chorioretinopathy begins to resolve. In the OCT images of the patient taken at 1 month following initial presentation (Figure 5-10), the IS/OS junction of the superonasal parafovea appears to be highly backreflecting possibly because the orientation of the outer segment is once again perpendicular to the direction of the incoming OCT beam. The small serous accumulation of fluid (yellow arrow) still causes a small

portion of the IS/OS junction to be misoriented and appear weakly backscattering. In the superonasal parafovea, the IS/OS junction can be seen to be disrupted in both OCT images and the ultrahigh resolution OCT shows that the RPE is also disrupted (red arrows) in this region. In the OCT images of the patient taken at 2 months following the initial visit (Figure 5-11), there is a complete return of the highly backreflecting IS/OS junction throughout the macular scans as the orientation of the outer segment returns to the normal anatomical position that is perpendicular to the direction of the incoming OCT beam. The ultrahigh resolution OCT imaging also reveals a localized disruption of the RPE layer in the superonasal parafovea which is the probable cause of the accumulation of serous fluid that led to detachment of the sensory retina. The disruption in the RPE layer appears to damage the adjacent photoreceptor inner and outer segments, leading to a functional deficit in that region. Ultrahigh resolution OCT suggest a downward dragging of retinal elements to the area of the RPE disruption while the architectural morphology of the elevated sensory retina in central serous chorioretinopathy remains intact and appears largely normal. This is consistent with the fact that patients usually have a favorable outcome with recovery of visual acuity upon resolution of the condition.

5.4 Macular Edema

Figure 5-12 shows the OCT images acquired from a 59 year old woman with 20/50 vision in her left eye that was diagnosed with cystoid macular edema and disc swelling upon clinical examination. The late-phase fluorescein angiogram (FA) depicts dye leakage in the characteristic petaloid pattern in the macular region. Both OCT images acquired in the macula clearly show the increase in retinal thickness due to the macular edema. Both images show that the cystoid edema appears in the foveacentralis region, with the large, 100-200 μm size, cystoid structures localized mainly in the inner nuclear layer. The linear spanning structures in this region probably represent Müller cells. The ultrahigh resolution OCT image can better differentiate finer retinal architectural morphology such as small cystoid structures. Ultrahigh resolution OCT shows smaller, ~20-40 μm size, cystoid structures, with sharply differentiated boundaries which appear to be present in the ganglion cell layer (yellow arrow). These smaller lesions are difficult to visualize with StratusOCT. The outer nuclear layer appears to be thicker than normal in these images and there is a small detachment of the photoreceptors from the RPE in center of the fovea (red arrow). There is edema of the photoreceptor outer segment layers and

possibly also photoreceptor inner segment layers with a corresponding change in thickness and increase in optical scattering (hyperscattering). The ELM is difficult to differentiate even in the ultrahigh resolution OCT. In the parafoveal region, the architectural morphology of the NFL, INL, IPL, ONL, OPL, and RPE appears to be normal.

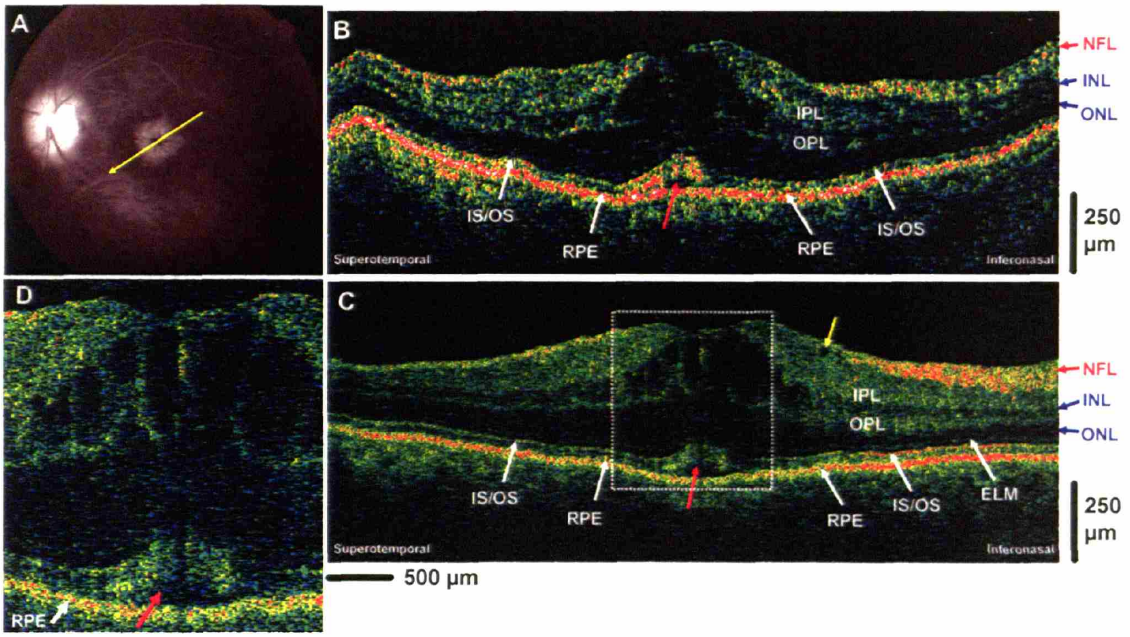

Figure 5-12. (A) Late-phase fluorescein angiogram depicting cystoid macular edema and the direction of OCT scans. **(B)** StratusOCT and **(C)** ultrahigh resolution OCT image of cystoid macular edema. **(D)** A 2x enlargement of the ultrahigh resolution OCT image.[15]

5.5 Dry Age-related Macular Degeneration

Figure 5-13 shows the OCT images acquired from a 72 year old woman with 20/25 vision in her left eye that was diagnosed with dry age-related macular degeneration (AMD). The early-phase fluorescein angiogram of the left eye depicts drusen and dye leakage associated with deterioration of the RPE and choriocapillaris. Both OCT images show disruption of the RPE layer which appears as an irregular and disrupted line in the ultrahigh resolution OCT image, in sharp contrast to the characteristic smooth and straight RPE appearance of the normal eye. The irregularity in the RPE is from AMD-related pathology and not due to eye motion artifacts. This can be seen by comparing the contour of the RPE with the contour of the vireo-retinal interface. These RPE irregularities can be visualized with slightly better clarity in the ultrahigh resolution

OCT image due to its higher resolution. The ELM can only be visualized in the ultrahigh resolution OCT image and appears intact. There are multiple, small irregularities in the photoreceptor inner and outer segments (IS/OS) manifest by what appears to be small bucklings (red arrows) of the highly optically scattering structure, which is interpreted as the RPE, in the region where the outer segments would normally be present.

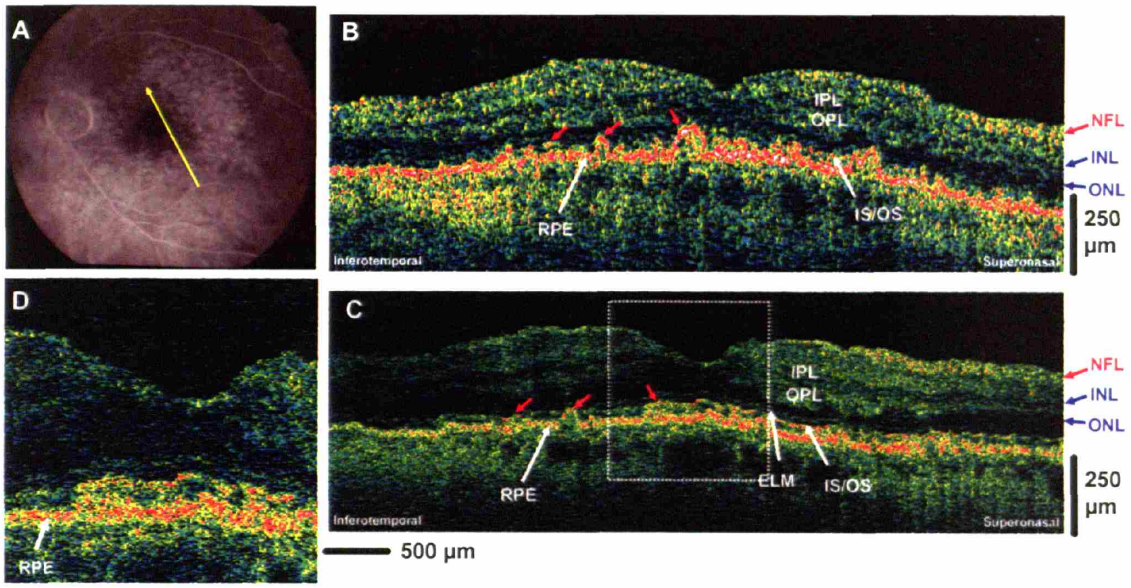

Figure 5-13. (A) Early-phase fluorescein angiogram depicting dry age-related macular degeneration and the direction of OCT scans. **(B)** StratusOCT and **(C)** ultrahigh resolution OCT image of dry age-related macular degeneration. **(D)** A 2x enlargement of the ultrahigh resolution OCT image.[15]

5.6 Wet Age-related Macular Degeneration

Figure 5-14 shows the OCT images acquired from a 55 year old woman with 20/80 vision in her right eye that was diagnosed with wet AMD and choroidal neovascularization (CNV). The late-phase fluorescein angiogram depicts the hyperfluorescence of the new vessels near the foveal region of the right eye. Both OCT images clearly show the highly optically backscattering de novo vessels (CNV) extending above the RPE layer in the foveal region. The CNV produces a focal increase in retinal thickness and altered the normal contour of the foveal pit in this region. The architectural morphology of the intraretinal structure is more clearly

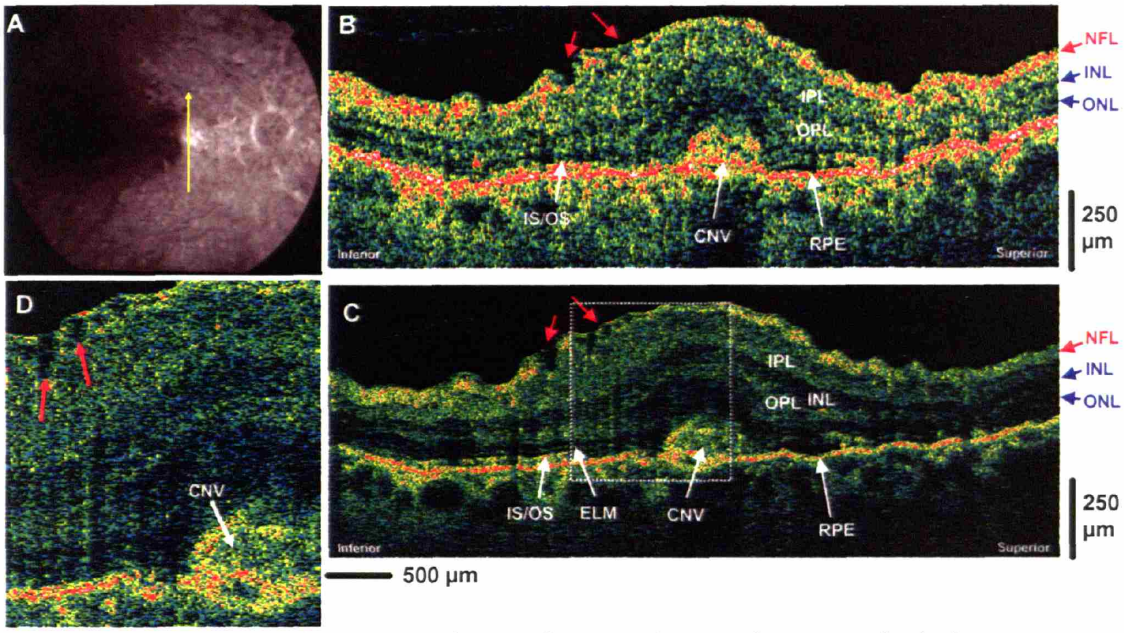

Figure 5-14. **(A)** Late-phase fluorescein angiogram depicting choroidal neovascularization and the direction of OCT scans. **(B)** StratusOCT and **(C)** ultrahigh resolution OCT image of wet MAD with choroidal neovascularization. **(D)** A 2x enlargement of the ultrahigh resolution OCT image.[15]

differentiated in the ultrahigh resolution OCT image. The ultrahigh resolution OCT image also shows disruptions in the RPE layer as well as the photoreceptor inner and outer segments near the region of the CNV. The boundary between the photoreceptor inner and outer segments is not observable in the fovea and the ELM is also not visible. Small irregularities in the retinal nerve fiber layer (NFL) and ganglion cell layers with evidence of epiretinal membrane formation can also be observed in the ultrahigh resolution OCT image (red arrows) as well as in the StratusOCT image. Both StratusOCT and ultrahigh resolution OCT images show the edema as well as the architecture of the inner and outer plexiform and inner and outer nuclear layers. The boundary between the ganglion cell layer and the IPL is difficult to resolve in both images.

5.7 Retinal Pigment Epithelium Detachment

Figure 5-15 shows the OCT images acquired from a 77 year old woman with 20/200 vision in her right eye that was diagnosed with retinal pigment epithelium detachment.

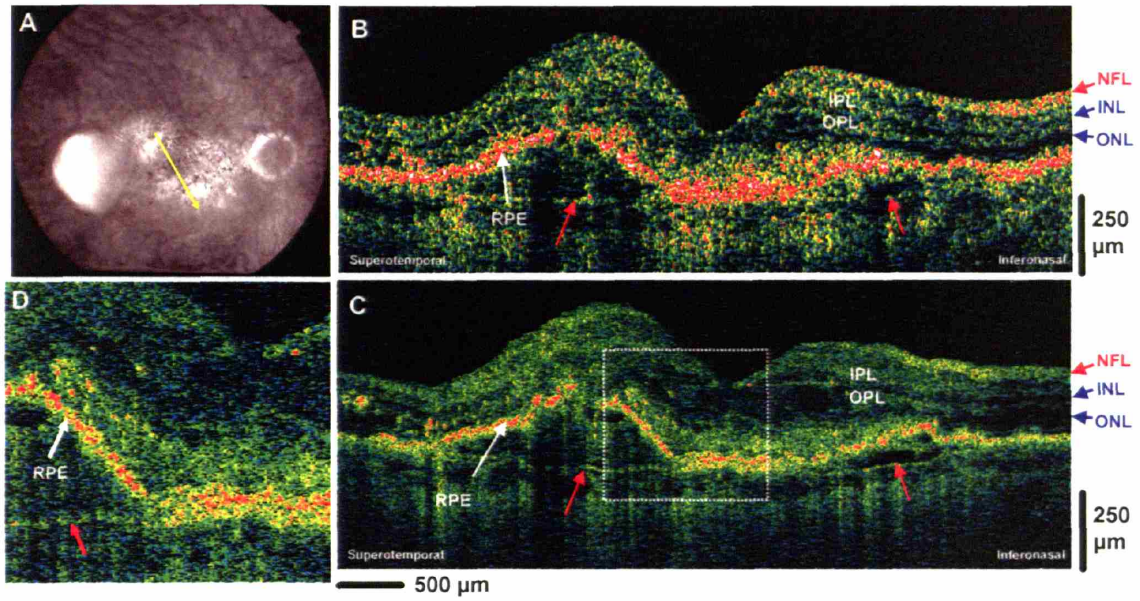

Figure 5-15. (A) Late-phase fluorescein angiography depicting retinal pigment epithelium detachment and the direction of OCT scans. **(B)** StratusOCT and **(C)** ultrahigh resolution OCT image of a patient with retinal pigment epithelium detachment. **(D)** A 2x enlargement of the ultrahigh resolution OCT image.[15]

Both StratusOCT and ultrahigh resolution OCT images show that the RPE appears to be detached in two regions (red arrows). The highly-backscattering RPE layer can be seen to be separated from the underlying choroidal structures in these two regions. The ultrahigh resolution OCT image more clearly shows a very thin backscattering layer (red arrows) below the displaced RPE layer. The anatomical position of this thin layer, underneath the detached RPE, suggests that it may be Bruch's membrane. The ultrahigh resolution image was able to visualize this thin layer more distinctly than the StratusOCT image. The difference between StratusOCT and ultrahigh resolution OCT in the visualization of this layer is more pronounced in the inferior-nasal region of the images. Finally, there is marked loss of structure in the photoreceptor inner and outer segments which can be observed in both OCT images.

5.8 Epiretinal Membrane

Figure 5-16 shows the OCT images acquired from an 81 year old man with 20/25 vision in his right eye that was diagnosed with epiretinal membrane.

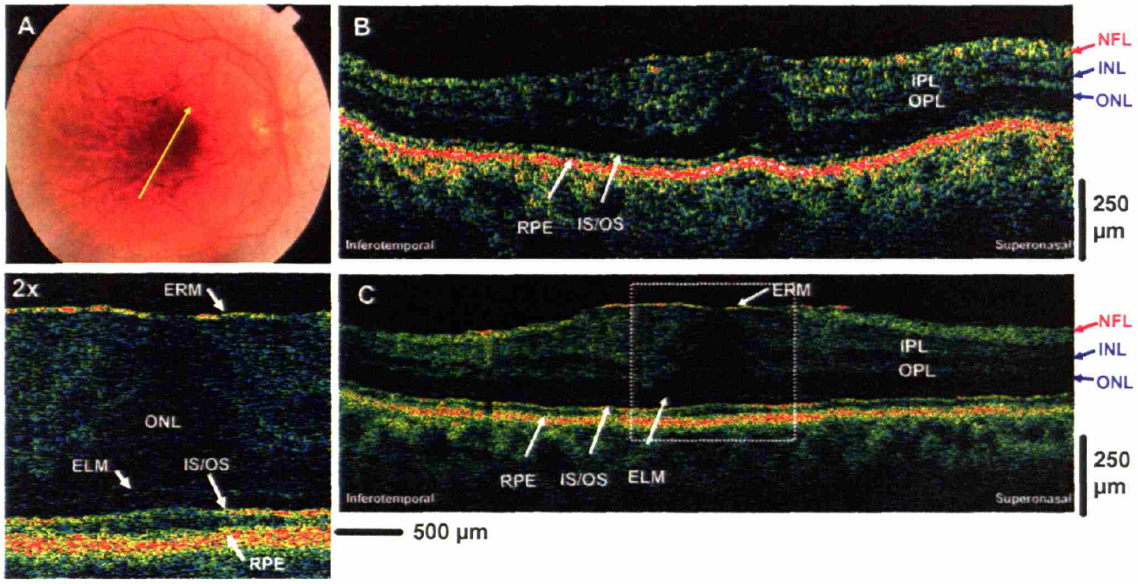

Figure 5-16. (A) Fundus photo depicting epiretinal membrane and the direction of OCT scans. **(B)** StratusOCT and **(C)** ultrahigh resolution OCT image of epiretinal membrane (ERM). **(D)** A 2x enlargement of the ultrahigh resolution OCT image clearly shows the thin highly backreflecting epiretinal membrane that is not visualized in the StratusOCT image.[15]

The fundus photo of the right eye depicts the epiretinal membrane; however, the thin epiretinal membrane (ERM) can only be seen in the ultrahigh resolution OCT but not in the StratusOCT image. In the ultrahigh resolution OCT image, the ERM is visualized as a thin, highly reflective membrane at the vitreomacular interface. The epiretinal membrane appears to be applying traction, distorting the normal foveal pit appearance and increasing the retinal thickness in foveal region. The thin epiretinal membrane is not directly visualized in the StratusOCT image although the abnormal effect of the membrane on the foveal pit contour and the increased thickness of the outer nuclear layer in the fovea can be detected.

5.9 Vitreomacular Traction

Figure 5-17 shows the OCT images acquired from a 46 year old woman with 20/40 vision in her left eye that was diagnosed with vitreomacular traction.

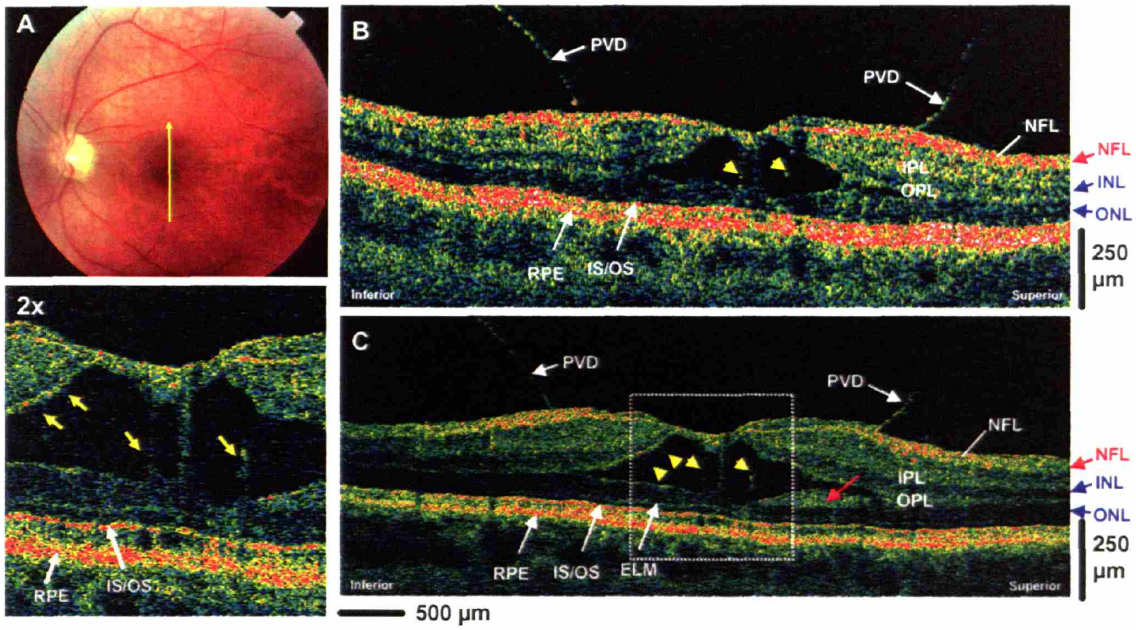

Figure 5-17. (A) Fundus photo depicting vitreomacular traction and the direction of OCT scans. **(B)** StratusOCT and **(C)** ultrahigh resolution OCT image of vitreomacular traction. **(D)** The 2x enlargement of the ultrahigh resolution OCT image shows several distended structures (yellow arrows) spanning the separation of the sensory retina that are suggestive of Müller cells.[15]

Both OCT images clearly show the posterior hyaloid vitreomacular traction causing a separation of the sensory retinal layers. The ultrahigh resolution OCT image shows that the separation occurs between the OPL and ONL. In both OCT images, distended structures (yellow arrows), spanning the separation in the sensory retina can be seen. The location of these structures suggests that they may be Müller cells which remain connected to the retinal layers despite their physical separation. The ultrahigh resolution OCT image facilitates the visualization of these finer structures. The ultrahigh resolution OCT image shows clearly that the RPE, inner and outer segments, ELM, and ONL are intact in spite of the vitreomacular traction. This is also visible in the StratusOCT image, although the architecture of the photoreceptor segments and external limiting membrane (ELM) is less well demarcated. The ultrahigh resolution OCT image shows an area superior to the fovea which might be a separation of the outer plexiform layer. There is a highly optically scattering layer adjacent to the ONL which might be a separated portion of the outer plexiform layer (red arrow).

5.10 Retinitis Pigmentosa

Figure 5-18 shows the OCT images acquired from a 27 year old woman with 20/25 vision in her right eye and an ocular history of retinitis pigmentosa.

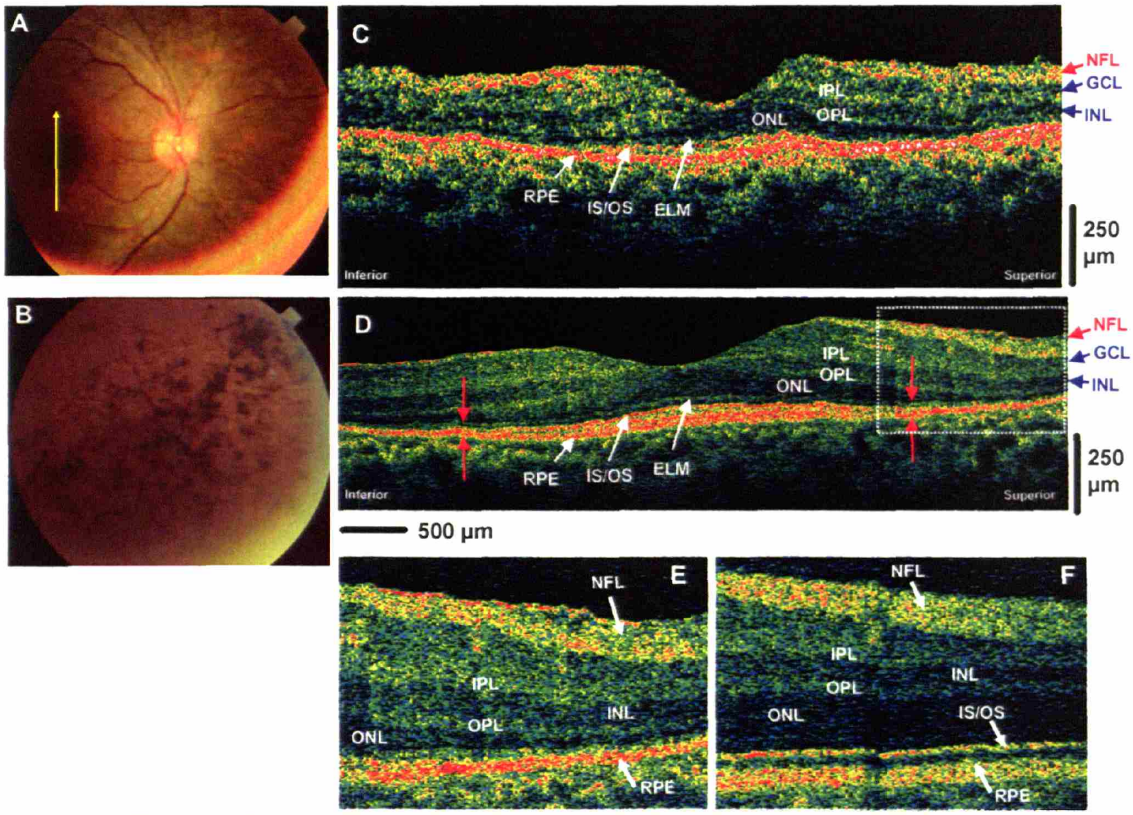

Figure 5-18. (A,B) Fundus photos depicting the presence of pigments in the peripheral retina of a retinitis pigmentosa patient and the direction of OCT scans in the macular region. **(C)** StratusOCT and **(D)** ultrahigh resolution OCT image of retinitis pigmentosa. **(E)** A 2x enlargement of ultrahigh resolution OCT image of the retinitis pigmentosa patient clearly indicates the thinning of the outer nuclear layer and photoreceptor segments when compared with **(F)** a 2x enlargement of a normal subject.[15]

Both OCT images show that there is marked atrophy of the photoreceptor cells in the peripheral macula region. The outer nuclear layer thickness appears normal in the foveal region, but becomes abnormally thin in the periphery of the macula. Other intraretinal layers such as the NFL, IPL, INL, and OPL layers appear relatively normal throughout the OCT images. The relatively normal appearance of the photoreceptor layers (outer nuclear layer, inner and outer

segments) in the fovea of this patient helps to explain why the visual acuity for that patient was 20/25. A close examination of the ultrahigh resolution OCT image reveals that progressive thinning of the photoreceptor inner and outer segments also occurs outside of the foveal region (red arrows). The atrophy of the inner and outer segments causes the highly backscattering IS/OS junction and the RPE layer from being clearly differentiated in the peripheral region of the macula. The peripheral thinning of outer nuclear layer and photoreceptor segments is caused by the progressive atrophy of the rods and cones associated with retinitis pigmentosa. The progressive thinning of the inner and outer segments is not as clearly visualized in the StratusOCT image because the external limiting membrane is not as clearly differentiated as in the ultrahigh resolution OCT image.

5.11 Conclusions

Compared to standard resolution StratusOCT, ultrahigh resolution OCT has an improved ability to visualize smaller structures such as the external limiting membrane, the photoreceptor inner and outer segments, epiretinal membrane, and possibly the Bruch's membrane. Theses structures tend to be very thin or sometimes only weakly backscattering; therefore, they are difficult to visualize using standard resolution StratusOCT. However, the improved understanding of morphologic features visualized in ultrahigh resolution OCT images can be used to improve the interpretation of StratusOCT images. The direct comparison of the ultrahigh resolution OCT to standard resolution StratusOCT enables the development of diagnostic criteria to be used in StratusOCT images alone. In the retinal pigment epithelium detachment case (Figure 5-15), the direct visualization of the underlying Bruch's membrane is possible with ultrahigh resolution OCT. Although the thin Bruch's membrane structure is not readily visualized in the StratusOCT image, the knowledge of its position in the ultrahigh resolution OCT image permits the interpretation of the faint reflection in the standard resolution OCT image as Bruch's membrane. These interpretations can then be applied to standard resolution StratusOCT images alone, without the need to perform ultrahigh resolution OCT, and can be used to enhance the diagnostic utility of StratusOCT imaging.

Ultrahigh resolution OCT also has improved ability over StratusOCT in visualizing the photoreceptor inner and outer segments and the integrity of the photoreceptors in a number of macular pathologies. The ability to visualize the detail of the photoreceptor morphology with

ultrahigh resolution OCT may provide additional information that can help improve the understanding of the pathogenesis and management of various macular diseases. In macular holes, the preservation of the outer segment in the region of the full-thickness hole is visualized much more clearly in ultrahigh resolution OCT than in StratusOCT. The preservation of photoreceptor inner and outer segments in the region of the full-thickness hole which may help to explain why re-apposing the sensory retina back against the RPE through macular hole surgery can often restore visual acuity.[10] In the case of central serous chorioretinopathy, the localized disruption of the photoreceptor layer and the RPE is evident in the ultrahigh resolution OCT image after the resolution of the sub-retinal serous fluid accumulation (Figure 5-11). In contrast, the StratusOCT image of this region does not clearly indicate a disruption of the RPE layer due to the larger speckle size and lower axial resolution of the StratusOCT image. The thinning of the outer nuclear layer caused by the progressive atrophy of the rods and cones associated with retinitis pigmentosa (Figure 5-18) can be visualized directly in both standard and ultrahigh resolution OCT. However, ultrahigh resolution OCT reveals that the atrophy and thinning are also manifest in the photoreceptor inner and outer segments. Therefore, ultrahigh resolution OCT has improved visualization of intraretinal features, and it promises to better elucidate the structural changes which occur in disease pathogenesis as well as to increase the sensitivity for earlier diagnosis and improve monitoring of disease progression and response to treatment.

5.12 References

1. Drexler W, Morgner U, Ghanta RK, et al. Ultrahigh-resolution ophthalmic optical coherence tomography. Nature Medicine 2001;7(4):502-7.

2. Swanson EA, Izatt JA, Hee MR, et al. In vivo retinal imaging by optical coherence tomography. Optics Letters 1993;18(21):1864-6.

3. Gass JDM. Idiopathic senile macular hole: Its early stages and pathogenesis. Arch Ophthalmol 1988;106:629-39.

4. Gass JDM. Reappraisal of biomicroscopic classification of stages of development of a macular hole. Am J Ophthalmol 1995;119:752-9.

5. Hee MR, Puliafito CA, Wong C, et al. Optical coherence tomography of macular holes. Ophthalmology 1995;102(5):748-56.

6. Gaudric A, Haouchine B, Massin P, et al. Macular hole formation: new data provided by optical coherence tomography. Archives of ophthalmology 1999;117(6):744-51.

7. Spaide RF. Macular hole repair with minimal vitrectomy. Retina 2002;22(2):183-6.

8. Spaide RF, Wong D, Fisher Y, Goldbaum M. Correlation of vitreous attachment and foveal deformation in early macular hole states. American journal of ophthalmology 2002;133(2):226-9.

9. Chauhan DS, Antcliff RJ, Rai PA, et al. Papillofoveal traction in macular hole formation: the role of optical coherence tomography. Arch Ophthalmol 2000;118(1):32-8.

10. Ko TH, Fujimoto JG, Duker JS, et al. Comparison of ultrahigh- and standard-resolution optical coherence tomography for imaging macular hole pathology and repair. Ophthalmology 2004;111(11):2033-43.

11. Fankhauser F, Enoch J, Cibis P. Receptor orientation in retinal pathology. A first study. Am J Ophthalmol 1961;52:767-83.

12. Fitzgerald CR, Enoch JM, Birch DG, et al. Anomalous pigment epithelial photoreceptor relationships and receptor orientation. Invest Ophthalmol Vis Sci 1980;19(8):956-66.

13. Fitzgerald CR, Birch DG, Enoch JM. Functional analysis of vision in patients after retinal detachment repair. Arch Ophthalmol 1980;98(7):1237-44.

14. Hee MR, Izatt JA, Swanson EA, et al. Optical coherence tomography of the human retina. Archives of Ophthalmology 1995;113(3):325-32.

15. Ko TH, Fujimoto JG, Schuman JS, et al. Comparison of Ultrahigh and Standard Resolution Optical Coherence Tomography for Imaging Macular Pathology. Ophthalmology in review.

16. Enoch JM. Visualization of wave-guide modes in retinal receptors. Am J Ophthalmol 1961;51:1107-18.

17. Winston R, Enoch JM. Retinal cone receptor as an ideal light collector. J Opt Soc Am 1971;61(8):1120-2.

CHAPTER 6: IMAGING GLAUCOMA

Histological studies have shown that glaucomatous damage is confined to the retinal ganglion cell layer (GCL) and nerve fiber layer (NFL).[1, 2] *In vivo* detection of these changes is the goal of clinical examination of the posterior ocular segment and glaucoma imaging modalities. Currently available modalities allow the detection of glaucomatous changes either in the optic nerve head (ONH) or by measuring the thickness of the retina in the macula or the NFL in the peripapillary region. These capabilities are limited by technological constraints, specifically the axial resolution of the images, preventing the detection of distinctive intraretinal layers. More accurate imaging and quantification of the GCL and NFL might improve glaucoma detection by focusing on the tissue layers that are most prone to glaucoma damage. Ultrahigh resolution OCT of glaucoma patient may provide additional information that is not currently detected with standard resolution StratusOCT. A normal subject and four glaucoma patients representing spectrum of various glaucomatous stages of damage were selected for this study.

6.1 Normal Retinal Anatomy

A forty year old white healthy man with a normal right eye examination and normal perimetry was scanned by ultrahigh resolution OCT and Stratus OCT (Figure 6-1). These scans were used as a reference for following glaucoma patients. Macular scanning with both StratusOCT and ultrahigh resolution OCT was conducted in temporal superior to nasal inferior orientation (Figures 6-1 AI and BI). Distinctive retinal layers could be detected by ultrahigh resolution OCT: nuclear retinal layers (ganglion cell layer, outer and inner nuclear layers) have low optical backscattering, while the NFL and the plexiform retinal layers are highly backscattering.[3] The oblique orientation of the scan causes the asymmetry in NFL thickness

because this layer is thinner in the temporal aspect of the macula (left side of the scan) and thicker at the maculopapillary bundle (right side).

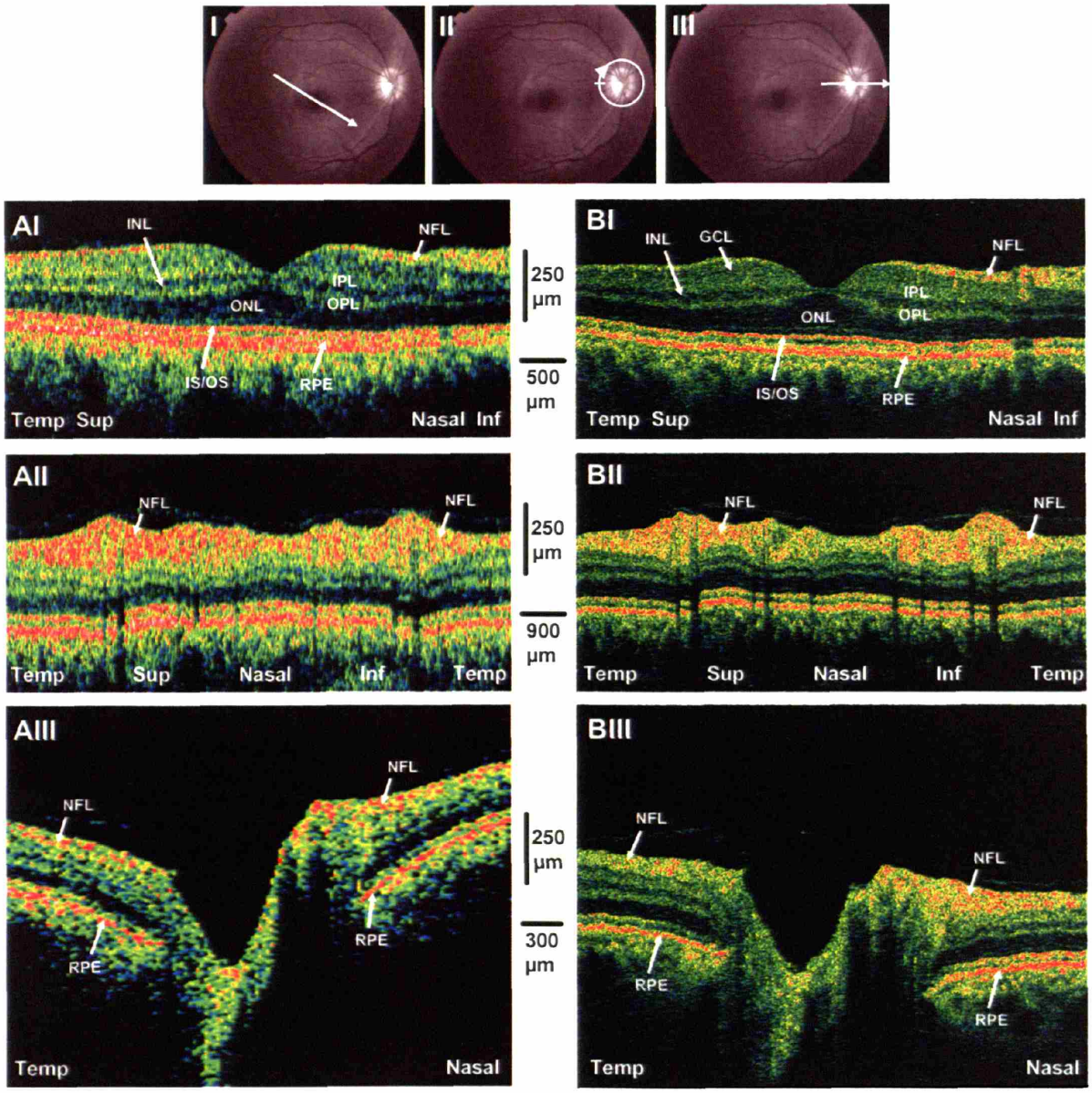

Figure 6-1. StratusOCT (A) and ultra-high resolution OCT (B) scans of a normal subject. Scans I are macular linear scans and the orientation of the scans are depicted on the top left image. Peripapillary circular scans are shown in panel II and the optic nerve head linear scans in panel III.[4]

Circumpapillary OCT images were aligned by temporal, superior, nasal, inferior and temporal quadrants from the left to the right side of the image (Figures 6-1 AII and BII). The most prominent feature in normal peripapillary retina is the wide anterior red band representing the NFL. This band is typically thicker in the superior and inferior regions and thinner in the temporal and nasal regions giving the characteristic "double hump" NFL configuration. Detailed observation reveals that the superior and inferior "humps" include a localized central thinning in the vertical poles of the optic disc. Black vertical streaks are due to a shadowing effect of blood vessels (Figures 6-1 A, B).

Optic nerve head scans were performed in the horizontal temporal to nasal orientation (Figures 6-1 AIII and 1BIII). The ONH is clearly detectable as the opening in the RPE layer. The disc has a shallow cup with mild slopes. The NFL is thickened in the nasal aspect of the ONH compared with the temporal aspect. The attachment of the posterior hyaloid membrane to the temporal margin of the ONH is evident on both standard and ultrahigh resolution OCT images.

6.2 Early Glaucoma

A 53 year old white woman with normal tension glaucoma in her left eye was treated medically with latanoprost and brinzolamide and two sessions of selective laser trabeculoplasty. On examination, the visual acuity (VA) was 20/20 and the intraocular pressure (IOP) was 13 mmHg. Pachymetry of the cornea was 541 μm and the anterior chamber was normal with an open angle. Mild opacification of the lens was noted and moderate cupping of the optic nerve head with a temporal superior rim notch (Figure 6-2 A). VF revealed an inferior nasal defect (Figure 6-2 A).

OCT scans of the macula were conducted in the temporal superior to nasal inferior orientation (Figures 6-2 BI and CI). Marked thinning of the NFL and GCL are noted mainly in the periphery of the temporal aspect of the macula corresponding with the inferior nasal defect in the perimetry. Thinning of NFL and ganglion cell layer is observed also in the periphery of the nasal aspect of the macula. Circumpapillary scanning demonstrated NFL thinning in the superior region with a localized punched-out defect corresponding to the ONH rim notch and the inferior nasal VF defect (Figures 6-2 BII and CII). Optic nerve head scans were obtained in temporal

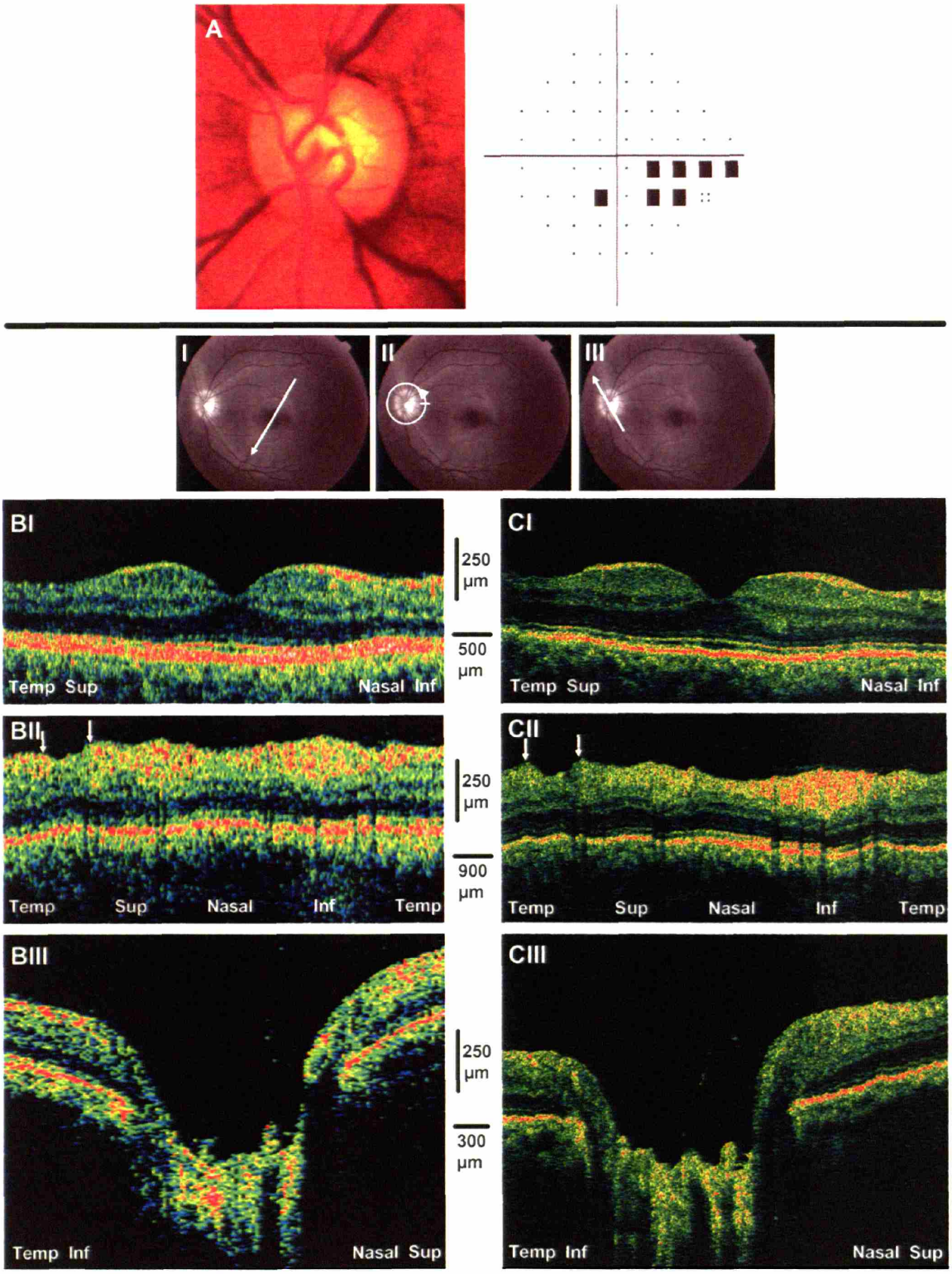

Figure 6-2. Optic disc photograph (A) of early glaucomatous damage demonstrating moderate cupping and superior temporal neuroretinal rim thinning. Visual field defect is presented in the inferior nasal region (A). StratusOCT scans are presented in section B and ultrahigh resolution OCT images in section C. The arrowheads highlight focal nerve fiber layer defect in the peripapillary scans (II). Shallow cupping is evident in the optic nerve head scans (III).[4]

inferior to nasal superior orientation (Figures 6-2 BIII and CIII). The thickness of the NFL is diminished on both sides of the ONH, with a large and deep cup with steep slopes. Large blood vessels are noted at the bottom of the optic disc cup.

6.3 Moderate Glaucoma

A 41 year old Asian man with newly diagnosed primary open angle glaucoma in the right eye was treated with latanoprost. On examination, VA was 20/25 and IOP was 22 mmHg. The anterior chamber was unremarkable except for mild deposition of pigment in the angle. The posterior segment reveals asymmetric cupping with a large cup in the right eye and neuroretinal rim notch in the temporal inferior segment (Figure 6-3 A). VF testing showed superior and inferior arcuate defects, more pronounced in the superior hemifield (Figure 6-3 A).

Macular scans were obtained in the temporal inferior to nasal superior orientation (Figures 6-3 BI and CI). Thinning of the NFL and GCL was noted throughout the macular scan mostly pronounced in the inferior sector. Peripapillary scan shows thinning of the NFL in all sectors (Figures 6-3 BII and CII). The signal obtained from the RPE is evenly distributed along the scan, therefore the diminished signal from the upper layers of the retina reflects true tissue atrophy due to the glaucomatous process. Scanning of the ONH was obtained in the horizontal temporal to nasal orientation (Figures 6-3 BIII and CIII). Severe attenuation of the NFL is observed on both sides of the ONH. A large, deep and steep disc cup is noted with the major blood vessel trunk at the bottom of the cup.

6.4 Severe Glaucoma

A 43 year old white man with juvenile open angle glaucoma in his right eye had a trabeculectomy and was treated with brimonidine, dorzolamide, timolol and travoprost. VA was 20/25 and IOP was 18 mmHg. On examination of the anterior segment, a flat superior bleb was noted and angle was open. The posterior segment was found to have marked ONH cupping with marked attenuation of the rim in the temporal inferior quadrant (Figure 6-4 A). VF showed a dense superior hemifield defect (Figure 6-4 A).

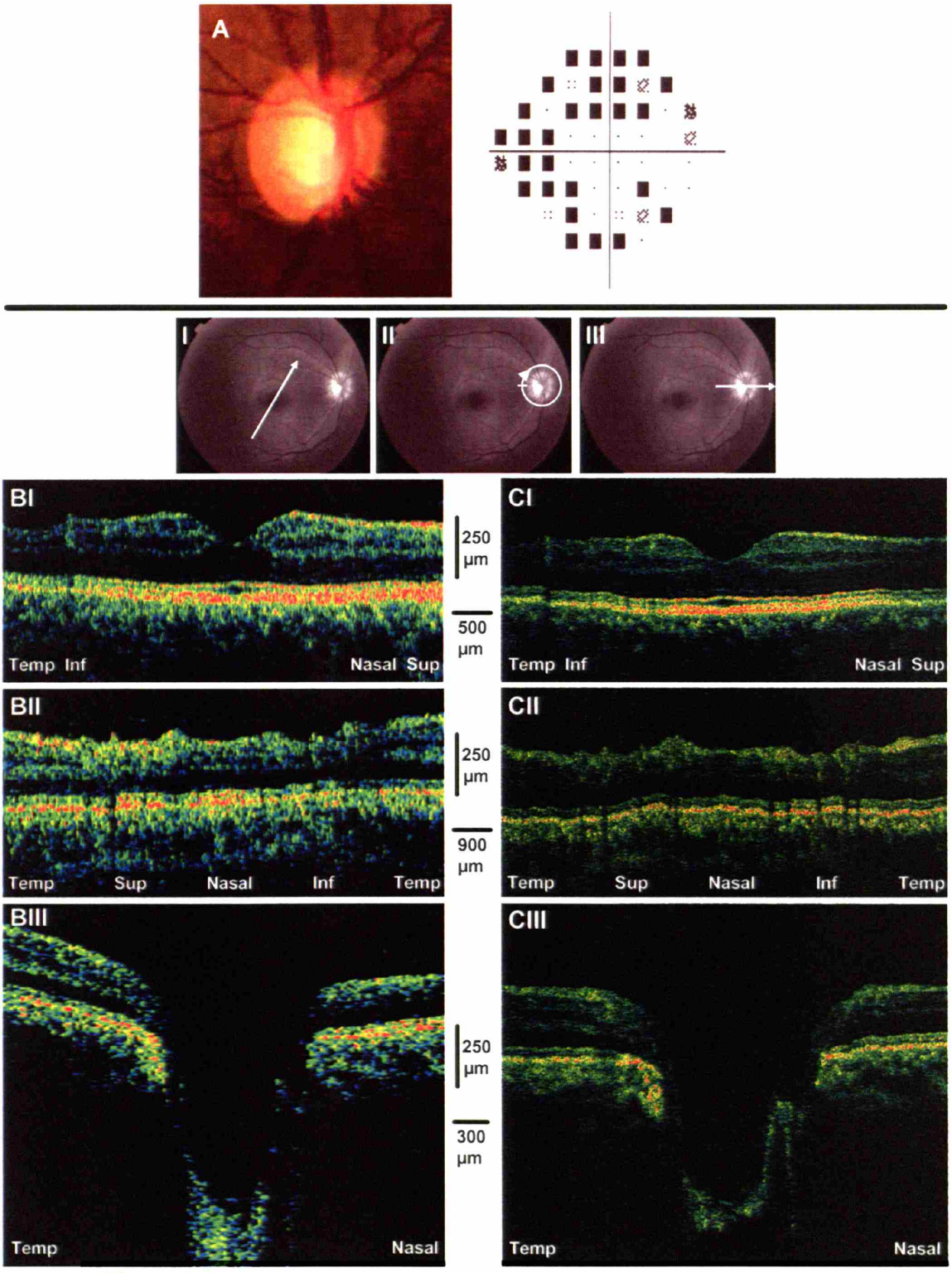

Figure 6-3. Optic disc photograph (A) of moderate glaucomatous damage demonstrating moderate cupping and inferior temporal neuroretinal rim thinning. Superior and inferior arcuate defects are shown in the visual field test (A). StratusOCT scans are presented in section B and ultrahigh resolution OCT images in section C. The nerve fiber layer is attenuated throughout the peripapillary scans (II). Large and deep optic nerve cupping is evident in the optic nerve head scans (III).[4]

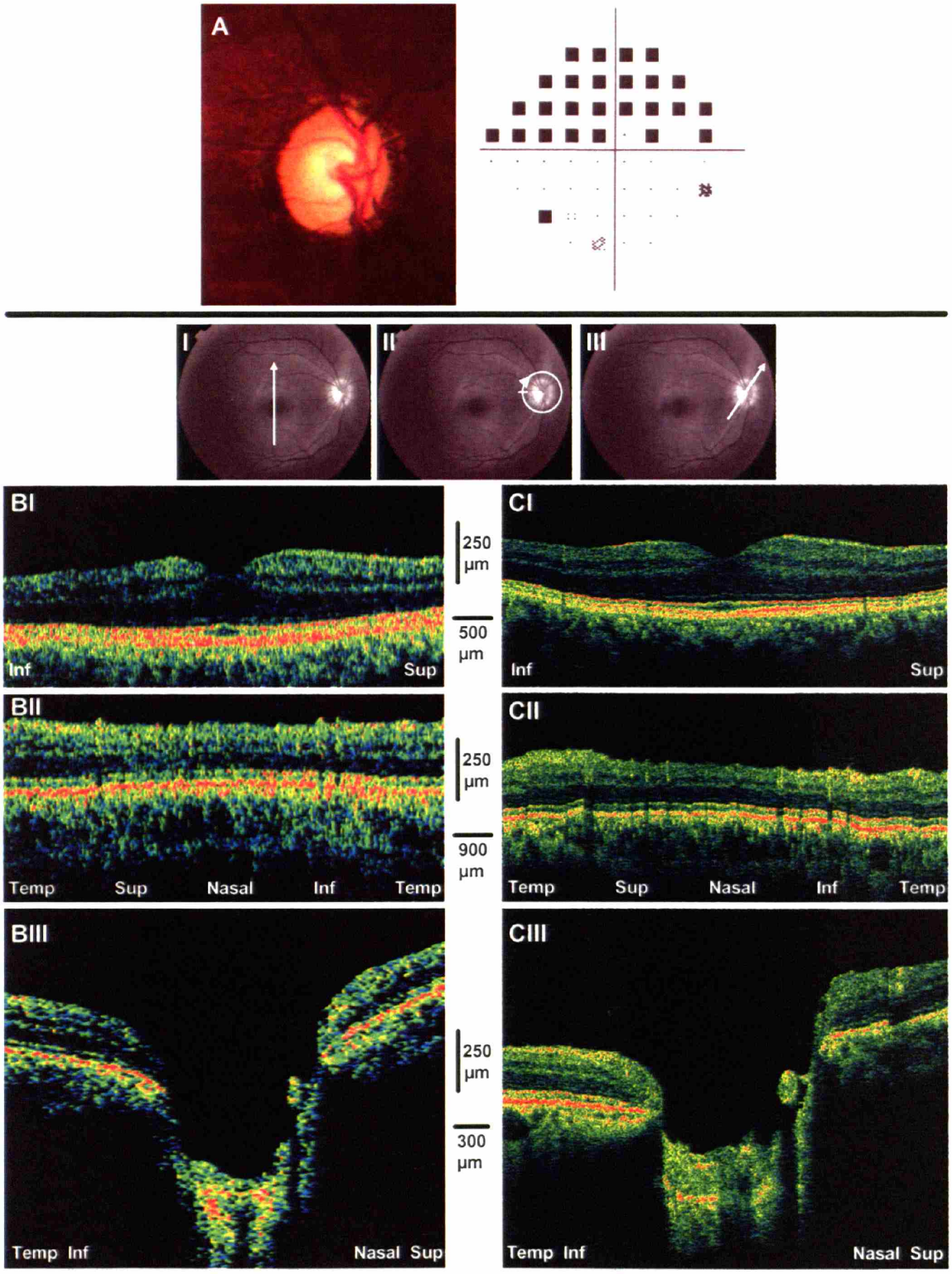

Figure 6-4. Optic disc photograph (A) of advance glaucomatous damage demonstrating large cupping and inferior temporal neuroretinal rim thinning with superior hemifield visual field loss (A). StratusOCT scans are presented in section B and ultrahigh OCT in section C. Marked thinning of the NFL and GCL is evident in both sides of the fovea mostly pronounced in the inferior region (I) as well as in the peripapillary scans (II). Optic nerve head scans showed deep cupping with elimination of the neuroretinal rim (III).[4]

Macular scans were obtained in the vertical inferior to superior orientation (Figures 6-4 BI and CI). At this orientation it is expected to find similar retinal patterns between both sides of the scan. Marked thinning was observed in both superior and inferior regions most pronounced in the periphery of the inferior region corresponding with the superior VF defect. The glaucomatous damage in the superior retina as observed by the OCT was not detected by perimetry at the time of testing. NFL thickness was diminished throughout the peripapillary region (Figures 6-4 BII and CII). This finding is fully appreciated when compared to the scan of the normal subject (Figures 6-1 AII and BII) taking into account that both subjects are from the same age range. Scanning of the ONH was obtained in the temporal inferior to nasal superior orientation (Figures 6-4 BIII and CIII). The scans are remarkable for attenuation of the NFL and deep and large optic disc cupping. No neuroretinal rim is noted in the temporal aspect of the disc.

6.5 Localized Glaucomatous Damage

A 64 year old white woman with normal tension glaucoma in the left eye was treated with selective laser trabeculoplasty and medically with brinzolamide and bimatoprost. VA was 20/20 and IOP 12 mmHg. Pachimetry of the left cornea was 540 μm and the angle was open. Posterior segment examination revealed a near total excavation of the ONH and a wedge shaped NFL defect in the temporal inferior sector (Figure 6-5 A left). VF showed a reproducible early superior paracentral defect (Figure 6-5 A).

Two linear scans were obtained with StratusOCT and ultrahigh resolution OCT through the clinically detected NFL defect (Figures 6-5B and 6-5C). The alignment of the scans (I and II) is presented in Figure 6-5A. A clearly visible thinning of the nerve fiber layer is noted and is surrounded by near normal thickness of the NFL layer. OCT scanning through the nerve fiber layer defect showed marked thinning of this layer on OCT surrounded by normal thickness nerve fiber layer. The white arrows in section B and C depicts the extent of nerve fiber layer thinning in the OCT images. As indicated in the red-free fundus photography, the thinning of the NFL is worse away from the optic nerve head.

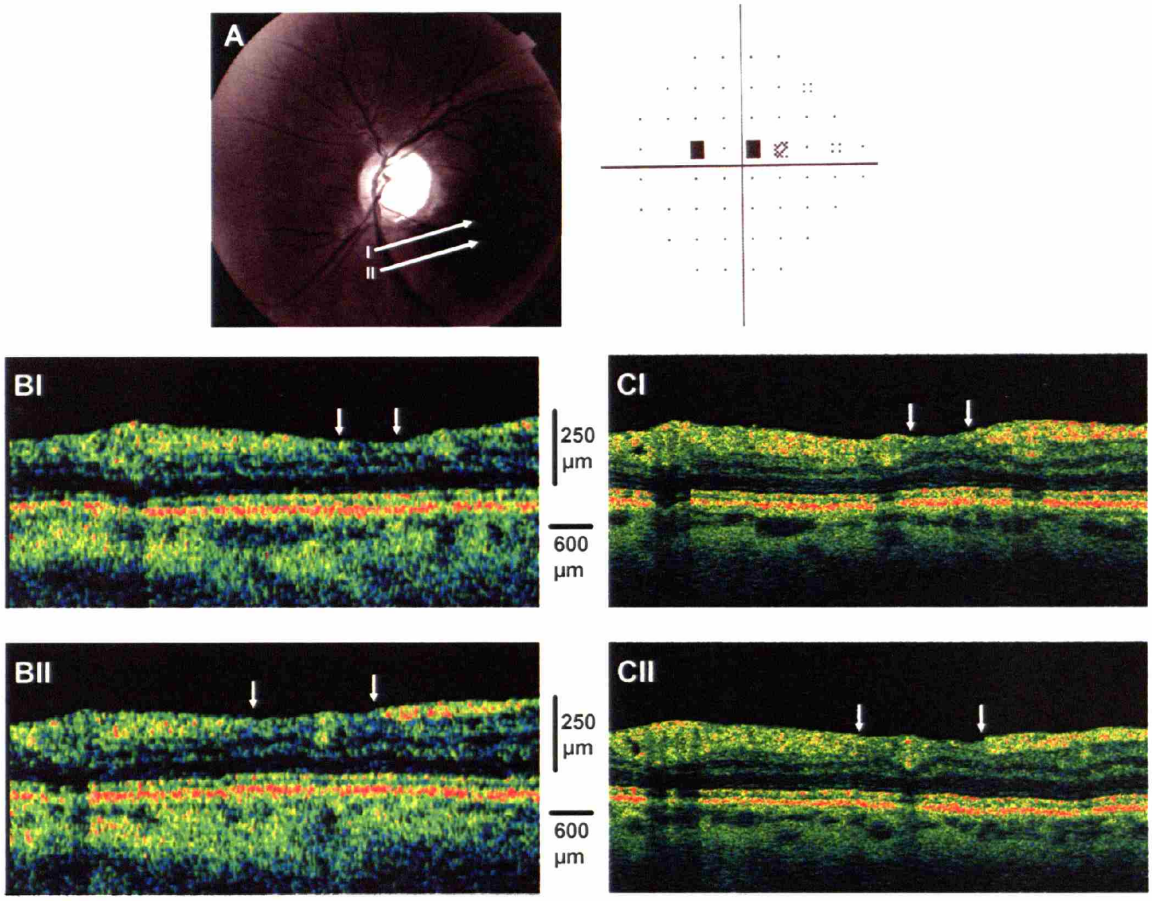

Figure 6-5. Red-free fundus photograph of temporal inferior nerve fiber layer defect (A, left). The visual field showed early superior paracentral defect (A). StratusOCT scans are presented in section B and ultrahigh resolution OCT images in section C. The white arrows in section B and C depicts the extent of nerve fiber layer thinning in the OCT images.[4]

6.6 Conclusions from Glaucoma Imaging

This study presents the investigation of ultrahigh resolution OCT imaging in glaucoma patients. Using the clinical ultrahigh resolution OCT system, we were able to discern retinal layers with a high degree of precision, specifically discriminating areas of glaucoma damage and discerning the differences in regions that were damaged from those that were not. Furthermore, we were able to apply the ultrahigh resolution OCT findings to standard resolution StratusOCT images and extract additional information from the StratusOCT images that we were unable to appreciate prior to ultrahigh resolution OCT imaging. We could evaluate finer details on the StratusOCT with the additional direction provided by the ultrahigh resolution OCT images.

The improved visualization provided by ultrahigh resolution OCT allowed the recognition of intraretinal structures as well as minute glaucomatous structural changes that could not be detected by other ocular imaging modalities or previous versions of commercial OCT devices. Since glaucomatous damage is confined to the NFL and GCL, the enhanced visualization might provide an important tool to detect these changes. The ability to visualize the layers which are specifically prone to glaucomatous damage improves the ability to detect the damage by focusing only on the measurements from those layers which are directly involved in the pathological glaucomatous process. These outer layers might be damaged due to other pathologies and thus induce total retinal thickness changes that do not reflect the glaucomatous damage. This property of the ultrahigh resolution OCT might be of particular value for longitudinal evaluation of glaucoma patients. Further investigation and construction of software allowing for automatic segmentation of intraretinal layers may provide quantitative measurements of these layers and further enhance clinical use.

The optical properties of normal retina enable the recognition of retinal layers in the ultrahigh resolution OCT scans similar to those obtained in histological sections (Figure 6-1 B). With the aid of ultrahigh resolution OCT, most of these features can be detected in the standard resolution StratusOCT scan (Figure 6-1 A). However, the ability to differentiate between layers and identify minute features is clearly enhanced by the ultrahigh resolution OCT scans.

Figures 6-2 B and 6-2C demonstrate an example in which the ultrahigh resolution OCT showed a localized NFL defect in the circumpapillary scan which was much less obvious in the standard resolution StratusOCT scan. This example highlights the advantage that ultrahigh resolution OCT provides in improving the visualization of small abnormalities. With the additional knowledge gained from the ultrahigh resolution OCT, one can more easily identify the area of abnormality in the corresponding standard resolution StratusOCT image (Figure 6-2 BII).

Defining the extent of the intraretinal (axial) glaucomatous damage can be challenging using StratusOCT (Figure 6-3 BII, inferior region, Figure 6-5 B). Ultrahigh resolution OCT showed a definitive attenuation of the NFL indicative of advanced tissue destruction (Figure 6-3 CII, inferior region, Figure 6-5C).

Numerous studies have shown that structural changes precede functional damage.[5-14] Figure 6-4 demonstrates a case where, in addition to the damage that corresponds to the VF

damage, further structural damage could be detected with both the standard and ultrahigh resolution OCT which was not yet apparent in VF testing.

Previous studies have shown the advantages of the ultrahigh resolution OCT in detecting retinal pathologies.[15, 16] The enhanced resolution offered by ultrahigh resolution OCT with the specific recognition of the NFL and GCL should improve the capabilities to detect glaucomatous damage. Moreover, these features have the potential of allowing the recognition of glaucomatous damage in the presence of other ocular pathologies that involve other retinal layers. The enhanced capabilities of ultrahigh resolution OCT over standard resolution OCT promises to improve the detection of glaucomatous retinal abnormalities.

6.7 References

1. Quigley HA, Addicks EM. Quantitative studies of retinal nerve fiber layer defects. Arch Ophthalmol 1982;100(5):807-14.

2. Harwerth RS, Carter-Dawson L, Shen F, et al. Ganglion cell losses underlying visual field defects from experimental glaucoma. Invest Ophthalmol Vis Sci 1999;40(10):2242-50.

3. Toth CA, Narayan DG, Boppart SA, et al. A comparison of retinal morphology viewed by optical coherence tomography and by light microscopy. Archives of ophthalmology 1997;115(11):1425-8.

4. Wollstein G, Paunescu LA, Ko TH, et al. Ultrahigh-resolution optical coherence tomography in glaucoma. Ophthalmology 2005;112(2):229-37.

5. Sommer A, Pollack I, Maumenee AE. Optic disc parameters and onset of glaucomatous field loss. I. Methods and progressive changes in disc morphology. Arch Ophthalmol 1979;97(8):1444-8.

6. Pederson J, Anderson D. The mode of progressive disc cupping in ocular hypertension and glaucoma. Archives of Ophthalmology 1980;98:490-5.

7. Sommer A, Quigley HA, Robin AL, et al. Evaluation of nerve fiber layer assessment. Arch Ophthalmol 1984;102(12):1766-71.

8. Sommer A, Katz J, Quigley HA, et al. Clinically detectable nerve fiber atrophy precedes the onset of glaucomatous field loss. Arch Ophthalmol 1991;109(1):77-83.

9. Quigley HA, Katz J, Derick RJ, et al. An evaluation of optic disc and nerve fiber layer examinations in monitoring progression of early glaucoma damage. Ophthalmology 1992;99(1):19-28.

10. Zeyen TG, Caprioli J. Progression of disc and field damage in early glaucoma. Arch Ophthalmol 1993;111(1):62-5.

11. Quigley HA, Enger C, Katz J, et al. Risk factors for the development of glaucomatous visual field loss in ocular hypertension. Arch Ophthalmol 1994;112(5):644-9.

12. Sommer A, Miller N, Pollack I. The nerve fiber layer in the diagnosis of glaucoma. Archives of Ophthalmology 1997;95:2149-56.

13. Chauhan BC, McCormick TA, Nicolela MT, LeBlanc RP. Optic disc and visual field changes in a prospective longitudinal study of patients with glaucoma: comparison of scanning laser tomography with conventional perimetry and optic disc photography. Arch Ophthalmol 2001;119(10):1492-9.

14. Kass MA, Heuer DK, Higginbotham EJ, et al. The Ocular Hypertension Treatment Study: a randomized trial determines that topical ocular hypotensive medication delays or prevents the onset of primary open-angle glaucoma. Arch Ophthalmol 2002;120(6):701-13; discussion 829-30.

15. Drexler W, Sattmann H, Hermann B, et al. Enhanced visualization of macular pathology with the use of ultrahigh-resolution optical coherence tomography. Archives of Ophthalmology 2003;121(5):695-706.

16. Ko TH, Fujimoto JG, Duker JS, et al. Comparison of ultrahigh- and standard-resolution optical coherence tomography for imaging macular hole pathology and repair. Ophthalmology 2004;111(11):2033-43.

CHAPTER 7: FUTURE WORK AND OUTLOOK

Ultrahigh resolution optical coherence tomography has been demonstrated in research and clinical ophthalmology to achieve axial resolutions of up to ~1 μm in animal eyes and ~3 μm in human eyes. The enhanced imaging capabilities of ultrahigh resolution OCT can improve the visualization of fine intraretinal architectural morphology such as the ganglion cell layer, photoreceptor layers, and retinal pigment epithelium. Many of these structures undergo pathologic changes in retinal disease, and ultrahigh resolution OCT can enhance the visualization of morphologic changes associated with retinal diseases (Chapter 5, 6)

7.1 Current Limitations of Ultrahigh Resolution OCT

Despite the successful application and the benefits of ultrahigh resolution OCT in clinical ophthalmology, there are currently several limitations in this technology.

Broadband Laser Light Source

All current clinical ultrahigh resolution OCT systems utilize femtosecond lasers as the imaging light source.[1-3] Commercial femtosecond lasers are expensive (around $100,000), laser cavity alignments are sensitive to room temperature changes, and femtosecond lasers can be difficult to operate without specialized trained. Thus, the requirement of a femtosecond laser for ultrahigh resolution OCT imaging presents a major challenge to the widespread adoption of this technology into the clinical setting. In order to enable widespread implementation of ultrahigh resolution OCT imaging in the ophthalmology clinic, an inexpensive and robust imaging light source that is capable of generating high resolution images must be realized. Superluminescent diode (SLD) sources are compact, robust, easy to operate, and much less expensive than

femtosecond solid-state lasers. However, the bandwidths of commercial SLD sources were relatively limited. Consequently, OCT axial resolutions were limited to ~10 μm when SLD sources were used. The development of a broadband SLD light source for ultrahigh resolution OCT will greatly enhance the clinical utility of ultrahigh resolution OCT imaging.

Limited Image Acquisition Speed

Current ophthalmic OCT systems have limited image acquisition time which restricts the amount of cross-sectional information that can be acquired from the retina. The StratusOCT system performs imaging at 400 axial scans (transverse pixels) per second, and can acquire a 512 axial scan StratusOCT image in ~1.3 second. The clinical ultrahigh resolution OCT systems perform imaging at 150 axial scans (transverse pixels) per second, and a 600 axial scan OCT image is acquire in approximately 4 seconds.[2] The relatively slow imaging speed of OCT systems such as StratusOCT and the ultrahigh resolution OCT has limited the number of scans that can be performed on patients in a single imaging session. In addition, the slow imaging speed of current OCT systems means that re-registration algorithms are necessary to correct for patient motion artifacts which are present in both StratusOCT and ultrahigh resolution OCT images. These re-registration algorithms automatically align adjacent axial scans and have been used to correct for axial motion in the OCT images of all previous prototype and commercial OCT systems.[4] Although aligning adjacent axial scans do not change relative measurements such as retinal thickness, they can obscure the true topography of the retina. In addition, these algorithms are ineffectual if the retina moves out of the axial measurement range, or if there is significant motion in the transverse direction which can also alters the position of the scanning OCT beam on the retina. In StratusOCT, motion artifacts can be reduced by acquiring OCT images with smaller number of axial scans; however, this also limits the amount of cross-sectional information that can be obtained from the retina. Even though ultrahigh resolution OCT has enhanced capabilities over StratusOCT at visualizing intraretinal features, the imaging speeds in ultrahigh resolution OCT are typically slower than StratusOCT and motion artifacts are typically more severe in the images. The StratusOCT images are usually not corrected for axial motion because axial motion is usually not significant in ~1.3 second. The ultrahigh resolution OCT images are always corrected for motion because the motion artifacts can be significant.

New Ultrahigh Resolution OCT Technologies

Within the last couple of years, new developments in OCT technology have provided solutions to the challenges currently facing ultrahigh resolution OCT in regards to its complicated light source and limited imaging speed. These technology advances may enable the development of high-speed ultrahigh resolution OCT systems that is robust and easy to operate in the clinical setting and can achieve imaging speed that is orders of magnitude faster than current ultrahigh resolution OCT systems.

7.2 Broadband Superluminescent Diode Light Source

Broadband superluminescent sources for OCT imaging have been previously investigated, but *in vivo* ultrahigh resolution OCT imaging has not been possible. Broadband superluminescence generated from a titanium:sapphire crystal pumped with high-power lasers can provide ~2 μm OCT axial resolution.[5, 6] However, the power that can be coupled into a signal mode fiber (in the μW range) is too low for high-speed in vivo imaging.[5, 6] Titanium:sapphire waveguides can be used to improve the coupling efficiency of the superluminescence into a single-mode fiber, but the power is still not sufficient for *in vivo* imaging.[7-9] Superluminescent diodes (SLD) are semiconductor high-gain optical amplifiers which generate amplified spontaneous emission. Early superluminescent diodes had a similar structure to diode lasers, except that antireflection coatings were applied to the diode facets to reduce feedback and inhibit lasing. However, spectral modulation of the diode output and lasing from parasitic feedback limited the output power of these designs to a few milliwatts. The use of angled waveguide structures further reduced feedback to enable higher power operation without spectral modulation or lasing.[10-12] The use of quantum well structures enabled broad gain bandwidths to be achieved at lower current densities than was possible with "bulk" heterostructure devices.[11] In order to further increase the optical output bandwidth while maintaining high output power, wavelength division multiplexing (WDM) of spectrally shifted SLDs can be performed. Early work demonstrated improvement in axial resolution from 10 μm to 6 μm using two wavelength division multiplexed SLDs.[13] In another study, using a dual-beam OCT approach, two spectrally displaced SLD beams were combined to achieve an effective bandwidth of 50 nm, corresponding to an OCT axial resolution of 6-7 μm.[14] However, the output powers of these sources were low and thus have limited signal-to-noise performance for

in vivo OCT imaging applications. Furthermore, the total optical bandwidth was not sufficient to achieve ultrahigh axial resolutions of 2-3 μm, which is possible with femtosecond solid-state laser light sources.

Recently, advancements in commercial superluminescent diode technology has improved the output bandwidth of these devices and it has been demonstrate that it is now possible to achieve ultrahigh resolution OCT imaging of 2-3 μm with the use of broadband SLD light sources.[15] This broadband source consists of two independent SLD diodes where the two optical outputs are multiplexed to achieve a total bandwidth of 155 nm and > 4 mW total CW output power. An axial resolution of ~2.3 μm was obtained in scattering tissue and an axial resolution of ~3.2 μm was obtained in the retina. The image quality and resolution in both scattering tissue and the retina are comparable to those obtained using femtosecond solid-state laser sources. This result demonstrates the ability to achieve *in vivo* ultrahigh resolution OCT imaging without the need for femtosecond solid-state lasers.

Multiplexed SLD Light Source

The broadband SLD source was a new prototype developed by Superlum Diodes, Ltd. and consists of two spectrally multiplexed, independently driven SLD diodes operating at 840 nm and 920 nm, respectively. An SLD diode based on a SQW (GaAl)As heterostructure[16] and a second recently-developed SLD diode based on a SQW (InGa)As/(AlGa)As heterostructure with graded-index waveguides[17] were used. The SLDs have optical outputs with overlapping spectral bands that can be combined with a broadband fiber coupler. A custom built broadband single-mode fiber Y-coupler based on fiber GRIN microlenses and miniature partially transmitting mirrors with dielectric multilayer coatings was developed to spectrally multiplex the SLD outputs. In the spectral range of 750-1100 nm, a coupling ratio of close to 50% and an insertion loss of less than 1 dB were achieved with this coupler. The combined SLD output provides 155 nm of bandwidth at a center wavelength of 890 nm with > 4 mW of CW output power. Compared to a solid-state laser, this broadband SLD source is quite compact and has a total footprint of only 31 x 26 x 15 cm including the power supply, or 31 x 15 x 5 cm for the SLD and multiplexer package alone. Figure 7-1 shows a photograph of this broadband SLD light source and its size compared to a standard ruler. The total cost of this light source is about an order of magnitude less than that of a typical commercial Ti:sapphire femtosecond laser. Another

advantage of the broadband SLD light source is that it is easy to operate. As Figure 7-1 indicates, this light source operation consists of the power switch and two buttons which turn on the individual SLD drivers separately. Unlike the femtosecond laser, the broadband SLD does not require laser alignment and modelocking operations by the user. Therefore, it can easily be operated by an ophthalmic technician and is well suited to be implemented in the ophthalmology clinic.

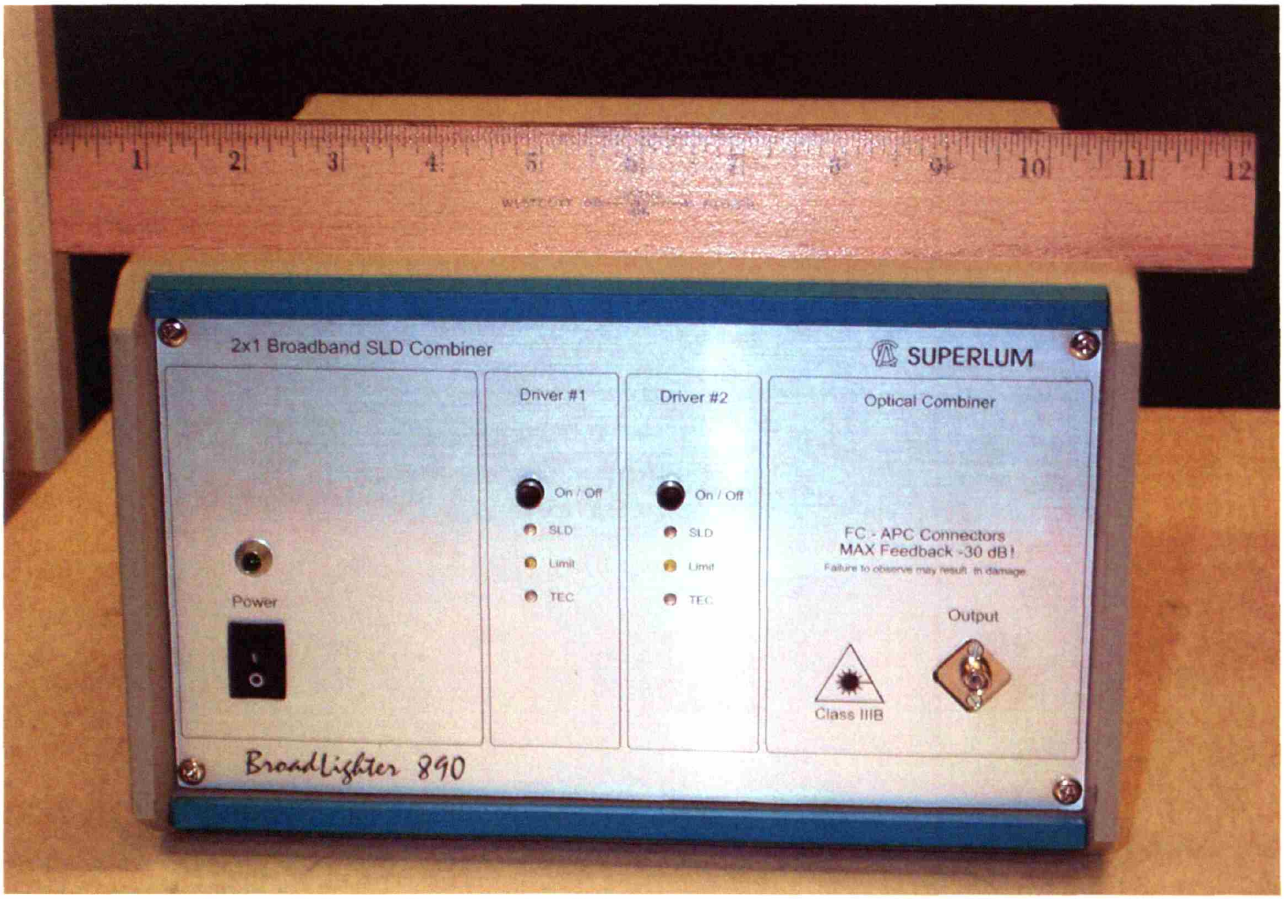

Figure 7-1. A photograph of the commercial broadband SLD light source prototype (Broadlighter 890, Superlum Diodes Ltd., Moscow, Russia). The light source is easy to operate and has a total footprint of only 31 x 26 x 15 cm.

Ultrahigh Resolution OCT System Considerations

Figure 7-2 illustrates the schematic of the OCT system used in test the broadband SLD light source for ultrahigh resolution imaging. The laboratory ultrahigh resolution OCT system was used for *in vivo* animal imaging and the clinical ultrahigh resolution OCT system was used

for *in vivo* retinal imaging. The sample arm consists of either an OCT microscope (for *in vivo* imaging of the hamster cheek pouch) or a modified ophthalmic slit lamp (for *in vivo* retinal imaging). Typical OCT systems usually operate at a detection frequency somewhere between 100 kHz and 10 MHz. Since the SLD source has low excess RF intensity noise in this range, dual-balanced detection is not required and high sensitivity can be obtained by using a single detector. However, the SLD source is sensitive to optical feedback, so special care was exercised to suppress all back reflections in the system to less than –30 dB. The reteroreflected reference arm power is kept to be within this limit and the typical retroreflected sample arm power is even lower. A broadband 50/50 fiber optic coupler (Gould Electronics Inc.) that supported the full spectrum of the SLD source was used for the Michelson interferometer. The reference arm of the interferometer contains adjustable wedges of BK7 glass and fused silica (FS) for dispersion compensation. When conducting ophthalmic imaging, the reference arm also contains a 24-mm (normal eye length) water cell to match the dispersion from the vitreous of the eye. Polarization controllers were used in the reference and sample arms to match the polarization states of the interfering fields, maximizing the output of the interferometer.

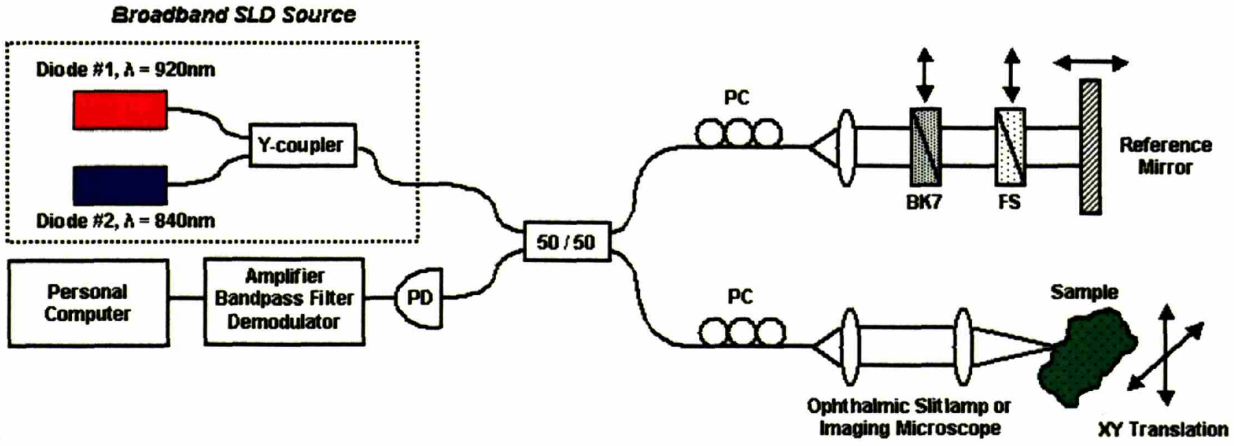

Figure 7-2. Schematic of the OCT system using a broadband SLD light source for *in vivo* ultrahigh resolution OCT imaging. A single detector was used due to the low excess noise of the SLD source. Dispersion matching elements (BK7, FS) in the reference arm were used to match the dispersion of optical elements in the sample arm. Polarization controllers (PC) allowed polarization adjustments to maximize field intensity in the interferometer.[15]

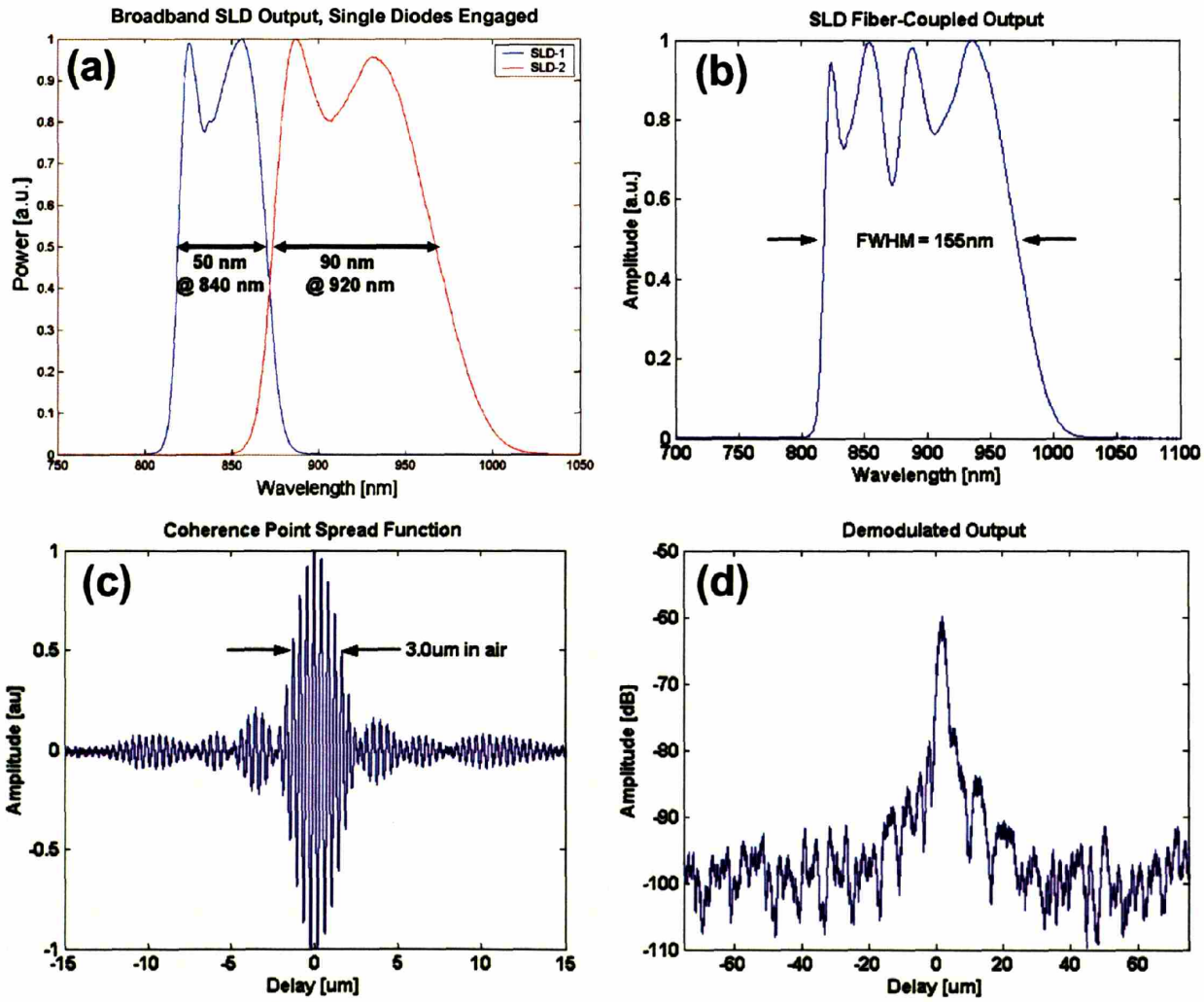

Figure 7-3. (a) Individual output spectra of the two superluminescent diodes. (b) Fiber-coupled multiplexed spectrum of the broadband SLD source. (c) Coherence point spread function of the broadband SLD source. (d) Logarithmic demodulated coherence point spread function. A 3.0 OD filter was used to prevent detector saturation.[15]

Figure 7-3(a) shows the individual output spectra of the two superluminescent diodes. Figure 7-3(b) shows the total fiber-coupled spectrum of the broadband SLD source, demonstrating a full-width-half-maximum bandwidth of 155 nm. With only one 50/50 interferometer, up to 1.6 mW of SLD power was available at the sample arm. The coherence point spread function of the broadband SLD source was measured by placing a mirror after the imaging microscope in the sample arm of the laboratory ultrahigh resolution OCT system. In

Figure 7-3(c), the interferometric point spread function from a mirror with an OD 3.0 filter was measured and shows a 3.0 μm OCT axial resolution in air, corresponding to approximately 2.3 μm in tissue. Because the spectrum of the light source has sharp edges and spectral modulation, sidelobes are present in the point spread function. However, since the intensity point spread function is the square of the field point spread function, these sidelobes do not produce significant image artifacts except when isolated high reflecting features are present. For *in vivo* animal imaging, axial scanning was performed at a velocity of 82 mm/sec with a Doppler frequency of 205 kHz and detection bandwidth of 54 kHz. Figure 7-3(d) shows that the point spread function after logarithmic demodulation demonstrates a sensitivity of 102 dB.

For *in vivo* ophthalmic retinal imaging, the clinical ultrahigh resolution OCT system was used. The water in the vitreous absorbs strongly at wavelengths above 920 nm and limits the bandwidth of the broadband SLD light source that can be used for retinal imaging.[18] A 24-mm length water cell was used in the reference arm in order to balance the dispersion in the eye. Absorption measurements performed on this water cell confirms that wavelengths longer than 920 nm were absorbed by the water. Therefore, the light incident on the eye was filtered to remove long wavelengths that would be absorbed by the vitreous, resulting in a bandwidth of 120 nm for ophthalmic imaging. The interferometric axial point spread function was measured using an isolated attenuated reflection from a mirror and was 4.3 μm in air, corresponding to 3.2 μm in the eye. Using 750 μW of incident power at the slitlamp output, well below the ANSI safety limit for retinal exposure, a sensitivity of ~92 dB was obtained. For ophthalmic imaging, axial scanning was performed at a velocity 410 mm/sec with a Doppler frequency of 1 MHz and detection bandwidth of 170 kHz. The axial scan length was 1.5 mm in tissue and the scan repetition rate was approximately 150 scans per second. Each ophthalmic image consists of 600 A-scans with an imaging scan time of approximately 4 seconds. This acquisition time was identical to that using a femtosecond solid-state laser light source and sufficiently short for the subject to keep the eye open and maintain fixation.

Ultrahigh Resolution OCT of hamster cheek pouch *in vivo*

Figure 7-4 shows an example of *in vivo* ultrahigh resolution OCT imaging in the hamster cheek pouch using the broadband SLD light source. This image has an axial resolution of approximately 2.3 μm in tissue and a transverse resolution of approximately 5 μm. A glass

coverslip was used on the surface of the exposed cheek pouch epithelium in order to reduce the high specular reflection caused by the large index mismatch from air to tissue. A cross-correlation algorithm was used to remove the motion artifacts caused by the breathing of the animal. No additional image processing techniques were applied to the image. This OCT image taken with the broadband SLD light source has image resolution and quality comparable to ultrahigh resolution OCT images of the hamster cheek pouch taken with a solid-state laser light source.[19] The stratum cornium is seen as a highly backscattering layer at the top of the cheek pouch, followed by the low backscattering epithelium layer. The muscularis layers and connective tissues below the epithelium layer can also be readily seen in this image. Blood vessels are clearly visible, which causes characteristic shadowing of the OCT signal below the level of the vessels.

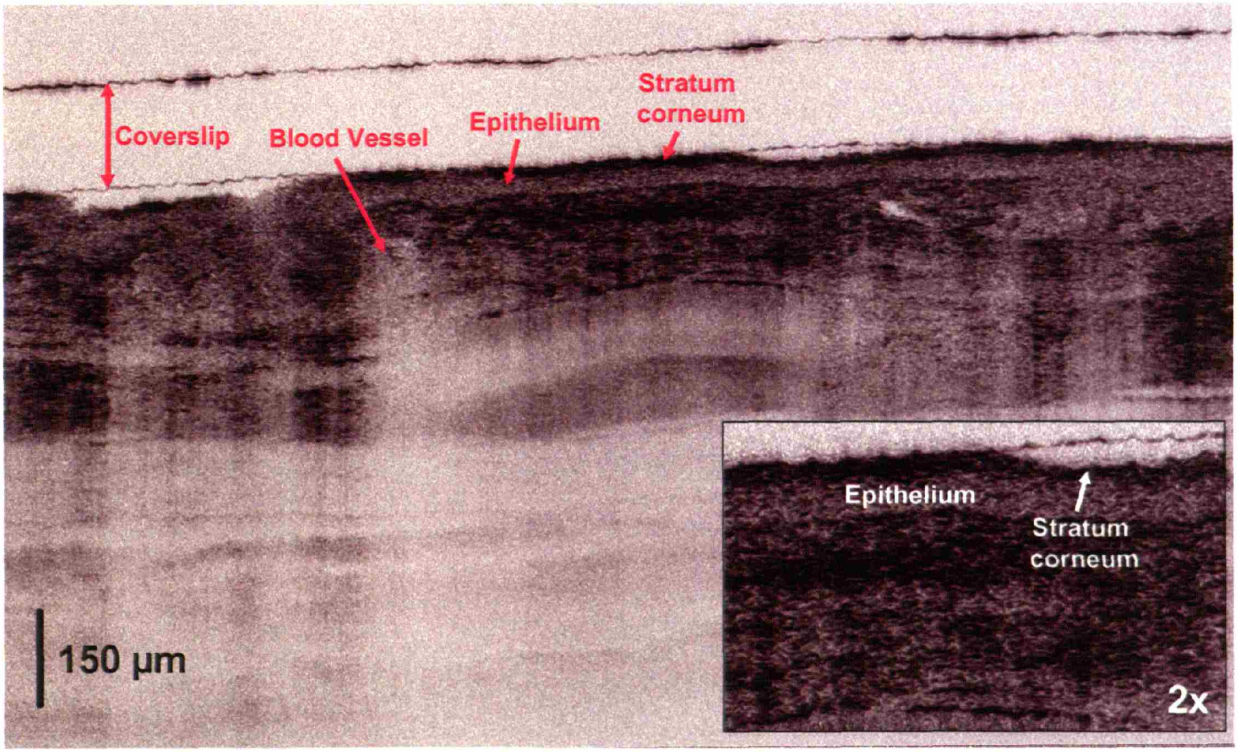

Figure 7-4. *In vivo* ultrahigh resolution OCT image of the Syrian golden hamster cheek pouch taken with the broadband SLD light source. Image axial resolution was 2.3 µm in tissue and transverse resolution was 5 µm. Ultrahigh resolution OCT imaging using a broadband SLD light source is capable of visualizing the stratum cornium, epithelium, muscularis, connective tissue, and blood vessels in the hamster cheek pouch.[15]

Ultrahigh Resolution OCT of human retina *in vivo*

We conducted a study comparing the retinal imaging capabilities of the broadband superluminescent diode light source with the clinical femtosecond laser light source for ultrahigh resolution OCT as well as standard 10 μm resolution, commercially available StratusOCT. OCT imaging was performed in the ophthalmology clinic. The OCT imaging was performed using 750 μW incident optical powers on all three systems. In order to facilitate the direct comparison of different images taken on the different OCT systems, imaging protocols for the commercial StartusOCT system was adopted on all systems. Six radial macular scans of 6 mm length each were acquired oriented at angles separated by 30-degree intervals, resulting in 3 mm rays at each clock hour emanating from the fovea. In a fashion similar to the macular scans, six radial optic nerve head scans of 4 mm length each centered on the optic disk can also be acquired. Circumpapillary scans of 3.4 mm, 4 mm, and 5 mm diameter centered on the optic disk were also acquired to compare the ability to differentiate different nerve fiber layer thickness at different imaging resolution.

Figure 7-5 shows the standard and ultrahigh resolution OCT images of the normal macula. Figure 7-5(A) is the ultrahigh resolution OCT image taken with the superluminescent diode light source, Figure 7-5(B) is the ultrahigh resolution OCT image taken with the femtosecond Titanium:sapphire laser at the same location, and Figure 7-5(C) is the StratusOCT image taken at the same position. Comparing the ultrahigh resolution OCT image of the macula taken with the superluminescent diode light source with the ultrahigh resolution OCT image taken with the femtosecond laser, both images are capable of identifying the fine retinal features such as ganglion cell layer, external limiting membrane, and photoreceptor segments that are hard to visualize in the standard resolution StratusOCT image. There appears to be very little difference between the two light sources in identifying small retinal structures and delineating different intraretinal layers. The OCT images taken with the femtosecond laser has slight higher signal-to-noise ratio than the OCT images taken with the superluminescent diode light source. However, the absolute signal-to-noise ratio of the OCT system using the superluminescent diode can be improved with additional a broadband circulator or by permanently fusing optical interconnections to reduce system losses. With these modifications, signal-to-noise performance approaching that of the current femtosecond laser OCT system is expected.

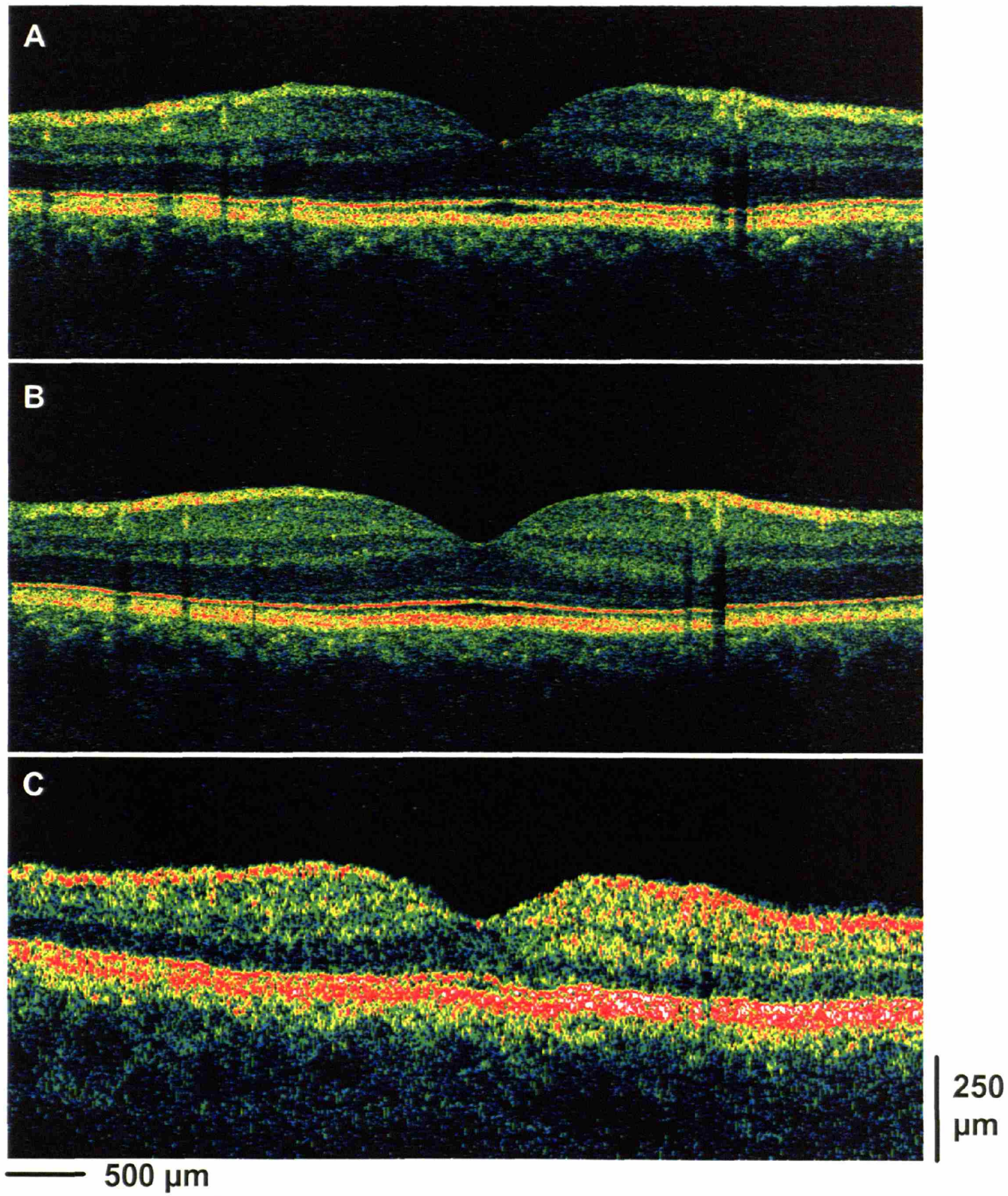

Figure 7-5. (A) Ultrahigh resolution OCT image of the normal macula taken with the broadband SLD light source. (B) Ultrahigh resolution OCT image taken with the femtosecond Titanium:sapphire laser at the same location. (C) StratusOCT image taken at the same position.

Figure 7-6 shows the standard and ultrahigh resolution OCT images of the normal optic nerve head taken across the optic disk. Figure 7-6(A) is the ultrahigh resolution OCT image taken with the superluminescent diode light source, Figure 7-6(B) is the ultrahigh resolution OCT image taken with the femtosecond titanium:sapphire laser at the same location, and Figure 7-6(C) is the StrausOCT image taken at the same position. This figure demonstrates the OCT systems' ability to image the optic nerve head to assess glaucomatous changes or neuro-ophthalmology pathologies. As in the macular OCT images, the nerve fiber layer (NFL) is highly backscattering and is visualized in the images as the first highly backscattering layer in the anterior portion of the retina. As expected from well-known retinal morphology, the nerve fiber layer thickens as it approaches the optic disk and the NFL thickness is at its maximum near the optic disk. Both ultrahigh resolution OCT images clearly distinguished the nerve fiber layer and other intraretinal layers such as the inner and outer plexiform layers and inner and outer nuclear layers better than the standard resolution StratusOCT. Both ultrahigh resolution OCT images are also better than StratusOCT at identifying the fine features of the outer retina such as the inner and outer photoreceptor segment junction and the retinal pigment epithelium.

Figure 7-7 shows the standard and ultrahigh resolution OCT images of the normal 3.4 mm diameter circumpapillary scan centered on the optic disk. This is the standard circumpapillary scan diameter used in the StratusOCT scanning protocols. Figure 7-7(A) is the ultrahigh resolution OCT image taken with the superluminescent diode light source, Figure 7-7(B) is the ultrahigh resolution OCT image taken with the femtosecond titanium:sapphire laser at the same location, and Figure 7-7(C) is the StrausOCT image taken at the same position. As is the case with the optic nerve head images (Figure 7-6), the ultrahigh resolution OCT images are much better at delineating the nerve fiber layer and other intraretinal structures than the standard resolution StratusOCT image. At 3.4 mm circumpapillary diameter, it is easy to identify the thickening of the nerve fiber layer that corresponds to the superior and inferior nerve fiber bundles and the anatomical thinning of the nerve fiber layer in the nasal region of the retina. Improved delineation of the nerve fiber layer should provide a more accurate and robust measurement of the NFL thickness in the circumpapillary scans and improve OCT morphometric measurements for glaucoma management.

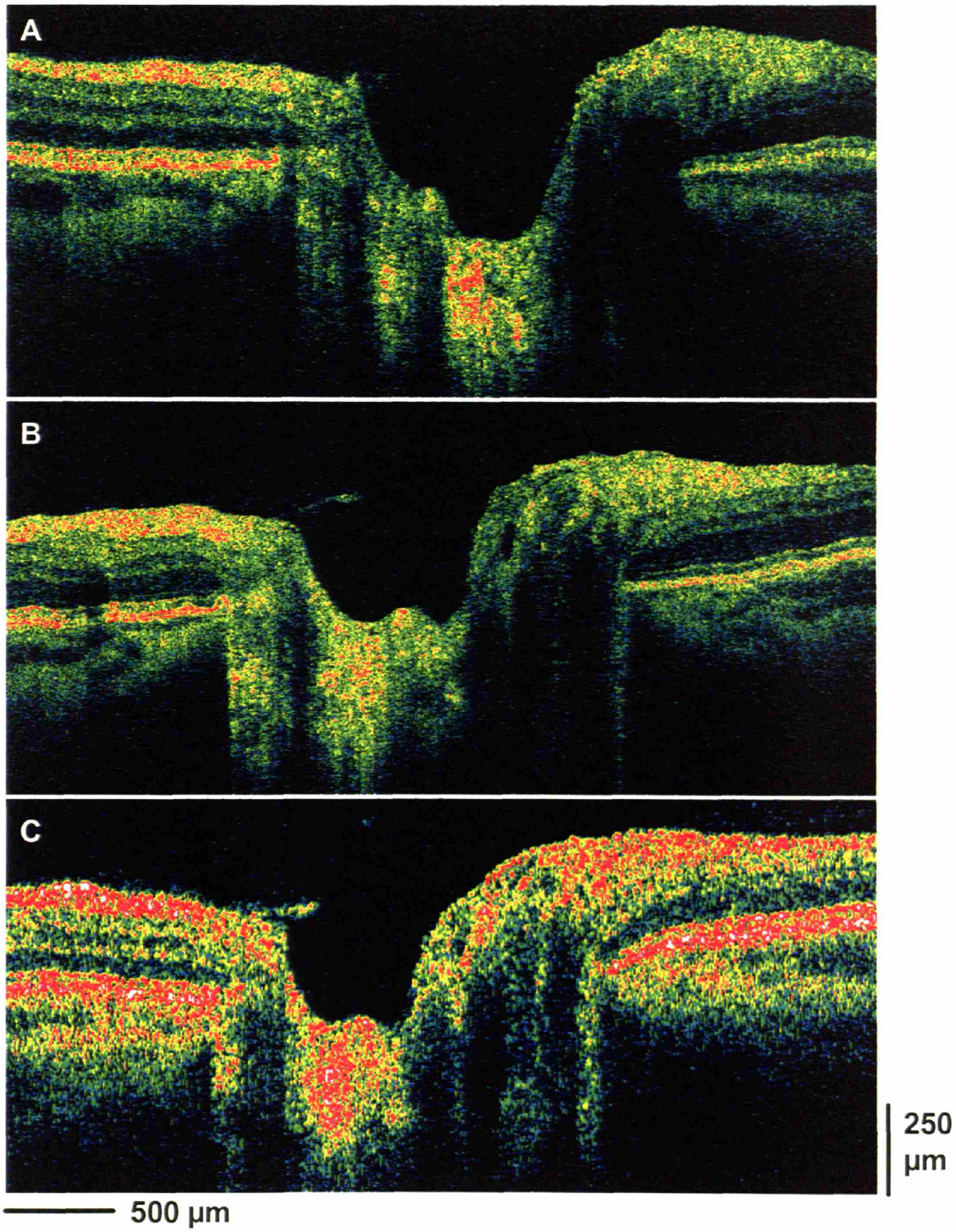

Figure 7-6. (A) Ultrahigh resolution OCT image of the normal optic disk taken with the broadband SLD light source. (B) Ultrahigh resolution OCT image taken with the femtosecond Titanium:sapphire laser at the same location. (C) StratusOCT image at the same position.

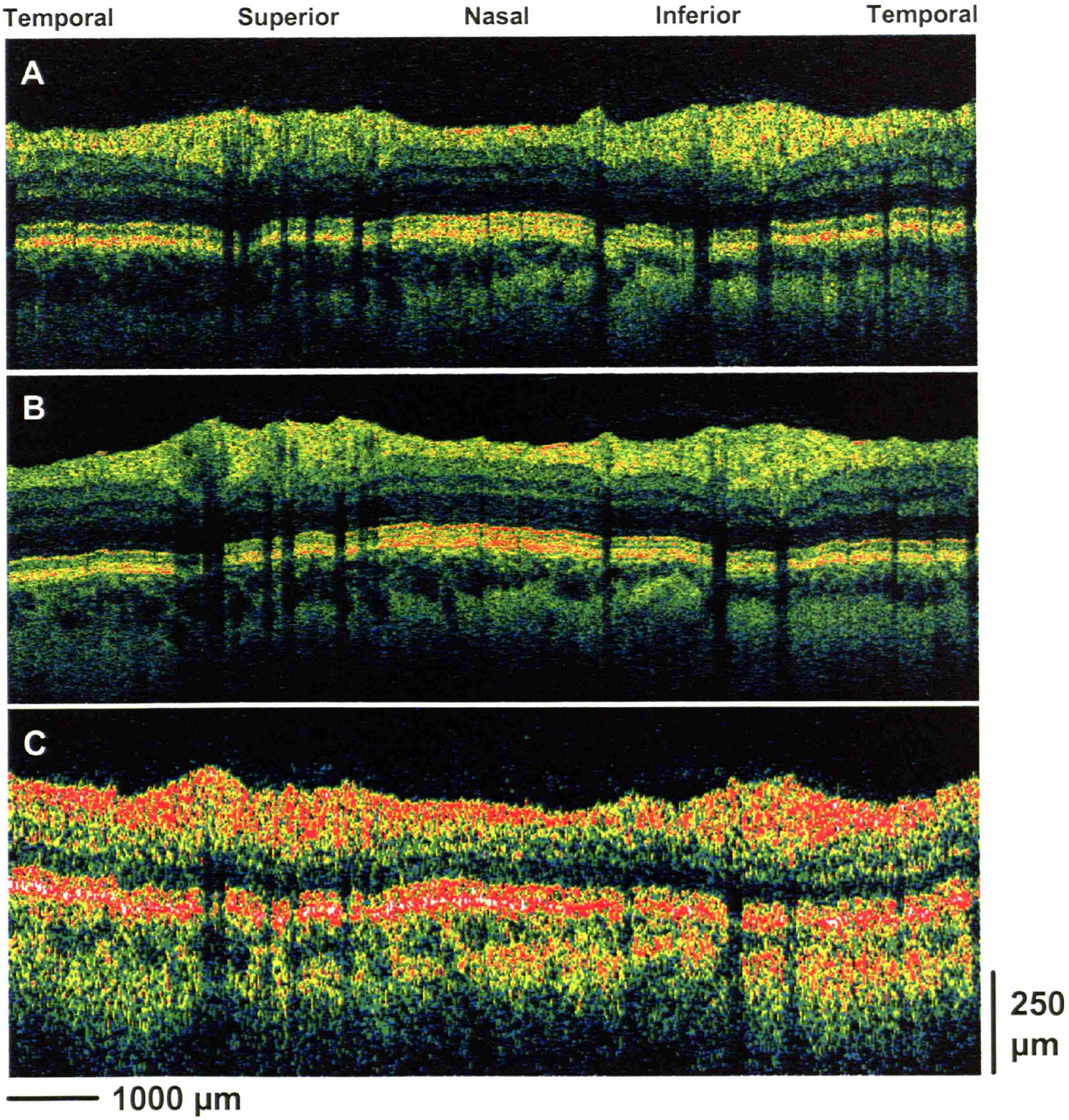

Figure 7-7. (A) Ultrahigh resolution OCT image of the normal 3.4 mm diameter circumpapillary scan centered on the optic disk taken with the broadband SLD light source. (B) Ultrahigh resolution OCT image taken with the femtosecond Titanium:sapphire laser at the same location. (C) StratusOCT image taken at the same position.

Figure 7-8 shows the standard and ultrahigh resolution OCT images of the 4 mm diameter circumpapillary scan centered on the optic disk. Figure 7-8(A) is the ultrahigh resolution OCT image taken with the superluminescent diode light source, Figure 7-8(B) is the ultrahigh resolution OCT image taken with the femtosecond Titanium:sapphire laser at the same location, and Figure 7-8(C) is the StrausOCT image taken at the same position. At 4 mm circumpapillay diameter, the nerve fiber layers are thinner the scans taken at 3.4 mm circumpapillay diameter (Figure 7-7) because the fibers are further away from the optic disk. Circumpapillary scans with larger scan diameter than conventional scanning protocol emulate the imaging of nerve fiber layer thinning under glaucomatous changes. OCT imaging's ability to detect nerve fiber layer thinning at different imaging resolutions can then be assessed. All three OCT images show the decrease in NFL thickness while both ultrahigh resolution OCT images show improved delineation of the nerve fiber layer over the standard resolution StratusOCT image.

Figure 7-9 shows the standard and ultrahigh resolution OCT images of the 5 mm diameter circumpapillary scan centered on the optic disk. Figure 7-9(A) is the ultrahigh resolution OCT image taken with the superluminescent diode light source, Figure 7-9(B) is the ultrahigh resolution OCT image taken with the femtosecond Titanium:sapphire laser at the same location, and Figure 7-9(C) is the StrausOCT image taken at the same position. At 5 mm circumpapillay diameter, the nerve fiber layers are thinner than the scans taken at 4 mm circumpapillay diameter (Figure 7-8) because the fibers are even further away from the optic disk; therefore, 5 mm circumpapillary scans can be used to emulate imaging of severe glaucomatous changes. All three OCT images show this decrease in NFL thickness while both ultrahigh resolution OCT images show improved delineation of the nerve fiber layer over the standard resolution StratusOCT image. The lower resolution of the StratusOCT image seems to suggest in the nasal region of the scan that the nerve fiber layer approaches zero thickness in parts of the scan (white arrow) while it is clear from both ultrahigh resolution OCT images that the nerve fiber layer is intact and does not reach zero thickness. In this case, the improved resolution of the ultrahigh resolution OCT imaging has enhanced the visualization of nerve fiber layer in the nasal region which can then be used to improve the measurement of nerve fiber layer thickness around the optic disk.

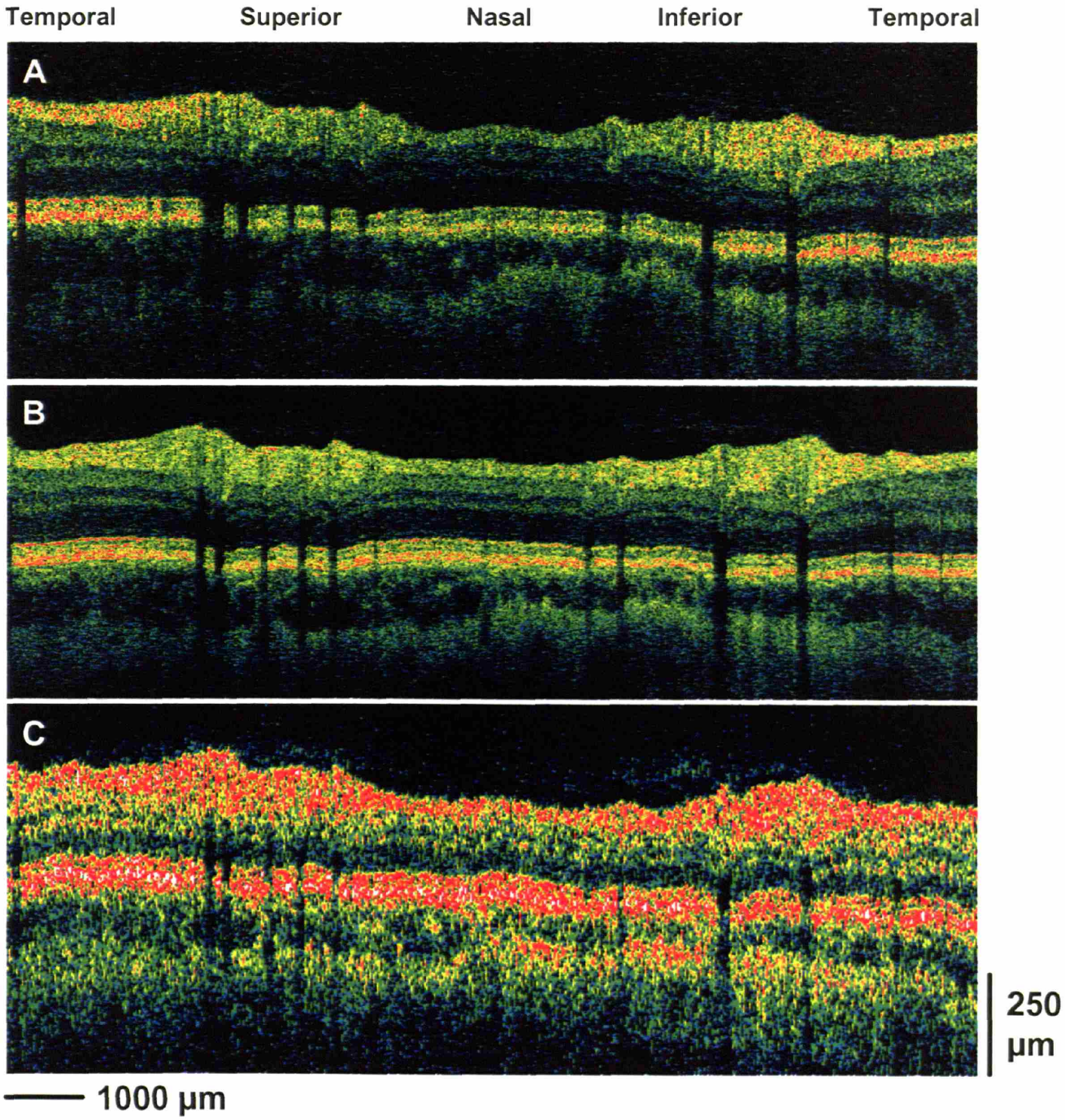

Figure 7-8. (A) Ultrahigh resolution OCT image of the 4 mm diameter circumpapillary scan centered on the optic disk taken with the broadband SLD light source. (B) Ultrahigh resolution OCT image taken with the femtosecond Titanium:sapphire laser at the same location. (C) StratusOCT image taken at the same position.

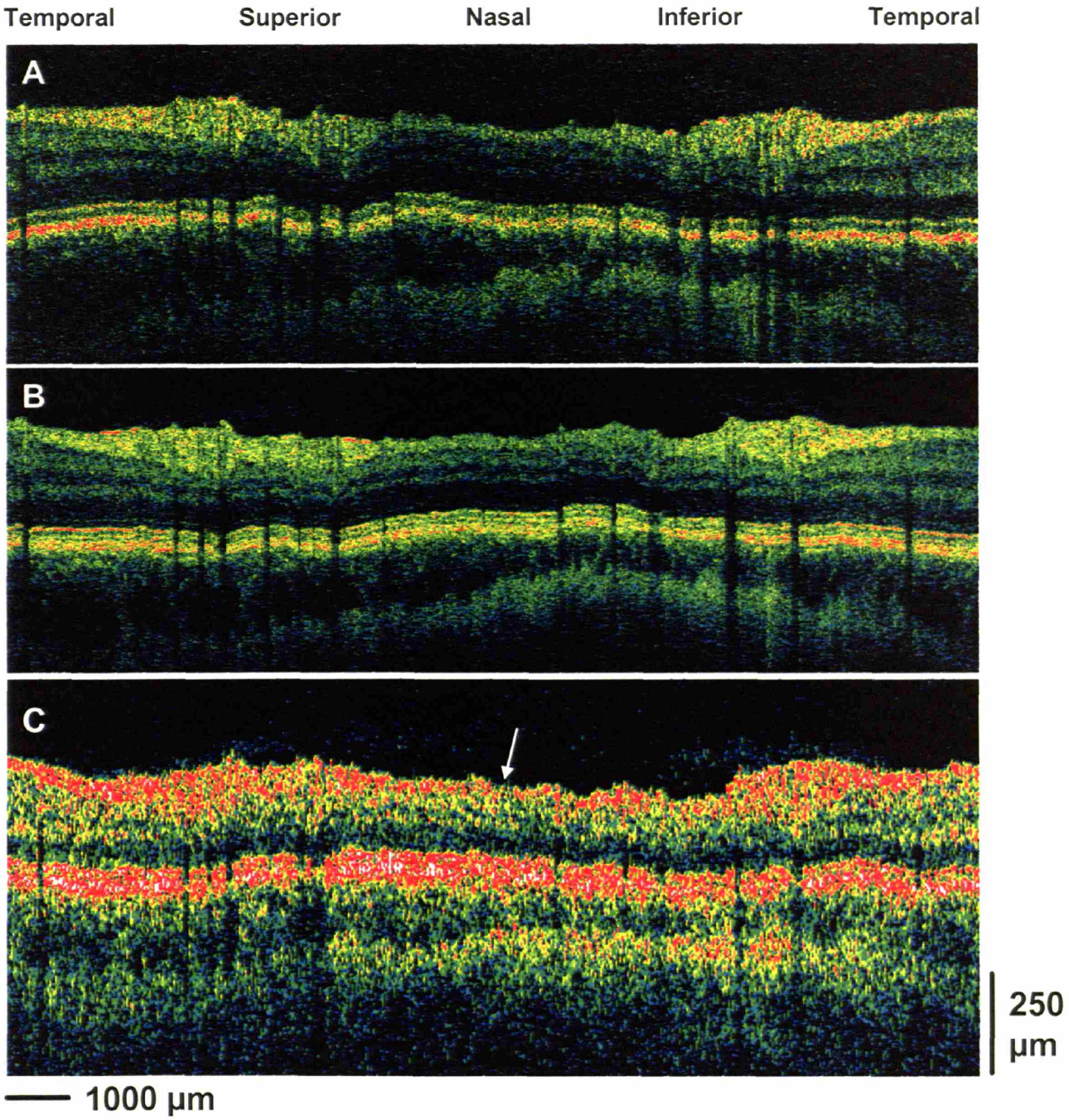

Figure 7-9. (A) Ultrahigh resolution OCT image of the 5 mm diameter circumpapillary scan centered on the optic disk taken with the broadband SLD light source. (B) Ultrahigh resolution OCT image taken with the femtosecond Titanium:sapphire laser at the same location. (C) StratusOCT image taken at the same position. The white arrow indicates the region of the StratusOCT scan that the nerve fiber layer appears to approach zero thickness.

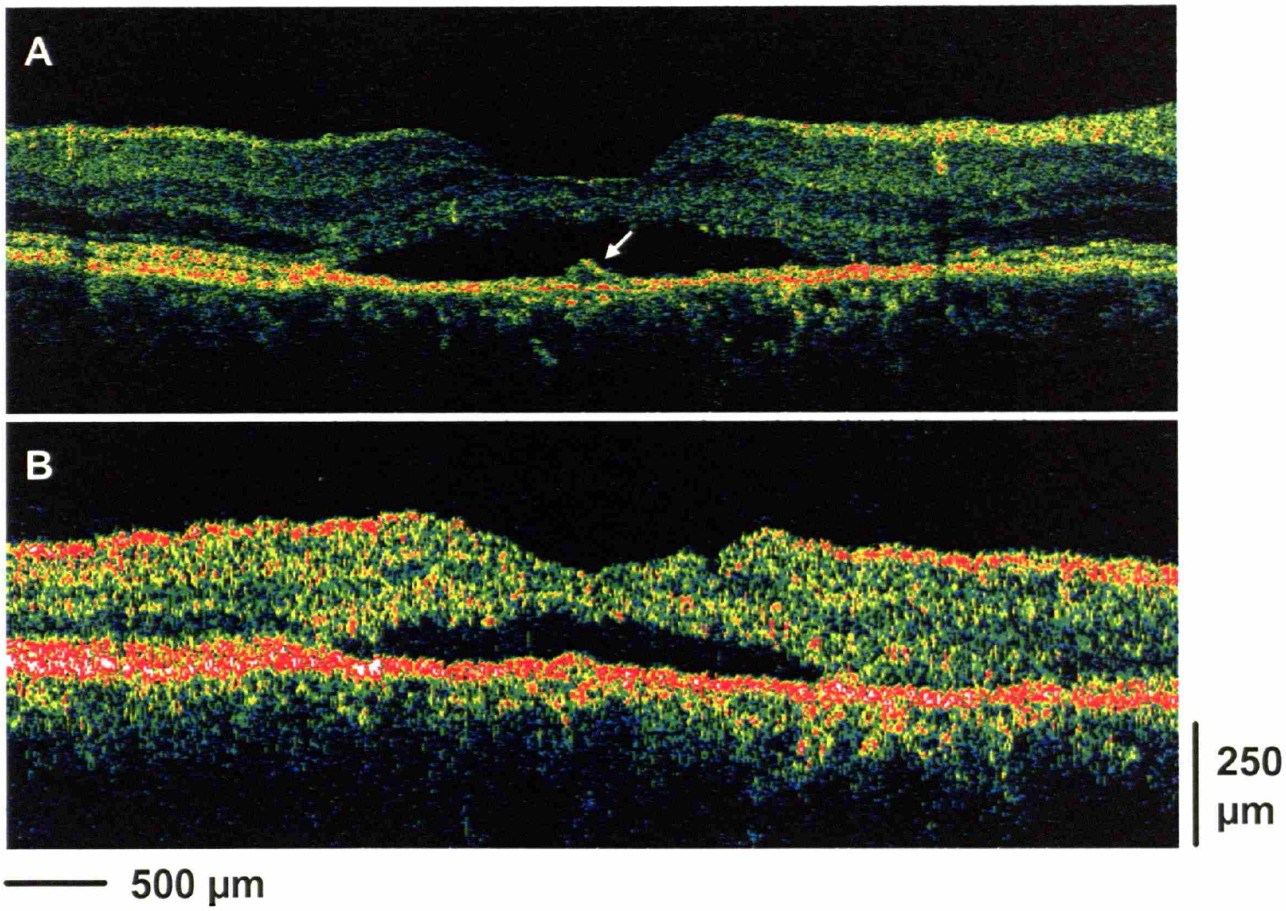

Figure 7-10. (A) Ultrahigh resolution OCT image of chronic central serous chorioretinopathy taken with the broadband SLD light source. The white arrow indicates the region of disruption in the RPE layer of the fovea under the serous detachment. (B) The StratusOCT image taken at the same location from the same patient does not clearly indicate the disruption of the RPE layer.

Figure 7-10 shows the standard and ultrahigh resolution OCT images of the macula of a 47-year old man with chronic central serous chorioretinopathy, demonstrating the clinical feasibility of the new diode light source for ultrahigh resolution OCT imaging. Figure 7-10(A) is the ultrahigh resolution OCT image taken with the superluminescent diode light source and Figure 7-10(B) is the StratusOCT image taken at the same position. Both images clearly show the serous detachment of the sensory retina. All the intraretinal layers in the sensory retina appear to be normal outside the region of sensory retina detachment. However, a disruption in the RPE layer of the fovea under the serous detachment can clearly be seen in the ultrahigh

resolution OCT image (white arrow). This disruption may be the probable cause for serous leakage of fluid into the intraretinal space and it was not clearly detected in the StratusOCT image due to its lower resolution.

Conclusions from Broadband SLD Imaging

To date, ophthalmic ultrahigh resolution OCT imaging in both laboratory-based and clinical systems has been achieved only with expensive femtosecond laser light sources that are difficult to operate and requires expert knowledge in laser operations. The expense and difficulty associated with operating the femtosecond laser light source has prevented the widespread application of the ultrahigh resolution OCT technology. In order to enable widespread implementation of ultrahigh resolution OCT imaging in the ophthalmology clinic, an inexpensive and robust imaging light source that is capable of generating high resolution images needs to be realized. We have demonstrated ultrahigh resolution OCT imaging based on a commercially available, low-cost (currently around ten thousand US dollars), superluminescent diode light source (Broadlighter 890, Superlum Diodes Ltd., Moscow, Russia). The imaging performance of the ultrahigh resolution OCT system based on the diode light source is very comparable to the performance achieved with a femtosecond laser light source. The Broadlighter 890 generated 155 nm bandwidth with a center wavelength of 890 nm while the titanium:sapphire femtosecond laser light source used in this study generated 125 nm bandwidth with a center wavelength of 815 nm. According to equation 2.2, the shorter center wavelength of the Titanium:sapphire femtosecond laser is expected to generated better axial resolution even with smaller total bandwidth. The measured OCT axial resolution of this laser was 3.5 μm in air which corresponds to less than 3 μm resolution in the eye accounting for the difference in index of refraction. The measured OCT axial resolution of the Broadlighter 890 was 4.3 μm in air which corresponds to ~3.2 μm resolution in the retina accounting for the difference in index of refraction. The small difference in axial resolution between the laser and the diode light sources was not discernable in the ultrahigh resolution OCT retinal images.

All the ultrahigh resolution OCT images taken with the Broadlighter 890 was able to distinguish and identify features that are visualized in the ultrahigh resolution OCT images taken with the Titanium:sapphire femtosecond laser. In contrast, the ultrahigh resolution OCT images taken with the Broadlighter 890 all had significant resolution improvements over the standard

resolution StratusOCT images, and the ultrahigh resolution OCT images can detect small intraretinal features such as the ganglion cell layer, the external limiting membrane, and photoreceptor segments much better than StratusOCT images. In clinical imaging (Figure 7-10), ultrahigh resolution OCT taken with the superluminescent diode source has higher resolution than StratusOCT and was able to identify small retinal features not seen in standard resolution images such as the disruption of the RPE related to central serous chorioretinopathy.

For retinal imaging, the axial resolution for this broadband SLD source was limited by the water absorption in the eye. The development of SLD devices at shorter wavelengths, which do not overlap the onset of water absorption at 920 nm, should improve resolution for retinal imaging in the future.[18] Although output powers are limited, the broadband SLD light source produces ultrahigh resolution OCT images which are comparable to those obtained using femtosecond solid state lasers. These results demonstrate the ability to achieve *in vivo* ultrahigh resolution OCT imaging using a compact, easy to operate, and relatively inexpensive SLD light source. The ability to obtain ultrahigh resolution OCT imaging without the expensive and complexity of operating a femtosecond laser should lower the threshold for implementation of ultrahigh resolution OCT technology in the clinic. A turnkey based diode light source that does not need constant laser realignment enables non-technical personnel to operate the ultrahigh resolution OCT ophthalmic imaging system. The relative low-cost of the superluminescent diode light source also improves the chance this technology may be adopted by commercial industry, eventually enabling the future widespread use of ultrahigh resolution OCT in ophthalmology clinics.

7.3 High-Speed, Ultrahigh Resolution OCT Imaging

Recent advances in OCT technology have enabled OCT imaging with a ~25 to 75 times increase in imaging speed over standard resolution OCT systems and ~100 times increase over conventional clinical ultrahigh resolution OCT systems.[20-24] In comparison to conventional OCT systems, these novel techniques are known as "spectral" or "Fourier domain" OCT because echo time delays of light are measured by Fourier transforming the interference spectrum of the light signal.[25, 26] This novel OCT detection technique has been shown to dramatically improve the sensitivity and speed of OCT imaging.[27-29] Spectral OCT detection techniques measure the echo time delay of light by measuring the spectrum of the interference between light from the tissue

and light from a stationary, un-scanned, reference arm. The echo time delays of the backscattered or backreflected light from the tissue can then be derived by taking the Fourier transform of the acquired interference spectrum. Since the light echoes from all of the different axial positions in the sample are measured simultaneously, rather than sequentially, it is possible to dramatically increase detection sensitivity and therefore increase the imaging speed. The resulting image is a measurement of echo time delay and magnitude of light analogous to the axial scan measurements in conventional OCT, except that scanning of the reference arm is not required and very high imaging speeds can be achieved.

Using these latest technological advances in the OCT field, a high-speed ultrahigh resolution spectral OCT system which can achieve axial image resolution of ~3 μm and can perform high-speed video-rate OCT imaging in the ophthalmology clinic has been developed by our group. This high-speed ultrahigh resolution OCT prototype can be operated with either a femtosecond laser or a broadband SLD as imaging light source. High-speed imaging will increase retinal coverage, improve image quality, reduce motion artifacts and achieve image registration to fundus features. With increased acquisition speed, multiple cross-sectional images may be rapidly acquired at different locations or orientations on the retina, improving the coverage of OCT scanning. In addition, it is possible to increase the number of axial scans per cross-sectional OCT images to improve the transverse pixel density and improve image quality and visualization of intraretinal layers. High-speed imaging will eliminate virtually all motion artifacts within the image and obviate the need for re-registration algorithms to correct axial motions, allowing the visualization of the true retinal topology. With these advances, it is possible to acquire a series of high pixel density OCT images that visualize retinal microstructure with unprecedented quality while preserving the true retinal topography. It is then possible to acquire three-dimensional OCT data that achieves comprehensive cross-sectional coverage of the retina. An OCT fundus image similar to a fundus photograph may then be created by the axial integration of three-dimensional OCT data to achieve image registration to fundus features. The combination of high image acquisition speed and ultrahigh OCT axial resolution promises to yield significant improvements in the clinical utility of high-speed ultrahigh resolution OCT systems over currently available prototype and commercial OCT systems.

Spectral Domain Ultrahigh Resolution OCT System

Conventional OCT systems perform measurements of the echo time delay of backscattered or backreflected light by using an interferometer with a mechanically scanned optical reference path.[4, 30, 31] Measurements of the echo delay and magnitude of light are performed by mechanically scanning the reference path length, so that light echoes with sequentially different delays are detected at different times as this reference path length is scanned. For this reason, these systems are known as "time domain" systems. Standard clinical ophthalmic OCT instruments such as the StratusOCT have scanning speeds of 400 axial scans per second and therefore can acquire a 512 axial scan (transverse pixel) OCT image in ~1.3 seconds.

A portable, high-speed ultrahigh resolution OCT system which can achieve high-speed video-rate ultrahigh resolution OCT imaging in the ophthalmology clinic has been developed. A detailed description of the system has been previously published.[23] Figure 7-11 shows a schematic of the high-speed, ultrahigh resolution OCT system using spectral/Fourier domain detection.

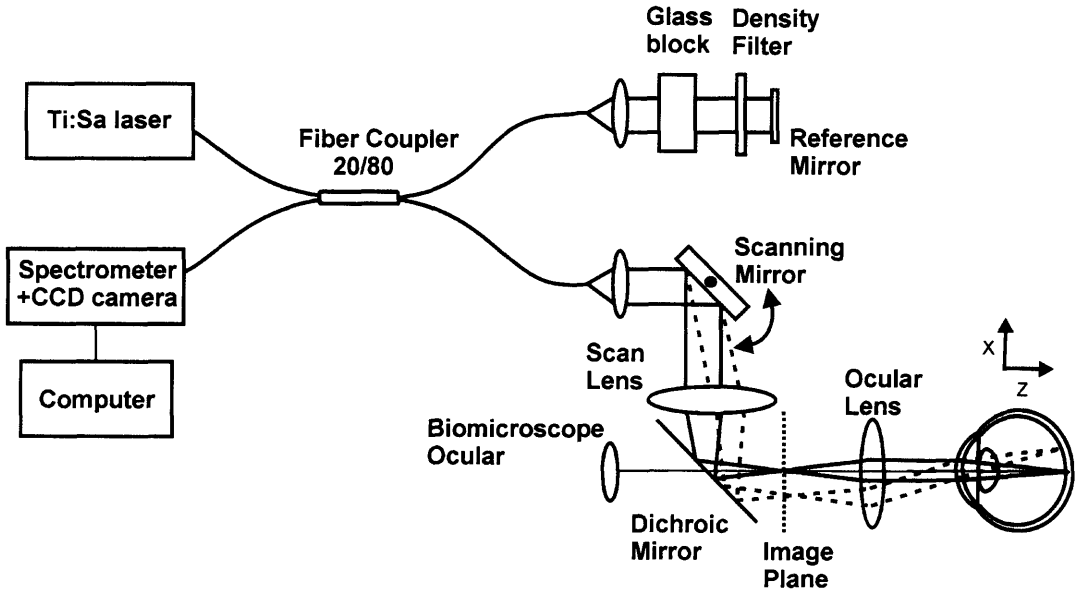

Figure 7-11. Schematic of high-speed, ultrahigh resolution "spectral/Fourier domain" OCT system. Echo time delays of backscattered or backreflected light are detected by measuring the spectrum of the interferometer output.[23]

Light from a broad bandwidth light source is split between the sample and reference arms of an interferometer. Light in the reference arm is attenuated and reflected from a stationary mirror at a fixed delay. Light in the sample arm is directed though two galvanometer-actuated steering mirrors and relay imaged through the pupil onto the retina.[31] The galvanometer actuated mirrors can scan the OCT beam across the retina in any arbitrary pattern in order to perform cross-sectional imaging. The spectrum of the interferometer output is detected using a spectrometer consisting of a collimating lens, transmission grating, imaging lens, and CCD line scan camera. The CCD line scan camera has 2048 pixels and was read at a 60 MHz pixel rate. The interference spectrum data from the camera was transferred to computer system memory (Pentium IV, 3.2 GHz) where it was rescaled from wavelength to frequency and Fourier transformed to generate axial measurements of the echo delay and magnitude of light from the retina.

The high-speed ultrahigh resolution OCT prototype can be operated with either a femtosecond laser or a broadband SLD as imaging light source. The clinical femtosecond Titanium:sapphire laser that has been implemented in the ophthalmology clinic (Chapter 2) has been integrated to the spectral OCT system for high-speed ultrahigh resolution OCT imaging. Moreover, the high-speed ultrahigh resolution OCT prototype can also be integrated to a broad bandwidth SLD light sources that is capable of performing ultrahigh resolution OCT imaging.[15] The turn-key based broadband SLD device will allow for more robust operation of the imaging light source in the clinical environment. The bandwidths and point spread functions of the two light sources are comparable, and the incident powers on the eye are identical. The ultrahigh resolution OCT images acquired with the two different sources are comparable in quality and signal-to-noise ratio.

The prototype high-speed, ultrahigh resolution OCT system enables retinal imaging speeds of up to 30,000 axial scans per second, corresponding to acquiring ~58 OCT images, each consisting of 512 axial scans or transverse pixels, every second. Since computer data processing such as Fourier transformations are required to generate the axial scan information from the raw interference spectrum measurements, the real time display of the OCT images on the monitor is limited to ~18 images (of 512 axial scans each) per second. This rate is sufficient to provide a flicker-free display of OCT imaging and can be used to provide feedback to the operator for

OCT scan alignment and focusing on the retina. This real time analysis and image display is achieved using only computer software programs and without any additional specialized hardware to assist data processing. It is important to note that the real-time display does not impede data acquisition, it is possible to simultaneously acquire data at the maximum rate while displaying acquired imaged at a slower rate.

The extremely high imaging speed of the high-speed ultrahigh resolution OCT allows for the demonstration of different retinal imaging protocols which were previously not possible to achieve. Using the high-speed ultrahigh resolution OCT system, different macular imaging protocols were performed in order to compare the relative advantage and clinical utility of each scanning protocol. The first protocol acquires a set of three very high pixel density images (8192 axial scans per image). Because of the very high pixel density (<1 μm per transverse pixel for a 6 mm cross-sectional image), transverse averaging may be used to increase the image signal-to-noise ratio without degrading the transverse resolution. Each high pixel density image can be acquired in ~0.3 second from a retinal area of interest in a manner similar to the "line scan" feature of the StratusOCT instrument. Because data acquisition for one such image takes approximately one-fourth of the time required for a 512 pixel StratusOCT image, image artifacts caused by axial motion is expected to be greatly reduced. This scan protocol is also especially useful for obtaining images in patients with opaque media or other conditions that reduce the detectable OCT signal and therefore the signal-to-noise ratio. The second scan protocol acquires a series of 24 radial cross-sectional scans (1500 axial scans per image) of the macula on a 6 mm diameter circle centered on the fovea. The radial scans were performed in a fashion similar to the StratusOCT macular mapping protocol, except that the data set contains four times more number of scans and can be completely acquired in ~1.2 second, less than the time required for StratusOCT to acquire one 512 axial-scan image. The third protocol acquires a series of 21 high pixel density (2048 axial scans per image) cross-sectional images in a raster pattern covering 6mm x 6mm area centered on the fovea. With spectral/Fourier domain detection techniques, this image set can be acquired in ~1.4 seconds, corresponding to ~0.07 s per image. Because of the rapid acquisition, retinal topography is preserved within each cross-sectional image. The fourth protocol acquires data in a dense raster pattern consisting of 180 images with 512 transverse pixels per image. This protocol covers a 6 mm square region with a volume element (voxel) size of 12 μm x 30 μm x 1.3 μm. Here three-dimensional OCT (3D OCT) data set is acquired, which

may be used for applications such as surface rendering, fudus image formation, and mapping. Because acquisition of each image takes approximately 22 ms, the total acquisition time for three-dimensional data is approximately 4 seconds, the same time it currently takes to acquire one ultrahigh resolution cross-sectional OCT image. Motion during acquisition of complete 3D OCT data is expected to be comparable to motion during acquisition of a single ultrahigh resolution OCT image.

High-Speed, Ultrahigh Resolution OCT Imaging

It is helpful to first compare cross sectional images of StratusOCT, conventional ultrahigh resolution OCT, and high-speed ultrahigh resolution OCT in order to compare the relative performance of each of these imaging systems. Figure 7-12 shows a comparison of macular and optic disc scans acquired with the different OCT systems at the same retinal location.

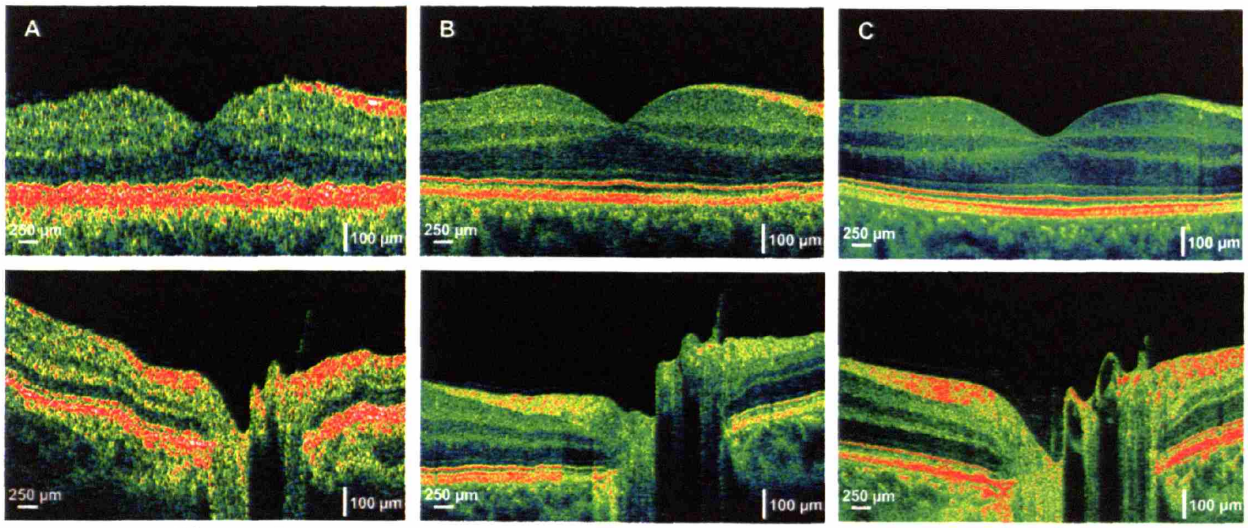

Figure 7-12. Comparison of standard resolution StratusOCT, ultrahigh resolution OCT, and high-speed ultrahigh resolution OCT using "spectral/Fourier" domain detection. (A) StratusOCT images of macula (upper) and optic disc (lower) have 10 µm resolution contain 512 axial scans (transverse pixels) and are acquired in ~1.3 seconds. (B) Ultrahigh resolution OCT images have ~3 µm axial resolution, contain 600 axial scans and are acquired in ~4 seconds. (C) High-speed ultrahigh resolution OCT images have ~2 µm axial resolution, contain 2048 axial scans and are acquired in ~130 ms. Note the dramatic improvement in image quality and speed.

The StratusOCT images (Figure 7-12A) have ~10 μm axial and 20 μm transverse resolution in tissue and consist of 1024 axial pixels and 512 transverse pixels acquired in ~1.3 second. The conventional ultrahigh resolution OCT images (Figure 7-12B) have ~3 μm axial and 15-20 μm transverse resolution in tissue and consisted of 3000 axial and 600 transverse pixels acquired in ~4 seconds. The high-speed ultrahigh resolution OCT images (Figure 7-12C) have ~3 μm axial and ~10 μm transverse resolution in tissue and consisted of 1024 axial pixels and 2048 transverse pixels acquired in ~0.07 second. Compared to the StratusOCT and conventional ultrahigh resolution OCT images, the high-speed ultrahigh resolution OCT images provide excellent visualization of the architectural morphology of the internal retinal layers. The high axial resolution and high transverse pixel density in the high speed ultrahigh resolution OCT images enabled better visualization of the nerve fiber layer (NFL), ganglion cell layer (GCL), and the fine photoreceptor structures of the outer retina such as the external limiting membrane (ELM), junction between the photoreceptor inner and outer segments (IS/OS) and retinal pigment epithelium (RPE). The extremely rapid image acquisition also has the advantage that eye motion artifacts from changes in retinal axial position or fixation are greatly reduced. Therefore, unlike StratusOCT and conventional ultrahigh resolution OCT imaging, motion correction algorithms for axial motions are not required for the high-speed ultrahigh resolution OCT images.[4] In regions with important topography such as the optic disc, motion correction algorithms can introduce artifacts which distort the true topography of the feature in the OCT image (Figure 7-12B). High-speed imaging therefore can provide a more accurate visualization of retinal topography than is possible using lower speed, conventional OCT.

High-speed ultrahigh resolution OCT also enables unprecedented increases in the transverse pixel density of the image which can improve visualization of certain morphologic features. Figure 7-13 shows an example of an image of the macular region with 8000 axial scans (transverse pixels). A segmentation algorithm has been applied to detect the boundaries of the internal retinal layers. In addition to overall retinal thickness, virtually all major retinal layers including nerve fiber (NFL), ganglion cell (GCL), inner and outer plexiform and nuclear layers can be identified and quantitatively measured. The detailed structure of the photoreceptors such as the external limiting membrane (ELM), junction between the inner and outer segments (IS/OS), and the retinal pigment epithelium (RPE) can be segmented and thicknesses measured.

The ability to quantitatively assess photoreceptor structure and photoreceptor integrity or impairment could be a powerful objective measure of disease progression in diseases such as retinitis pigmentosa or other retinal degenerative disorders. Quantitative measurement of total retinal thickness is an important measure of macular edema in diabetic retinopathy and quantitative measurement of the nerve fiber layer is an important diagnostic for glaucoma detection and management.

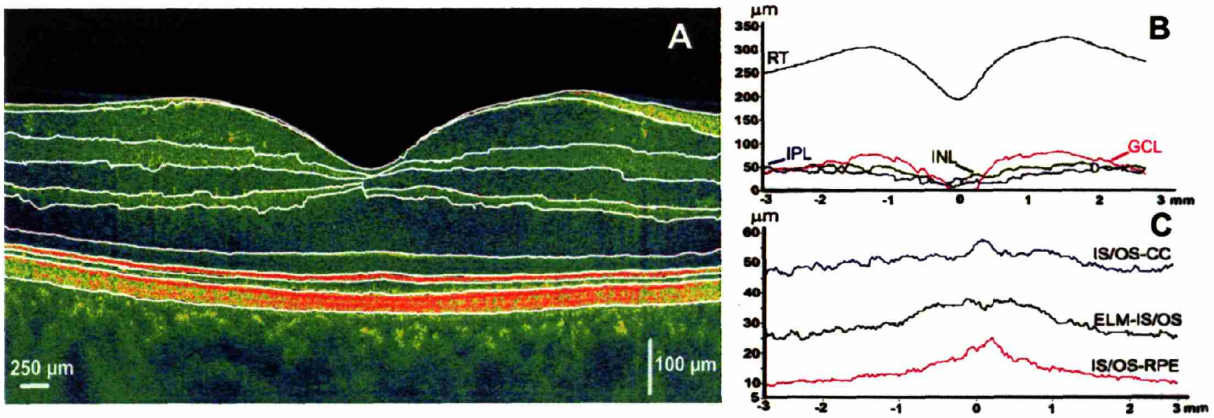

Figure 7-13. (A) High transverse pixel density images enable segmentation of intraretinal layers. (B) Thickness measurements were obtained from the entire retina (RT), inner nuclear layer (INL), inner plexiform layer (IPL), and ganglion cell layer (GCL. (C) Distances between outer retinal layers such as the external limiting membrane (ELM), junction of photoreceptor inner and outer segments (IS/OS), retinal pigment epithelium (RPE), and choriocapillaris (CC) can be measured.

Figure 7-14 shows high-speed ultrahigh resolution OCT images selected from the set of 24 OCT images radial scanned from the macula. Each OCT image in this radial set consists of 1500 axial scans and the entire set of 24 images can be acquired in 1.2 seconds. Since the ETDRS region is a circular area centered on the fovea, high transverse pixel density radial macular scans that better match the ETDRS region is useful for mapping the macular thickness. A radial scanning protocol has the advantage that it concentrates measurements in the foveal region, where information is most clinically relevant. In addition, the fovea is visible in all images and serves as a landmark which confirms patient fixation. The 24 high-speed ultrahigh resolution OCT radial images are separated by only 7.5 degrees between the images and the

entire set can be acquired in ~1.2 second. This radial scan protocol is similar to the protocol that was implemented on the StratusOCT.[32] However, the StratusOCT uses only 6 radial images and since the angle between the images is 30 degrees, focal pathologies can be missed. Figure 7-15 shows a macular thickness map generated from the 24 radial scanned OCT images in a manner similar to the ETDRS-type macular thickness map of the StratusOCT. The map is divided into 9 ETDRS-type regions, and the average macular thickness for each region is displayed in microns. The improved sampling density, axial resolution, and imaging speed of the new high-speed ultrahigh resolution OCT promises to improve the sensitivity and reproducibility of retinal thickness measurements as well as enable the detection of focal retinal pathologies.

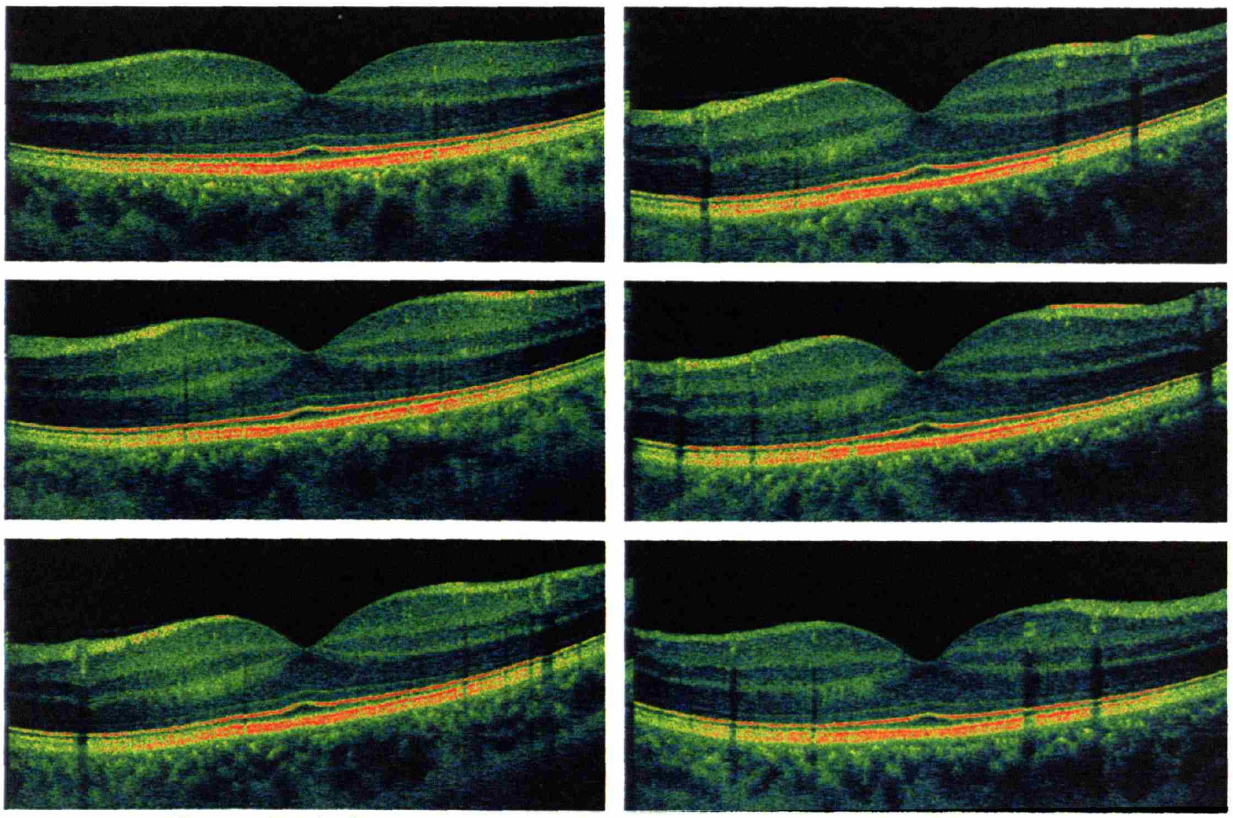

Figure 7-14. Selected images from a set of 24 radial OCT images scanned from the macula with the high-speed, ultrahigh resolution OCT system. With improved transverse sampling of 1500 A-scans per image, the intraretinal layers are better visualized than standard 600 A-scan ultrahigh resolution OCT images.

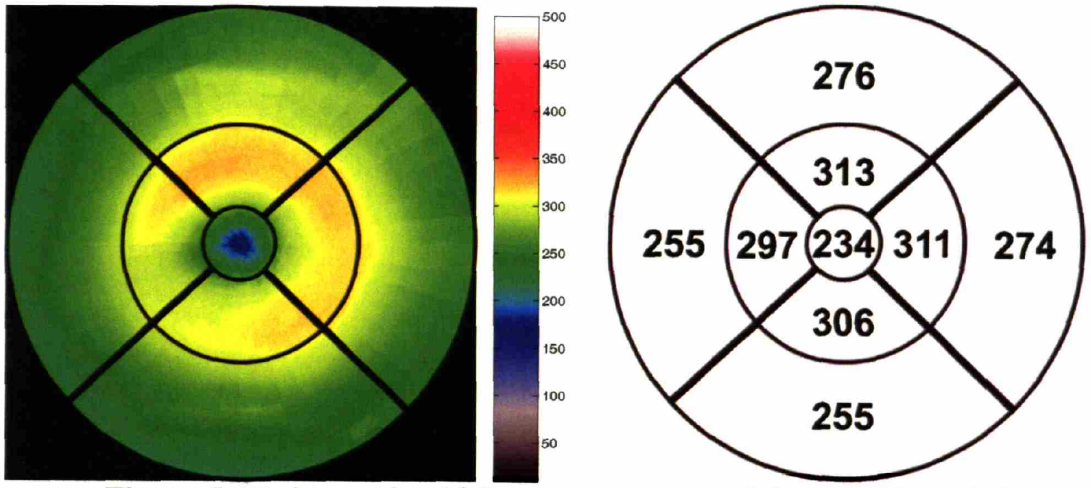

Figure 7-15. A macular thickness map generated from the 24 radial scanned OCT images in a manner similar to the ETDRS-type macular thickness map of the StratusOCT.

Figure 7-16 shows high-speed ultrahigh resolution OCT images selected from the set of 21 images raster scanned from the macula. Each OCT image in this raster set consists of 2048 axial scans and the entire set of 21 images can be acquired in ~1.4 seconds with each OCT image separated from the subsequent image by only 300 μm. The raster scans has the advantage of sampling on a rectangular grid, providing uniform coverage and simple reconstruction of the retinal thick map. The improved sampling density, axial resolution, and faster imaging speed promises to improve sensitivity and reproducibility of thickness measurements and enable detection of focal pathologies.

Finally, three-dimensional cross-sectional information can be acquired from the retina using high-speed ultrahigh resolution OCT imaging. OCT data can be acquired in a dense raster pattern consisting of 180 images with 512 transverse pixels per image. This protocol covers a 6 mm square region with a volume element (voxel) size of 12 μm x 30 μm x 1.3 μm. Three-dimensional OCT (3D OCT) can be used to generate a fundus view of the scanned region that consists purely of OCT data. To generate the OCT fundus view, images from the 3D OCT data set are summed along the axial direction. Cross-sectional images in the 3D OCT data set are automatically registered to features such as blood vessels visible on the OCT fundus image. In turn, it is possible to correlate the OCT fundus view with a standard fundus photo as shown in Figure 7-17 and to find the precise location transverse location of OCT scans. While this

procedure may be used to register 3D OCT cross-sectional images, it may also be extended to register cross-sectional images from other protocols by correlation with images from the 3D OCT data set.

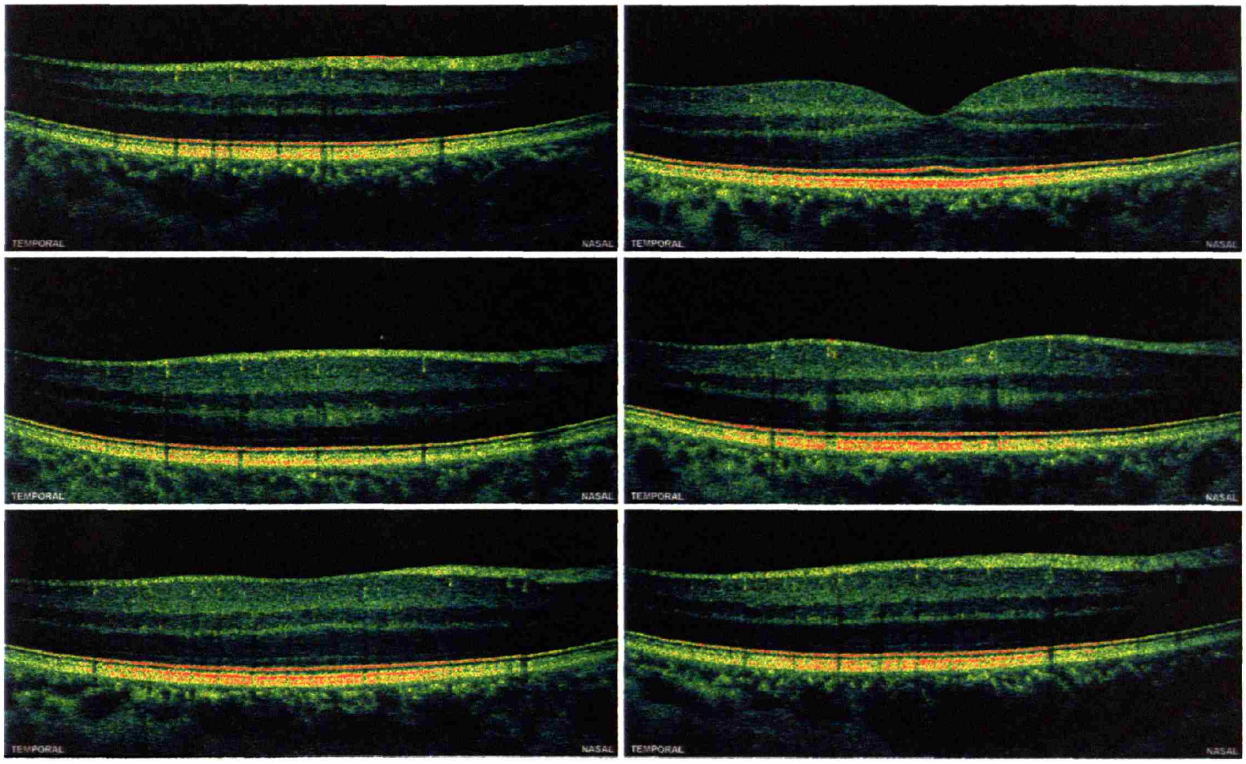

Figure 7-16. Selected images from a set of 21 raster OCT images scanned from the macula with the high-speed, ultrahigh resolution OCT system.

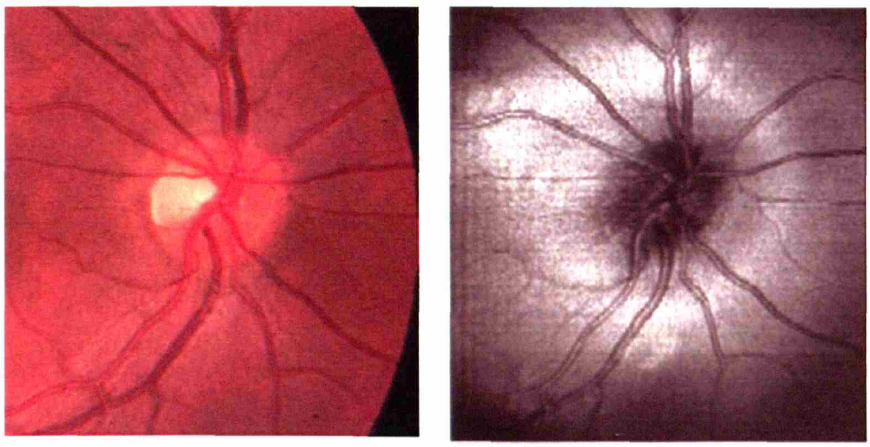

Figure 7-17. (Left) Fundus photograph of a normal optic disk region. (Right) An OCT fundus view generated purely from three-dimensional OCT data showing that cross-sectional OCT images can be precisely registered to fundoscopic features seen in the fundus photograph.

Conclusions from High-Speed, Ultrahigh Resolution OCT Imaging

The development of the high-speed, video-rate, ultrahigh resolution OCT system represents a significant advance in the capability of OCT imaging for ophthalmology. A prototype high-speed Spectral OCT system can perform ultrahigh resolution OCT imaging at over 30,000 axial scans (transverse pixels) per second, more than 100 fold improvement in imaging speed over the previous clinical ultrahigh resolution OCT system.[2] The improvement in imaging speed combined with the ultrahigh axial resolution promises to significantly improve the clinical utility of high-speed ultrahigh resolution OCT imaging over conventional commercial OCT systems.

The ability to perform high-speed ultrahigh resolution OCT imaging enables the acquisition of high transverse pixel density images which can improve OCT image quality and allow for detailed viewing of small retinal features. In high-speed ultrahigh resolution OCT imaging, extremely high pixels density images, such as 8000 transverse pixels, can be acquired from a retinal region of interest in a manner similar to the "line scan" feature of the StratusOCT instrument. In the high-speed OCT system, three such 8000 transverse pixel images can be acquired in ~0.8 second. High pixel density imaging and averaging has the advantage of increasing signal-to-noise ratio without degrading transverse resolution, thereby improving visualization of intraretinal layers. This can be seen in Figure 7-12, which compares standard and high-speed ultrahigh resolution OCT images with comparable axial and transverse resolutions. The intraretinal layers are better visualized in the high-speed images due to the higher transverse scan density than the standard ultrahigh resolution OCT image. The ELM and photoreceptor IS/OS junction are more clearly delineated in the high-speed ultrahigh resolution OCT images. In addition, a hyperreflective layer is visualized between the IS/OS junction and the RPE in high-speed ultrahigh resolution OCT images, which is not clearly seen in StratusOCT or ultrahigh resolution OCT images. The improved visualization of these layers in cross-sectional images may lead to improved performance of image segmentation algorithms and increase our understanding of this portion of the retina.

This study has also shown that high-speed scanning can eliminate virtually all motion artifacts in the OCT image and obviate the need for using re-registration algorithms to correct for

the axial motions of the subject. This advantage of the high imaging speed allows for the visualization of the true retinal topology. This can be seen in Figure 7-12, which shows a comparison between StratusOCT, conventional ultrahigh resolution OCT, and high-speed ultrahigh resolution OCT images of a normal macula and optic disk. The StratusOCT images shown contain 512 axial scans and require ~1.4 seconds for acquisition. They are not corrected for axial motion, although motion correction by computer is possible. Due to the relatively long acquisition time, the apparent retinal contour in the image is somewhat distorted by subject motion. Images acquired with the conventional clinical ultrahigh resolution OCT prototype require ~4 seconds for acquisition and consist of 600 axial scans. Because of the relatively long acquisition period, all conventional ultrahigh resolution OCT images must be corrected for axial motion, losing topographical information. This can be clearly seen in the optic disk image, where the nerve head is "flattened" by the correction algorithm. High-speed ultrahigh resolution OCT imaging does not require axial motion correction (Figure 7-12) and therefore can provide a more accurate visualization of retinal topography than is possible using slower, conventional OCT.

For measuring and mapping retinal thickness, the improvement in the imaging speed of the high-speed ultrahigh resolution OCT system has obvious advantages over conventional OCT systems. The high-speed ultrahigh resolution OCT system represent a greater than 100 fold increase in imaging speed over conventional OCT systems, and it can enable a increased numbers of OCT scans to be performed in a thickness mapping protocol set while reducing the total amount of imaging time. The increase numbers of OCT scans improves the fundus coverage of the thickness mapping protocols and increase the likelihood of detecting focal retinal pathologies that may be missing with current commercial OCT technology. In addition, a number of innovative mapping protocols can be performed using high-speed ultrahigh resolution OCT imaging. The concept of raster scanning, by acquiring consecutive images at equally spaced lateral locations, has been previously demonstrated;[31] however, due to speed limitations of the conventional OCT systems, radial and circumpapillary scanning protocols were chosen as the clinical retinal imaging protocols.[31, 32] Because the scan speed of StratusOCT is limited, only six radial OCT images centered on the fovea are acquired for mapping the macular thickness and only six radial OCT scans centered on the optic disc are acquired for the reconstruction of the optic nerve head. Since the radial pattern of six tomograms samples macular thickness at clock-

hours, the retinal thickness information in the wedges between each tomogram is interpolated. Therefore, this imaging protocol may miss focal pathologies located in a span of less than one clock hour, or 30°. In addition, the 6 radial macular tomograms cover a 6 mm diameter circle and have a maximum distance between samples of 1.6 mm at the perimeter of the circle. With the development of high-speed ultrahigh resolution OCT, it is now possibly to dramatically increase the number of radial scans in a mapping set in order to improve the retinal coverage for macular thickness mapping and optic nerve head reconstruction. Rapid raster scans of the retina can also be achieved within a suitable imaging time with the high-speed ultrahigh resolution OCT system. The raster scan has the advantage of sampling on a rectangular grid, providing uniform coverage and simple reconstruction of thickness maps. In our study, twenty-four radial scans of the macular can also be performed in a 6 mm diameter circle centered on the fovea in order to generate a macular thickness map (Figure 7-15). Each radial OCT image consists of 1500 axial scans or transverse pixels and the entire 24 image macular set can be acquired in ~1.2 second. Twenty-one raster scans of the macula can be performed in a 6 mm square area centered on the fovea. Each OCT image consists of 2048 axial scans (transverse pixels) and the entire 21 image set can be acquired in ~1.4 second, approximately the time for StratusOCT to acquire one image with 512 axial scans.

In addition to novel scanning protocols, high-speed ultrahigh resolution OCT imaging can also be used to acquire three dimensional OCT data in a dense raster pattern. Three dimensional OCT scanning achieves comprehensive coverage of the retina and can be used to create an OCT fundus image which is an *en face* image similar to a fundus photograph for precise registration of cross-sectional images to fundus features. This solves one of the longstanding problems in conventional OCT imaging, the precise and repeatable registration of OCT images with the fundus. The combination of three dimensional OCT scanning and high-speed retinal thickness mapping protocols will allow for precise and reproducible morphometric measurements to improve the detection and follow to progression of retinal pathologies.

Previously, all ultrahigh resolution OCT studies had been performed using femtosecond lasers. While providing axial OCT image resolutions approaching 1-3 μm, femtosecond lasers traditionally are expensive and require frequent re-alignment which make these type of light sources difficult to operate in a clinical setting. The high-speed ultrahigh resolution OCT system can perform imaging with both a standard femtosecond laser and a broadband

superluminesceond diode (SLD) light source. The broadband SLD sources combine two or more superluminescent diodes with complementary bandwidths in order to achieve a larger effective bandwidth, and therefore enable ultrahigh axial image resolutions. These broadband SLD light sources are lower cost, more compact and robust than femtosecond lasers, and therefore are likely to enable wider spread availability of ultrahigh resolution OCT imaging.

7.4 Future of Ophthalmic Ultrahigh Resolution OCT Imaging

The future of ultrahigh resolution OCT imaging for ophthalmology appears very bright. This thesis project has demonstrated that ultrahigh resolution OCT has the possibility to improve the diagnosis and management of retinal diseases as well as increase the understanding of ocular disease pathogenesis. With the demonstration of ultrahigh resolution OCT imaging using a broadband SLD light source, the chances has improved that this technology may be adopted by commercial industry, eventually enabling the widespread use of ultrahigh resolution OCT in ophthalmology. The improvement in imaging speed combined with the ultrahigh axial resolution can also significantly improve the clinical utility of high-speed ultrahigh resolution OCT imaging over conventional OCT systems. High-speed ultrahigh resolution OCT imaging can reduce motion artifacts, improve image quality, enable detailed zooming of the OCT images, and allow registration of cross-sectional images to fundus features. High-speed thickness mapping with ultrahigh resolution OCT can improve the scan coverage of the fundus, enhance detection of focal pathology, and enable the performance of different mapping protocols in a very short total imaging time. High-speed ultrahigh resolution OCT imaging enhances the capabilities of OCT and eliminates a number of the current limitations of ultrahigh resolution OCT. Therefore, the development of the high-speed ultrahigh resolution OCT system with broadband SLD light sources represents a significant advance in the imaging capability of this technology and it will significantly improve the utility of OCT imaging in ophthalmology. Therefore, ultrahigh resolution OCT has the potential in the future to become an important tool for ophthalmology research and clinics.

7.5 References

1. Drexler W, Sattmann H, Hermann B, et al. Enhanced visualization of macular pathology with the use of ultrahigh-resolution optical coherence tomography. Archives of Ophthalmology 2003;121(5):695-706.

2. Ko TH, Fujimoto JG, Duker JS, et al. Comparison of ultrahigh- and standard-resolution optical coherence tomography for imaging macular hole pathology and repair. Ophthalmology 2004;111(11):2033-43.

3. Wollstein G, Paunescu LA, Ko TH, et al. Ultrahigh-resolution optical coherence tomography in glaucoma. Ophthalmology 2005;112(2):229-37.

4. Swanson EA, Izatt JA, Hee MR, et al. In vivo retinal imaging by optical coherence tomography. Optics Letters 1993;18(21):1864-6.

5. Clivaz X, Marquis-Weible F, Salathe RP. Optical low coherence reflectometry with 1.9 mu m spatial resolution. Electronics Letters 1992;28(16):1553-5.

6. Kowalevicz AM, Ko T, Hartl I, et al. Ultrahigh resolution optical coherence tomography using a superluminescent light source. Optics Express 2002;10(7).

7. Pollnau M, Salathe RP, Bhutta T, et al. Continuous-wave broadband emitter based on a transition-metal-ion-doped waveguide. Optics Letters 2001;26(5):283-5.

8. Crunteanu A, Pollnau M, Janchen G, et al. Ti:sapphire rib channel waveguide fabricated by reactive ion etching of a planar waveguide. Applied Physics B (Lasers and Optics) 2002;B75(1):15-7.

9. Pollnau M. Broadband luminescent materials in waveguide geometry. Journal of Luminescence 2003;102-103:797-801.

10. Alphonse GA, Toda M. Mode coupling in angled facet semiconductor optical amplifiers and superluminescent diodes. Journal of Lightwave Technology 1992;10(2):215-19.

11. Alphonse GA. Design of high-power superluminescent diodes with low spectral modulation. Test and Measurement Applications of Optoelectric Devices, Jan 21-22 2002. San Jose, CA, United States: The International Society for Optical Engineering, 2002; v. 4648.

12. Shidlovski V, Wei J. Superluminescent diodes for optical coherence tomography. Test and Measurement Applications of Optoelectric Devices, Jan 21-22 2002. San Jose, CA, United States: The International Society for Optical Engineering, 2002; v. 4648.

13. Swanson EA, Chinn SR, Boppart SA, et al. Optical coherence tomography: principles, instrumentation, and applications. Proceedings of 21st Australian Conference on Optical

Fibre Technology (ACOFT'96), 1-4 Dec. 1996. Gold Coast, Qld., Australia: IREE Soc, 1996.

14. Baumgartner A, Hitzenberger CK, Sattmann H, et al. Signal and resolution enhancements in dual beam optical coherence tomography of the human eye. Journal of Biomedical Optics 1998;3(1):45-54.

15. Ko TH, Adler DC, Fujimoto JG, et al. Ultrahigh resolution optical coherence tomography imaging with a broadband superluminescent diode light source. Optics Express 2004;12(10):2112-9.

16. Semenov AT, Shidlovski VR, Jackson DA, et al. Spectral control in multisection AlGaAs SQW superluminescent diodes at 800 nm. Electronics Letters 1996;32(3):255-6.

17. Mamedov DS, Prokhorov VV, Yakubovich SD. Superbroadband high-power superluminescent diode emitting at 920 nm. Quantum Electronics 2003;33(6):471-3.

18. Hale GM, Query MR. Optical constants of water in the 200-nm to 200-μm wavelength region. Applied Optics 1973;12(3):555-63.

19. Hartl I, Li XD, Chudoba C, et al. Ultrahigh-resolution optical coherence tomography using continuum generation in an air-silica microstructure optical fiber. Optics Letters 2001;26(9):608-10.

20. Cense B, Nassif NA, Chen TC, et al. Ultrahigh-resolution high-speed retinal imaging using spectral-domain optical coherence tomography. Optics Express 2004;12(11).

21. Leitgeb RA, Drexler W, Unterhuber A, et al. Ultrahigh resolution Fourier domain optical coherence tomography. Optics Express 2004;12(10):2156-65.

22. Wojtkowski M, Bajraszewski T, Gorczynska I, et al. Ophthalmic imaging by spectral optical coherence tomography. Am J Ophthalmol 2004;138(3):412-9.

23. Wojtkowski M, Srinivasan VJ, Ko TH, et al. Ultrahigh-resolution, high-speed, Fourier domain optical coherence tomography and methods for dispersion compensation. Optics Express 2004;12(11):2404-22.

24. Nassif NA, Cense B, Park BH, et al. In vivo high-resolution video-rate spectral-domain optical coherence tomography of the human retina and optic nerve. Optics Express 2004;12(3).

25. Fercher AF, Hitzenberger CK, Kamp G, Elzaiat SY. Measurement of Intraocular Distances by Backscattering Spectral Interferometry. Optics Communications 1995;117(1-2):43-8.

26. Hausler G, Linduer MW. "Coherence radar" and "spectral radar"-new tools for dermatological diagnosis. Journal of Biomedical Optics 1998;3(1):21-31.

27. Leitgeb R, Hitzenberger CK, Fercher AF. Performance of Fourier domain vs. time domain optical coherence tomography. Optics Express 2003;11(8):889-94.

28. de Boer JF, Cense B, Park BH, et al. Improved signal-to-noise ratio in spectral-domain compared with time-domain optical coherence tomography. Optics Letters 2003;28(21):2067-9.

29. Choma MA, Sarunic MV, Yang CH, Izatt JA. Sensitivity advantage of swept source and Fourier domain optical coherence tomography. Optics Express 2003;11(18):2183-9.

30. Huang D, Swanson EA, Lin CP, et al. Optical coherence tomography. Science 1991;254(5035):1178-81.

31. Hee MR, Izatt JA, Swanson EA, et al. Optical coherence tomography of the human retina. Archives of Ophthalmology 1995;113(3):325-32.

32. Hee MR, Puliafito CA, Duker JS, et al. Topography of diabetic macular edema with optical coherence tomography. Ophthalmology 1998;105(2):360-70.